ABSTRACT

Title of Dissertation: STUDY OF TRANSIENT EFFECTS IN PHOTO-
EXCITED SEMICONDUCTING POLYMERS

Yi-Hsing Peng
Doctor of Philosophy, 2008

Directed By: Professor Chi H. Lee
Department of Electrical and Computer Engineering

Semiconducting conjugated polymers regioregular poly(3-hexylthiophene) (RR-P3HT) and poly[2-methoxy-5-(2'ethyl-hexyloxy)-1,4-phenylene vinylene] (MEH-PPV) have received considerable interest for prospective applications in organic photovoltaics (OPV). Understanding the photo-initiated processes and carrier transport in those materials is essential to improve the performance of the polymer OPV devices. Optical pump-Terahertz (THz) probe time domain spectroscopy (OPTP-TDS) is a noncontact technique which combines THz time domain spectroscopy and the pump-probe method. OPTP-TDS provides the ability to study the transient properties of photoexcited semiconducting materials.

In this thesis, we establish new standard experimental and analysis procedures for OPTP-TDS by adopting the analysis method suggested by Nienhuys and Sundstrom for investigating the transient events that are faster than the duration of THz probe pulses. We observed experimentally artifacts in the conductivity of photoexcited GaAs, as predicted by Nienhuys and Sundstrom, when we apply the

conventional analysis method. For the first time, we successfully remove the artifacts and recover the true transient conductivity of photoexcited GaAs using the correction transformation.

P3HT/PCBM blends are investigated using OPTP-TDS. The new analysis process enables us to obtain the time resolved frequency dependent complex photoconductivity in subpicosecond resolution. The time resolved conductivity is analyzed by the Drude-Smith model to describe the behavior of localized charge carriers in the polymer. Transient mobility drop at subpicosecond time resolution in the photoexcited polymer is observed for the first time. The mobility drop can be explained by the polaron formation in the polymer, and is the main cause of the transient real conductivity drop in the first picosecond after photoexcitation.

Semiconducting polymer MEH-PPV is investigated using OPTP-TDS, DC-bias transient photoconductivity, and photo-induced reflectivity change with high time resolution to get the transient conductivities at electrical, THz, and optical frequencies. The data are fitted with the Drude-Smith model and the Lorentzian oscillation model to describe free and bound carriers. The quantum efficiency of excitons was estimated to be less than 0.01, which is lower than previous reports. The imaginary conductivity at THz frequencies is attributed not to excitons but bound carriers with one tenth energy of excitons, which are possibly phonons.

STUDY OF TRANSIENT EFFECTS IN PHOTO-EXCITED
SEMICONDUCTING POLYMERS

By

Yi-Hsing Peng

Dissertation submitted to the Faculty of the Graduate School of the
University of Maryland, College Park, in partial fulfillment
of the requirements for the degree of
Doctor of Philosophy
2008

Advisory Committee:
Professor Chi H. Lee, Chair/Advisor
Doctor Warren N. Herman
Professor Julius Goldhar
Professor Thomas E. Murphy
Professor James R. Anderson

DEDICATION

To my parents, my wife, and my daughter

ACKNOWLEDGEMENTS

I would like to express my sincerest gratitude to my adviser, Prof. Chi Hsiang Lee, for his guidance and mentoring that have helped me go through the difficulties of the research, and for his encouragements and being supportive all the time. I also would like to thank Dr. Weilou Cao, who has shared with me his knowledge and skills in all aspects when I needed help. I would like to thanks Dr. Warren N. Herman for his resources and suggestions that have made my studies go smoothly. I would like to show gratitude to Prof. Julius Goldhar and Dr. Danilo Romero for their insightful suggestions to my research. I would like to thanks Prof. Thomas E. Murphy and James R. Anderson for accepting my request to serve on the dissertation committee.

Also, I would like to show appreciation to Dr. Hongye Liang for training me and helping me in the early stage of my research. I would like to thank Min Du, Dr. Mihaela Ballarotto, Victor Yun, and Dr. Yongzhang Leng for preparing the samples and supporting the experiments. I would like to thank other colleagues in both Prof. Lee's and LPS polymer groups, including Dr. Jinjin Li, Dr. Junghwan kim, Dr. Younggu Kim, Glenn Hutchunson, Alen Lo, Dr. Wei-Yen Chen, Dr. Shuo-Yen Tseng, and Dr. Dong Hung Park.

Finally, my thanks go to my parents, for their support and encouragement during my studies, and my wife, Ching-Yee Chang, who and I have supported and cheered up each other through all the difficulties and who shares all the happiness and sadness in our life together. Also thank my daughter, Sophia, who has given joy and happiness to my life.

TABLE OF CONTENTS

LIST OF TABLES

LIST OF FIGURES

ix

xiii

LIST OF ABBREVIANTIONS

2D	Two-dimensional
BAMH-PPV	Polyphenylenevinylene
FWHM	Full width half maximum
HOMO	The highest occupied molecular orbital
IR	Infrared
IRAV	Infrared-active vibrational
ITO	Indium tin oxide
LUMO	The lowest unoccupied molecular orbital
MEH-PPV	Poly[2-methoxy-5-(2'ethyl-hexyloxy)-1,4-phenylene vinylene]
OD	Optical densities
OFET	Organic field-effect transistors
OLED	Organic light-emitting diodes
OPTP-TDS	Optical pump-THz probe time domain spectroscopy
OPV	Organic photovoltaics
P3HT	Poly(3-hexylthiophene)
PCBM	[6,6]-phenyl-C_{61}-butyric acid methyl ester
RR	Regioregular
THz	Terahertz
ZnTe	Zinc telluride

Chapter 1: Introduction

1.1 Motivation and contributions

Semiconducting polymers have received considerable interest for prospective applications in organic electronic and photonic devices such as organic field-effect transistors (OFET), organic light-emitting diodes (OLED), and organic photovoltaics (OPV). In contrast to conventional semiconductors, these materials are flexible, lightweight, low cost, easy to process, and tunable for properties. For OPV applications, current power conversion efficiencies in semiconducting polymer solar cells are still about an order lower than that in conventional semiconductor solar cells. To further improve the performance of the polymer OPV devices, understanding the photo-initiated processes and carrier transportation in those materials is essential.

Optical pump-Terahertz (THz) probe time domain spectroscopy (OPTP-TDS) is a noncontact technique developed in recent years. It combines THz time domain spectroscopy and the pump-probe technique. Due to the low frequency nature of THz waves, THz time domain spectroscopy is very sensitive to free charge carriers. THz pulses are generated and detected coherently, so both the amplitude and phase of the THz electric field transmitted through a sample can be obtained simultaneously. Consequently, both the real and imaginary parts of conductivity spectra can be analyzed. The important properties such as free carrier quantum efficiency and mobility can be extracted when an adequate conductivity model is applied. Pump-probe is a technique to measure an ultrafast phenomenon. In the experiment, the probe pulse probes a transient event that is

initiated by the pump pulse. Because the pump and probe pulses are synchronized, the ultrafast phenomenon can be resolved. By using optical pump and THz probe, OPTP-TDS has the potential to study the transient properties of photoexcited semiconducting materials.

When the sample's properties are changing fast with respect to the duration of the THz pulses, the interpretation of results for OPTP-TDS is not straight forward. Kindt and Schmuttenmaer [46] proposed a data analysis method, which is aided with a two dimensional scan in the OPTP-TDS experiment, to obtain the transient photoinduced conductivity in this situation. The analysis method was adopted in many OPTP-TDS experiments [41][48][49][50][78], and it became a standard experimental and analysis procedure for OPTP-TDS. Recently, Nienhuys and Sundstrom [29] reported a theoretical analysis of the OPTP-TDS measurement. The results showed that the conductivity obtained using the standard method is complicated and actually has little physical meaning if the event is faster than the duration of the THz pulses. They also suggested a new analysis method which involves a series of transformations to recover the true transient conductivity.

Semiconducting conjugated polymers regioregular poly(3-hexylthiophene) (RR-P3HT) and poly[2-methoxy-5-(2'ethyl-hexyloxy)-1,4-phenylene vinylene] (MEH-PPV) have been studied using OPTP-TDS by other groups [48][49][50][78] due to their potential uses in OPV applications. In these experiments, they are either using the conventional analysis method proposed by Kindt and Schmuttenmaer [48][49] or avoiding measurement of the properties at the beginning of the photoexcitation when the dynamics is faster than the THz duration [50][78]. To our knowledge, currently there is

2

no OPTP-TDS experiment using the new analysis method suggested by Nienhuys and Sundstrom.

In this thesis, we establish new standard experimental and analysis procedures for OPTP-TDS by adopting the analysis method suggested by Nienhuys and Sundstrom for investigating transient events that are faster than the duration of THz probe pulses. We observed experimentally the artificial conductivity of photoexcited GaAs predicted by Nienhuys and Sundstrom when we apply the conventional analysis method. We, for the first time, successfully remove the artificial effect, and recover the true transient conductivity of photoexcited GaAs using a correction transformation.

P3HT/PCBM blends are investigated using OPTP-TDS. The new analysis process enables us to obtain the time resolved frequency dependent complex photoconductivity with subpicosecond resolution. The time resolved conductivity is analyzed by the Drude-Smith model[75] to describe the behavior of localized charge carriers in the polymer. A transient mobility drop at subpicosecond time scales in the photoexcited polymer is observed for the first time. The decrease mobility can be explained by polaron formation in the polymer, and is the main cause of the transient drop in the real conductivity in the first picosecond after photoexcitation.

The semiconducting polymer MEH-PPV is investigated using OPTP-TDS, DC-bias transient photoconductivity, and photo-induced reflectivity change with high time resolutions to get the transient conductivities at electrical, THz, and optical frequencies. The data are fitted by the Drude-Smith model and Lorentzian oscillator model to describe free and bound carriers. The quantum efficiency of exciton generation was estimated to be less than 1%, which is lower than previous reported [48]. The imaginary conductivity

at THz frequencies is attributed not to excitons but to the bound carriers with one tenth energy of excitons, which are possibly phonons.

1.2 THz and THz spectroscopy

THz radiation is an electromagnetic wave whose frequency is between 0.1 and 10 THz. It corresponds to wavelengths between 3 mm and 30 μm, and photon energies between 0.4 and 40 meV (see Figure 1-1). This frequency range sometimes is also called far infrared or sub-millimeter wave. Below this frequency range, microwaves and radio waves can be generated by electronics, and have wide applications in broadcast, communications, food processing, and radar. Above the THz frequency range, infrared, visible radiation, and other higher frequency rays are based on photonics. Their main applications are in communications, lighting, inspection, and medical imaging. Between the microwave and IR frequencies, the THz frequency range was also known as the 'THz gap', because neither efficient sources nor sensitive detectors were available to make measurements until developments in recent years.

There are now several techniques to generate and sense THz radiation in both electrical and optical approaches. Optical rectification [1], photoconductive antenna [2], optical parametric generation [3], and semiconductor surface emission [4] are used for THz pulsed sources. Electro-optic sampling [5][7], photoconductive antenna [2], and bolometer [6] are detection mechanism for these sources. For CW THz wave, Gunn diode [8], quantum cascade laser (QCL) [9], photomixing [10], backward-wave oscillator (BWO) [11], free electron laser (FEL) [12], and gas laser are the sources, while

bolometer, pyroelectricity, Schottky diode [13] , and plasma wave electronics [14] are
used for detection.
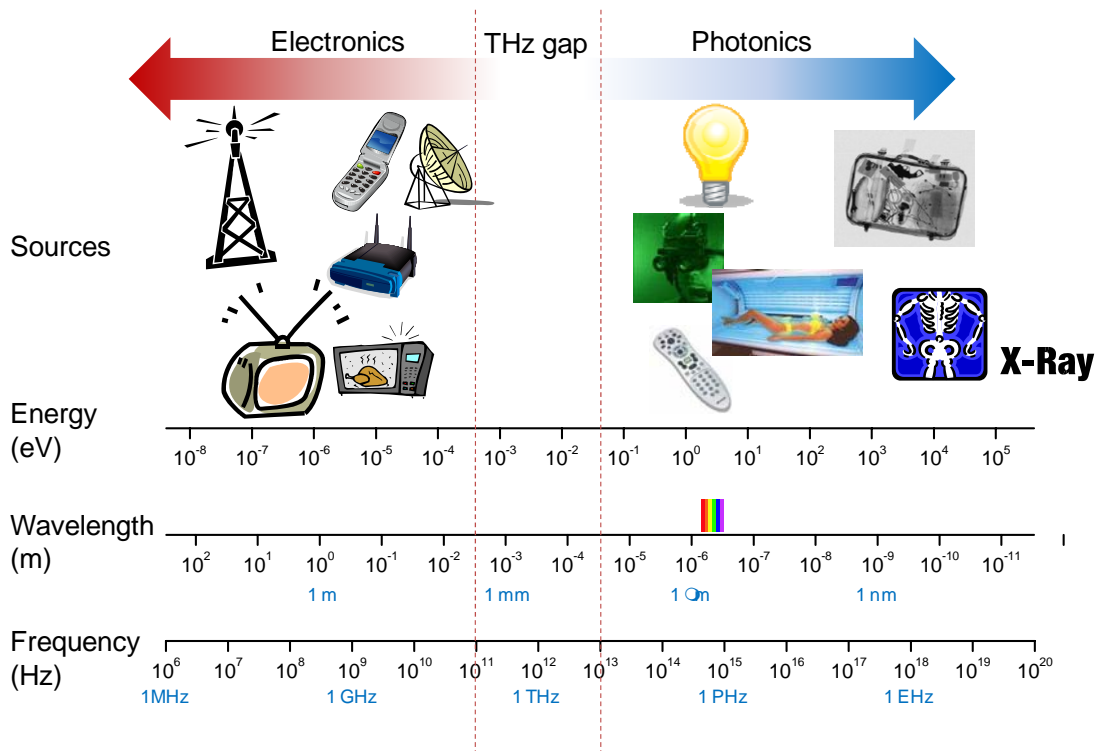
Figure 1-1 THz gap in the electromagnetic spectrum

THz waves, between electronic and optical frequency, have the following attractive characteristics: THz wave, like its lower frequency relative microwave, can penetrate most dielectric and dry materials, allowing the imaging of internal structure or concealed objects. THz wavelengths (0.03~3 mm) are shorter than that of microwaves, thus it provides better spatial resolution for imaging application. THz waves are low photon energy radiation (1 THz ~ 4 meV), and have no harmful effects on biological tissues. In contrast with THz, X-rays have photon energy in the keV range and have a potential of causing genetic damage and cancer. THz spectroscopy provides abundant information of unique rotational, vibration, and translational modes of the material, so can be used to identify many materials.

Due to these desirable characteristics, THz radiation has many potential applications in the following fields: communication, security, medical, inspection, and science (see Figure 1-2). THz can be used for short range wireless communication which will be a thousand times faster than the current wireless network. By reason of its harmless radiation and penetrating ability, THz radiation can be used for security screening for concealed weapons or explosives in airports [15]. Drug detection [16] and real time cancer screening [17] were also reported for pharmaceutical and medical imaging applications. For quality control (QC) applications, it has been used for non-destructive inspection of foam insulation sprayed on space shuttle [18][19] and IC package examination and testing [16][20]. Because of the rich spectroscopic information in the THz range, THz spectroscopy is an important technique for scientific studies in material science and astronomy.
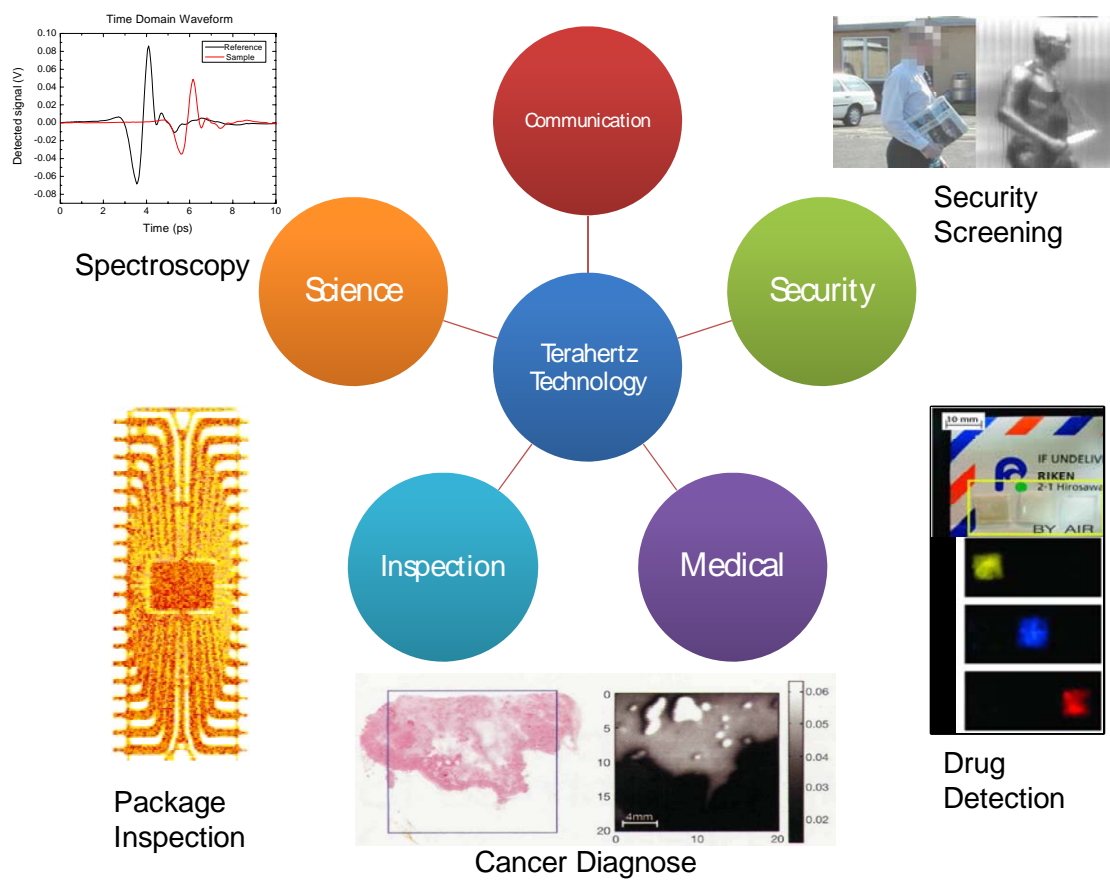
Figure 1-2 Applications for THz technology

Because of the low frequency nature of THZ waves (compared with other light sources), it is very sensitive to the presence of charge carriers. This is because the scattering frequency of charge carriers in a semiconductor is also in the THz region and as a result THz waves interact with charge carriers in a specific manner. These characteristics make THz an ideal radiation for probing charge carriers. Therefore, THz time domain spectroscopy becomes an important tool to investigate charge transport in a material.

THz time domain spectroscopy was first introduced in the 1980s by using photoconductive antennas as both emitter and detector [2]. The principle of THz generation and detection using photoconductive antennas is as follows: Ultrafast laser pulse shines on a biased photoconductive switch to generate transient photocurrent. The photo-induced rapidly varying current will emit electromagnetic radiation. This electromagnetic radiation has a wide band of frequencies and is in THz range. For THz detection, the electric field of THz radiation induces a transient bias voltage on the photoconductive switch. The amplitude and time dependence of this transient voltage are obtained by measuring the photoinduced current versus the time delay between the THz wave and the probing ultrafast laser pulses. This THz generation and detection method is widely applied in THz time domain spectroscopy for studying steady-state properties of materials. Another popular method for THz generation and detection in THz spectroscopy is optical rectification [1] and electro-optic sampling [5][7]. Optical rectification is a second-order nonlinear optics effect. THz pulses are generated when ultrafast optical pulses shine on the nonlinear crystal. Electro-optic sampling for sensing THz waves is measuring the polarization change of probe optical pulses due to the

electric field of THz pulses applied to the EO crystal. Because optical rectification is a second-order nonlinear optics effect, the intensity of THz pulses is proportion to the square of the intensity of optical pulses. For that reason, this method is suitable for an amplified laser system which has higher pulse energy, and is usually used in optical pump-THz probe time domain spectroscopy where high optical pumping intensity is desired. Optical pump-THz probe time domain spectroscopy is a technique combining THz radiation with visible pump pulses to investigate transient photoconductivity. A sample is excited by the optical pump pulse to generate photoinduced carriers, and then probed by the THz probe pulse. By delaying the THz probe pulses with respect to the optical pump pulse, the dynamics of photoinduced carriers can be traced in time.

1.3 Semiconducting polymer

Semiconducting polymers are based on π electrons on linear carbon chains. π electrons exist in conjugated polymers, which have atoms covalently bonded with alternating single and multiple bonds. Polyacetylene is the simplest conjugated polymer, as shown in Figure 1-3. Polyacetylene has sp2 hybridization and has a π bond in its double bond between the carbons. Pure (undoped) polyacetylene has very low conductivity around 10^{-10} to 10^{-8} /ohm-cm. However, after doping, the conductivity of the conjugated polymer could increase rapidly to many orders of magnitude higher. Alan J. Heeger, Alan MacDiarmid and Hideki Shirakawa reported metallic conductivity in iodine doped trans-polyacetylene in 1977 [56]. After that, many different semiconducting polymers were discovered and developed, thus the era of polymer electronics begun.

9

Heeger, MacDiarmid and Shirakawa were awarded the 2000 Nobel Prize in Chemistry for their contributions in conductive polymers.
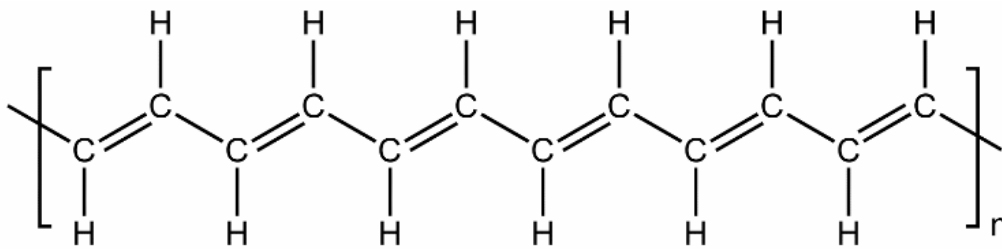
Figure 1-3 Structure of trans-polyacetylene

Semiconducting polymers, just like other plastic, have many favorable physical and chemical properties. Compared to conventional semiconductors, semiconducting polymers have the following advantages:

- Flexibility

- Lightweight

- Low cost

  - Easy to process (solution processibility, malleability)

  - Large area production (e.g. printing)

- Low toxicity

- Adjustable properties through functionalization

Like conventional semiconductors, semiconducting polymers have been used to make many electronic and photonic devices such as organic light-emitting diodes (OLED) [21], organic photovoltaics (OPV) [22][23], organic field-effect transistors (OFET) [24][25], and organic semiconductor lasers [26]. Combined with the desirable mechanical

10

properties of the polymers, these devices could be used to make potential products such as electric paper, foldable displays, flexible solar cells, and wearable computers.

For OPV applications, current organic solar cells still suffer from low power efficiency cmpared to conventional semiconductor solar cells. For single active layer organic solar cell devices, the highest efficiency achieved right now is about 5% [27]. Further increase to 6.7% can be obtained by applying multiple active layer architecture to absorb wider solar spectrum energy [28]. On the other hand, the power conversion efficiency of today's standard commercial semiconductor solar cells is about 10~20%, and the best reported efficiency of complex semiconductor multi-junction solar cells have been reported is 40% by National Renewable Energy Laboratory. To further improve the performance of the polymer OPV devices, detailed understanding the photo-initiated processes and carrier transport in semiconducting polymers is necessary.

1.4 Scope of thesis

The remainder of this thesis is separated into five chapters.

Chapter 2 discusses the principle and experimental method of THz time domain spectroscopy. In this study, we use optical rectification and electro-optic sampling to generate and detect THz radiation in our spectroscopy setup. In this chapter, we first will describe the principle of optical rectification and electro-optic sampling. A method to measure THz pulse energy and detector related distortion effects will be addressed in this part. The second part discusses experimental setup and analysis method, which includes Fourier analysis, single layer medium transmission analysis, and the simple Drude model.

The last part describes the experiments that measure the steady state electronic properties of Drude-like materials: doped silicon and an ITO film.

Chapter 3 is dedicated to optical pump-THz probe time domain spectroscopy. Unlike steady state THz spectroscopy, the transient photo-excited material properties may change during the THz probe time. An advanced analysis is required to obtain meaningful information from experimental data. In this chapter, we focus on two parts: The first part is about the theoretical derivation of the analysis technique. The artificial conductivity we obtain directly from the optical pump-THz probe time domain spectroscopy using the conventional analysis method suggested by Kindt and Schmuttenmaer will be derived [46]. A new analysis method regarding a series of transformations suggested by Nienhuys and Sundstrom [29] to obtain the true conductivity is also discussed in this part. The second part discuses the transient photoconductivity measurement of photoexcited GaAs. GaAs is a well known Drude-like material, and we use it as a benchmark sample to test the new analysis method. A comparison of the results using the new analysis method and the results obtained from the conventional method will be made.

Chapter 4 presents the study of photo-induced carrier dynamics in P3HT/PCBM blends. The different P3HT weight fraction blends, 0, 0.2, 0.5, 0.8, and 1, are studied with optical pump- THz probe time domain spectroscopy. The new analysis method enables us to resolve the transient photo-conductivity of these materials at sub-picosecond time scales. The conductivity is analyzed using the Drude-Smith model to determine the photon-to-carrier yield, average carrier mobility, and carrier density. A very fast conductivity dynamics in the first picosecond after photoexcitation is observed and

analyzed in terms of dynamics of carrier density and mobility. Long term conductivity (10~300 ps) is also measured and the role of PCBM in the P3HT matrix will be discussed.

Chapter 5 describes transient photoinduced properties of a semiconducting polymer, MEH-PPV. We use three different experiments to study the material: optical pump- THz probe time domain spectroscopy, DC-bias transient photoconductivity measurements, and photo-induced reflectivity change measurement. These experiments measure the properties at THz frequencies, DC, and optical frequencie, respectively. A model that combines the Drude-Smith model and the Lorentzian oscillator model is used to describe the behaviors of photoexcited carriers. The dynamics of free carriers, bound carriers, and phonons will be discussed in this chapter.

Chapter 6 concludes this thesis and suggests the future work.

Chapter 2: Terahertz Time Domain Spectroscopy

2.1 Introduction

For the typical terahertz (THz) time domain spectroscopy, THz pulses are required as a broadband radiation source to probe the material. There are several ways to generate THz pulses: the optical rectification effect [1][7], photo-conductive antenna [30], and semiconductor surface emission. The electric field of the THz pulses can be measured by the pump-probe technique where a detector is illuminated with a portion of the same laser pulses that are used to generate the THz. By changing the relative arrival time of THz pulses and probe pulses, one can measure the electric field of the THz wave in the time domain. Two typical detection methods used in THz spectroscopy are photoconductive switch sampling [30] and electro-optic sampling [1]. In our system, we use the optical rectification effect to generate THz pulses and electro-optic sampling for THz detection

In the first section, we will discuss the principle of optical rectification and electro-optic sampling. A method to estimate THz pulse energy by electro-optic sampling measurement and to estimate detector related distortion effects will also be addressed in this section. The second section discusses the experiment setup and the analysis method, which includes applying Fourier analysis, single layer medium transmission analysis, and the simple Drude model to extract physical properties in Drude-like materials. The last part describes the experiments that measure the steady state electronic properties of Drude-like materials: doped silicon and an ITO film.

2.2 THz generation and detection

2.2.1 THz generation: Optical Rectification

Optical rectification is a non-linear optical process which describes the generation of DC polarization accompanying the passage of an intense laser beam through certain crystals. It was observed for the first time by Bass et al. in 1962 when a high power ruby pulse laser (694.3 nm, 1 MW/pulse, 10^{-7} s duration) was transmitted through potassium dihydrogen phosphate (KDP) and potassium dideuterium phosphate (KD$_d$P) [31]. The phenomenon is the analogue of electric rectification which converts AC signal to DC. In nonlinear optics, optical rectification is a second-order nonlinear process and can be represented by [32]

$$P = \chi^{(2)}(0; \omega, -\omega) E(\omega) E^*(\omega) \quad .$$

(2.1)

For 100 femtosecond pulse laser, the bandwidth of the spectrum is about several THz, as shown in Figure 2-1. The nonlinear dielectric polarization due to optical rectification can be expressed as [27]

$$P_i(\Omega) = \int_{\omega_0 - \Delta\omega/2}^{\omega_0 + \Delta\omega/2} \chi_{ijk}^{(2)}(\Omega; \omega + \Omega, -\omega) E_j(\omega + \Omega) E_k^*(\omega) d\omega \quad ,$$

(2.2)

15

where ω_0 is the central frequency of the incident pulse, $\Delta\omega$ is the bandwidth of the incident pulse, and $\chi_{ijk}^{(2)}$ is the second order nonlinear optical susceptibility tensor element of the nonlinear crystal. According to the formula, because the bandwidth of incident ultra-fast pulses is several THz, the nonlinear crystal emits electromagnetic pulses whose frequencies are in THz range.
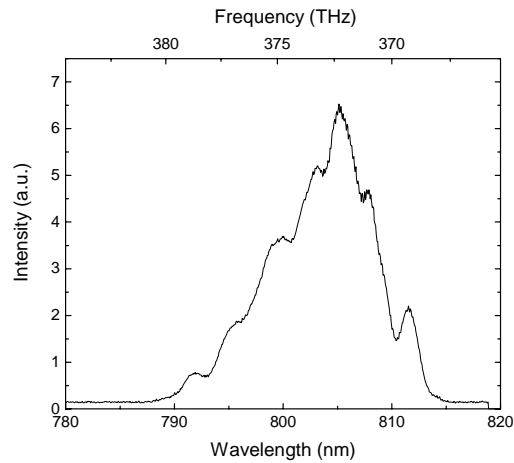
Figure 2-1 Typical spectrum of 800 nm, 100 fs duration pulse laser

Another trait of THz generation via optical rectification is that the electric field strength of generated THz waves is proportional to the input pump power. Figure 2-2 shows the measured THz electric field peak amplitude dependence with pump power. The nonlinear crystal for THz generation is 1mm thick [110] zinc telluride (ZnTe) and pump source is 800 nm, 100 fs, 1 kHz repetition rate pulse laser. The linear relationship between the THz field and incident pump laser power implies that THz generation efficiency is proportional to the square of the input laser power. Therefore THz

16

generation via optical rectification is more suitable for applications in amplified laser systems, which have high peak power in single pulse, than THz generation via the photoconductive antenna.
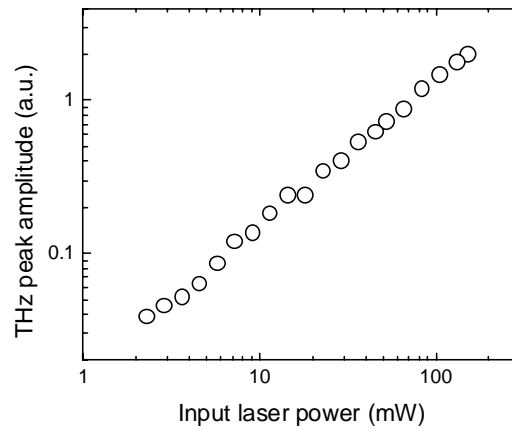
Figure 2-2 THz electric field peak amplitude vs. Input pulse laser power

For nonlinear optical crystals, second order nonlinear susceptibility only exists in noncentrosymmetric crystals. We use ZnTe as the nonlinear crystal for THz generation via optical rectification process. ZnTe is a zinc-blende crystal and has a cubic, $\overline{4}3m$ point-group symmetry. It has only one independent nonvanishing second-order nonlinear optical coefficient: $d_{14} = d_{25} = d_{36}$. It is a red color crystal and has an energy band-gap of 2.26 eV at room temperature. Under intense 800nm pulse irradiation, it will not only generate THz radiation via optical rectification, but also emit green fluorescence light due to two photon absorption.

In order to increase THz generation efficiency, longer interaction lengths (thicker crystal) are desirable. However, the phase matching condition limits the maximum

thickness of the crystal. The phase matching condition for the optical rectification can be expressed as

$$k(\omega_{opt} + \omega_{THz}) - k(\omega_{opt}) - k(\omega_{THz}) = 0 \quad , \tag{2.3}$$

where $k(\omega_{opt} + \omega_{THz})$ and $k(\omega_{opt})$ are the angular wavenumbers of different frequency components of the aser pulse, $k(\omega_{THz})$ is the angular wavenumber of the THz wave, ω_{opt} and ω_{THz} are the angular frequency of the laser pulse and THz wave. From (2.3), we get

$$\frac{k(\omega_{THz})}{\omega_{THz}} = \frac{k(\omega_{opt} - \omega_{THz}) - k(\omega_{opt})}{\omega_{THz}} \cong \left(\frac{\partial k}{\partial \omega} \right)_{opt} \quad . \tag{2.4}$$

The left hand side $\dfrac{k(\omega_{THz})}{\omega_{THz}}$ is the phase velocity of the the THz wave, and the right hand side $\left(\dfrac{\partial k}{\partial \omega} \right)_{opt}$ is the group velocity (speed of envelop of the wave) of the laser pulses. The relation indicates that when the phase velocity of THz wave is equal to the group velocity of the optical wave (the velocity of the pulse envelope), the phase matching condition is achieved. The coherence length l_c may be derived as [7]

$$l_c = \frac{\pi c}{\omega_{THz} \left| n_{opt} - \lambda_{opt} \left(\dfrac{dn_{opt}}{d\lambda} \right)_{\lambda_{opt}} - n_{THz} \right|} \quad , \tag{2.5}$$

18

where c is speed of light, n_{opt} is the optical (800 nm) index of the refraction of the crystal, and n_{THz} is the THz index of the refraction of the crystal. Using Equation (2.5), the relationship of coherence length and THz frequency for ZnTe by pumping with 800 nm pulses can be calculated and the result is shown in Figure 2-3. The data show that good phase matching is achieved for 1-mm-thick ZnTe when the THz frequency is below 2.3 THz. Figure 2-4 shows the amplitude spectrum of THz radiation generated and detected by two 1-mm-thick [110] ZnTe crystals. The useful frequency range from 0.2 THz to 2.3 THz basically agrees with the phase matching theorem.
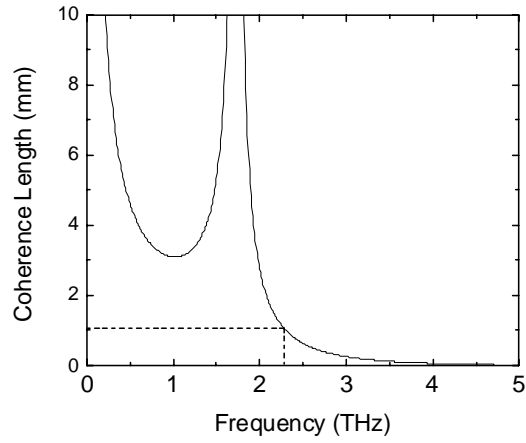
Figure 2-3 The calculation result of the coherence length vs THz frequency for ZnTe using 800 nm beam.

The dotted line indicates the coherence length for 1-mm thick ZnTe crystal.
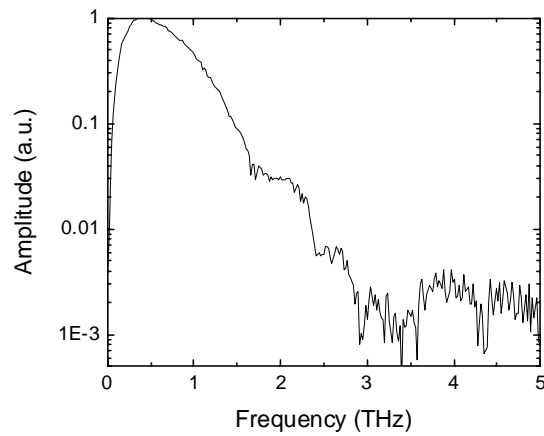
Figure 2-4 THz amplitude spectrum using a 100 fs pulsed laser at 800 nm and generation and detection via

two 1-mm thick [110] cut ZnTe crystal.

2.2.2 THz detection

2.2.2.1 Electro-optic sampling

Electro-optic sampling uses the linear electro-optic effect, also called that the Pockels effect, to measure the strength of the electric field (both positive and negative) which varies slower than the duration of optical probe pulses. The resolution of the technique depends on the duration of the optical probe pulses. When ultrafast optical pulses are used in the electro-optic sampling, the electric field of THz pulses can be mapped out by slowly varying the arrival time of the optical probe pulses without requiring very fast photodetectors. For each setting of the relative time delay, the optical probe is influenced by the small portion of the THz electric field which arrives at the detector crystal at the same time as the optical probe pulse. The polarization change of the probe pulse is proportional to the strength of the THz electric field, and can be averaged over many pulses to average out noise in order to achieve very high signal to noise ratio. Figure 2-5 shows the mechanism of the electro-optic sampling.

The Pockels effect describes the phenomenon that the change of refractive index depends linearly on the strength of the applied electric field in some materials. The linear electro-optic effect can be expressed in terms of a nonlinear polarization[32]:

21
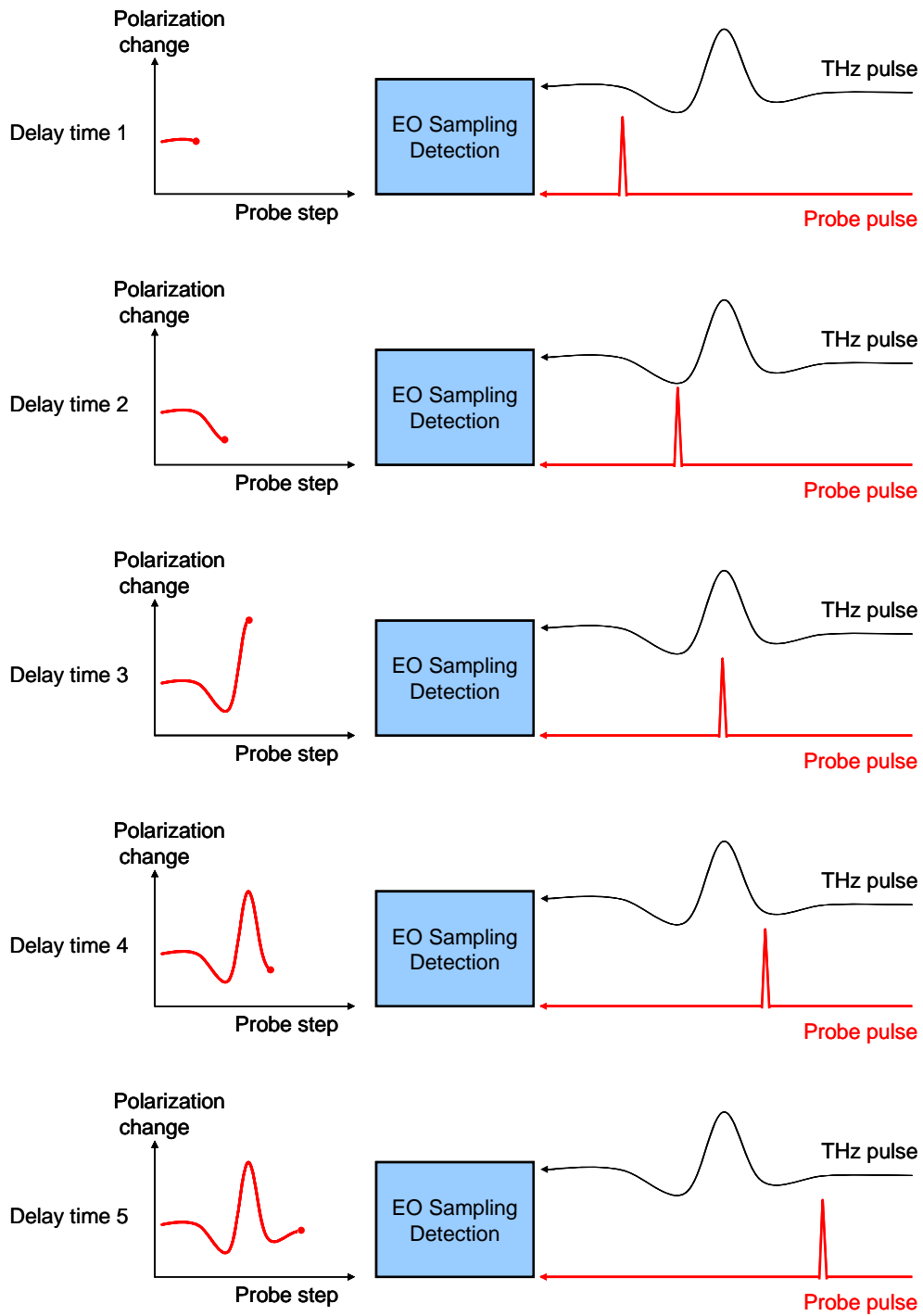
Figure 2-5 Mechanism of electro-optic sampling

$$P_i(\omega) = 2\sum_{jk} \chi_{ijk}^{(2)}(\omega = \omega + 0)E_j(\omega)E_k(0) \quad .$$

(2.6)

This is a second-order optical nonlinearity, and therefore this effect only exists in noncentrosymmetric materials.

In our system, we use a [110], 1 mm thick ZnTe crystal as the nonlinear crystal to detect the THz electric field. Figure 2-6 shows the experimental setup of electro-optic sampling for THz electric field detection. The THz pulse and optical probe pulse are collinear and arrive as the ZnTe crystal simultaneously. After the crystal, the probe beam passes through a quarter wave plate and a Wollaston prism, which is a polarizing beam splitter that separates the two orthogonal polarization components. The difference of the intensities of the two polarization components are then measured by a balanced detector. The relationship of this difference signal to the THz E-field reques a detailed discussion of the electro-optic effect for ZnTe in this experimental setup.
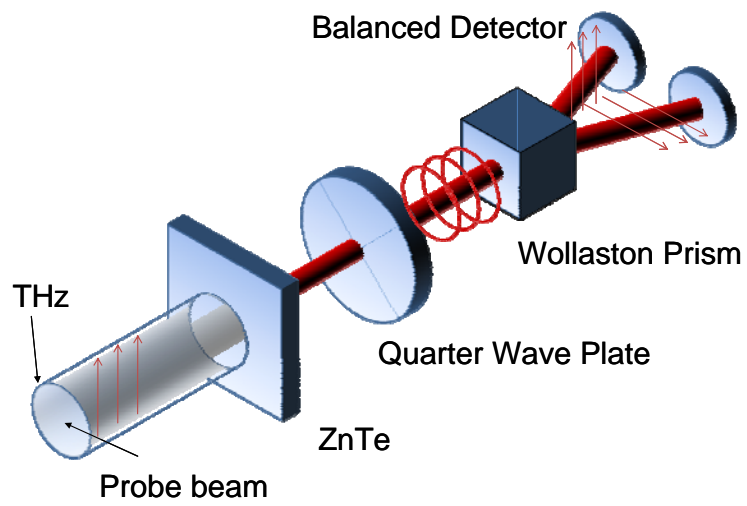
Figure 2-6 Experimental setup of electro-optic sampling for THz Electric field detection.

ZnTe is a zinc-blende crystal and has a cubic, $\overline{4}3m$ point-group symmetry. Its electro-optic tensor can be written as

$$
r_{ij} = \begin{vmatrix} 0 & 0 & 0 \\ 0 & 0 & 0 \\ 0 & 0 & 0 \\ r_{41} & 0 & 0 \\ 0 & r_{41} & 0 \\ 0 & 0 & r_{41} \end{vmatrix} \quad ,
$$

(2.7)

where $r_{41} = 3.9$ pm/V for ZnTe [33]. The index ellipsoid in the presence of the THz field is given by

$$
\frac{x^2}{n^2} + \frac{y^2}{n^2} + \frac{z^2}{n^2} + 2r_{41}E_x yz + 2r_{41}E_y xz + 2r_{41}E_z xy = 1 \quad ,
$$

(2.8)

where E_x, E_y, and E_z are the THz electric field components along [100], [010], and [001] direction. Because the ZnTe crystal we use is [110] cut, we first make the transformation around z axis with a rotation $45°$

$$
x = \frac{\sqrt{2}}{2} x' - \frac{\sqrt{2}}{2} y' \quad ,
$$
$$
y = \frac{\sqrt{2}}{2} x' + \frac{\sqrt{2}}{2} y' \quad ,
$$
$$
z = z' \quad .
$$

(2.9)

The index ellipsoid becomes:

25

$$x'^2(\frac{1}{n^2}+r_{41}E_z)+y'^2(\frac{1}{n^2}-r_{41}E_z)+\frac{z'^2}{n^2}+2\sqrt{2}r_{41}E_xy'z'=1 \quad .$$

<div align="right">(2.10)</div>

In order to eliminate the mixed term to align the coordinate system with the major axes of the ellipsoid, another transformation is taken:

$$x' = x'' \quad ,$$
$$y' = y''\cos\theta - z''\sin\theta \quad ,$$
$$z' = y''\sin\theta + z''\cos\theta \quad ,$$

<div align="right">(2.11)</div>

and let

$$E_z = E_{THz}\cos\alpha, E_x = E_{THz}\frac{\sqrt{2}}{2}\sin\alpha \quad ,$$

<div align="right">(2.12)</div>

where α is the angle of the THz polarization with respect to the [001] axis, as shown in Figure 2-7. The final ellipsoid can be solved as:

$$x''^2(\frac{1}{n^2}+r_{41}E_{THz}\cos\alpha)$$
$$+y''^2\{\frac{1}{n^2}-r_{41}E_{THz}[\cos\alpha\sin^2\theta+\cos(\alpha+2\theta)]\}$$
$$+z''^2\{\frac{1}{n^2}-r_{41}E_{THz}[\cos\alpha\cos^2\theta-\cos(\alpha+2\theta)]\}=1 \quad ,$$

<div align="right">(2.13)</div>

where

<div align="center">26</div>

$$\theta = -\frac{1}{2}\arctan(2\tan\alpha) + n\pi \quad . \tag{2.14}$$

We therefore can get the refractive index along the $y"$ axis

$$\frac{1}{n_{y"}^2} = \frac{1}{n^2} - r_{41}E_{THz}[\cos\alpha\sin^2\theta + \cos(\alpha + 2\theta)]$$

$$\Rightarrow n_{y"} \approx n + \frac{n^3}{2}r_{41}E_{THz}[\cos\alpha\sin^2\theta + \cos(\alpha + 2\theta)] \quad . \tag{2.15}$$

And similarly for the index along $x"$,

$$n_{z"} \approx n + \frac{n^3}{2}r_{41}E_{THz}[\cos\alpha\cos^2\theta - \cos(\alpha + 2\theta)] \quad . \tag{2.16}$$

Right now we have the principle ellipsoid angle $\theta(\alpha)$ with respect to the [001] axis, see Figure 2-7, and the principal refractive indices $n_{y"}(\alpha)$ and $n_{z"}(\alpha)$. If we assume that the polarization of the probe beam is parallel to the normal direction of the optical table, that the angle of the quarter wave plate axis is $45°$ with respect to the polarization of probe beam, and that the angle between [001] of ZnTe and the polarization of probe bream is ϕ (see Figure 2-7), then the probe beam polarization after the quarter wave plate can be calculated using Jones calculus,

27
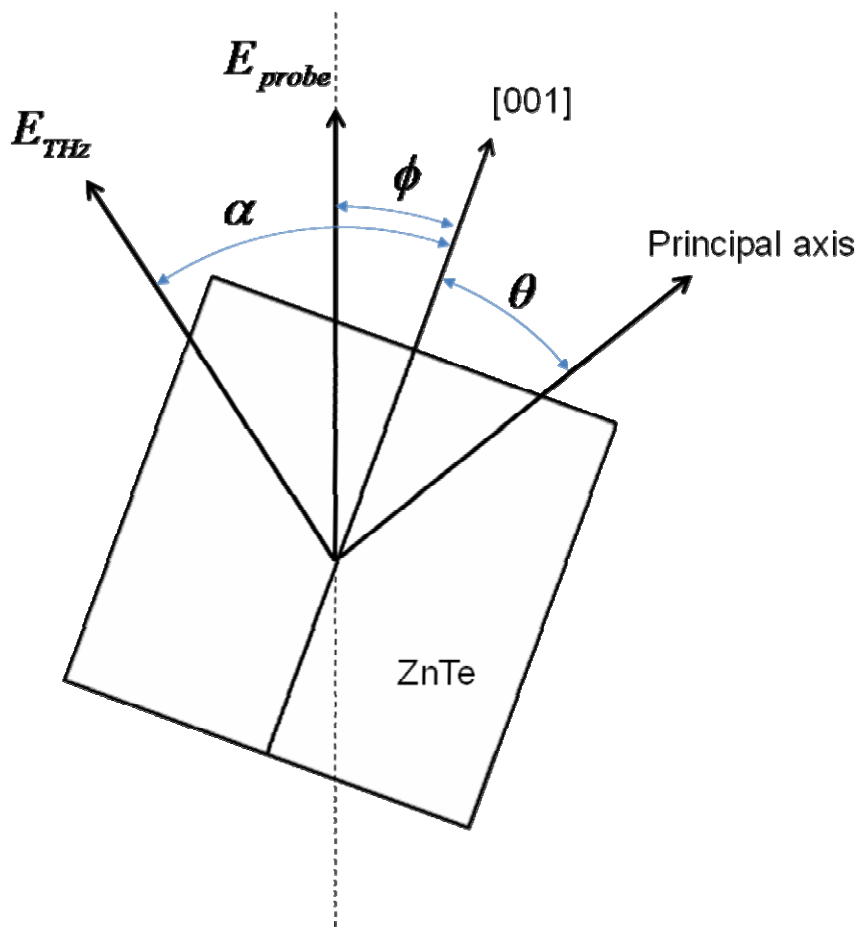
Figure 2-7 Angles of the probe beam and THz polarization with respect ro the ZnTe [001] axis.

$$\begin{pmatrix} E_\perp \\ E_{/\!/} \end{pmatrix} = R(-45°)\begin{pmatrix} 1 & 0 \\ 0 & i \end{pmatrix}R(45°)R(-\phi+\theta)\begin{pmatrix} \exp(-i\dfrac{\omega n_{y^"}L}{c}) & 0 \\ 0 & \exp(-i\dfrac{\omega n_{z^"}L}{c}) \end{pmatrix}R(\phi-\theta)\begin{pmatrix} 1 \\ 0 \end{pmatrix},$$

$$\tag{2.17}$$

where $R(\varphi)=\begin{pmatrix} \cos(\varphi) & \sin(\varphi) \\ -\sin(\varphi) & \cos(\varphi) \end{pmatrix}$ and L is the thickness of ZnTe. After passing through

the Wollaston prism, the two polarization components of the probe beam are detected by

the balanced detector, and the difference intensity can be derived[34],

$$\Delta I(\alpha,\phi) = I_p \sin[2(\phi-\theta(\alpha))]\sin[\frac{\omega L}{c}(n_{y^"}(\alpha)-n_{z^"}(\alpha))].$$

$$\tag{2.18}$$

Using Eq. (2.14), (2.15), and (2.16), the equation can be simplified to:

$$\frac{\Delta I(\alpha,\phi)}{I_p} = \frac{\omega n^3 E_{THz}r_{41}L}{2c}(\cos(\alpha)\sin(2\phi)+2\sin(\alpha)\cos(2\phi)).$$

$$\tag{2.19}$$

According to equation (2.19), the signal gathered from the balanced detector is

proportional to the amplitude of the THz electric field and to the intensity of the optical

probing beam, as shown in Figure 2-2 and Figure 2-9. Figure 2-8 shows the detected

signal dependence on the ZnTe azimuth angle ϕ, which is well predicted by equation

(2.19).
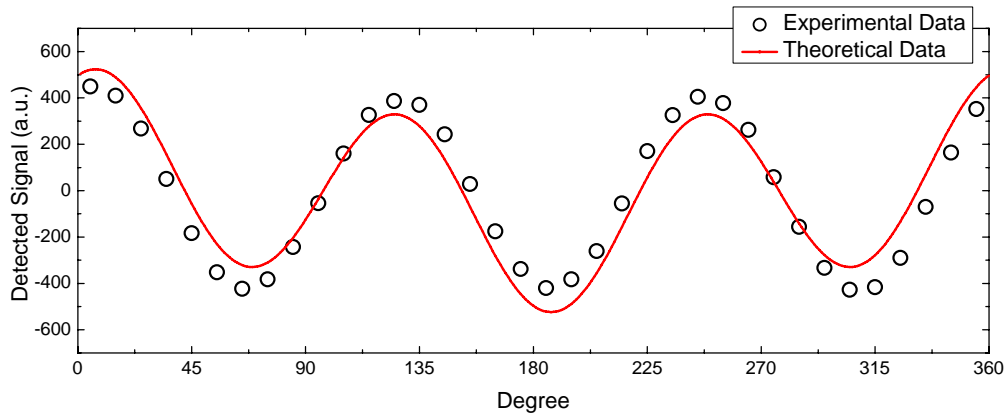
Figure 2-8 Detected signal dependence on the ZnTe azimuth angle ϕ. The line is theoretical fit using equation (2.19).
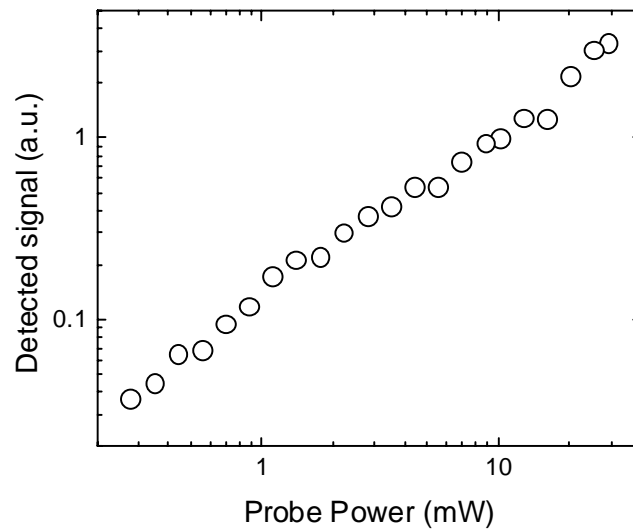
Figure 2-9 Linear response of detector by varying the probe beam power.

2.2.2.2 THz pulse energy detection

The conventional method to measure the energy of THz pulses uses bolometers. However, to achieve good sensitivity, they have to be cooled by liquid helium, because the principle of bolometers is to measure the temperature increase due to the absorption of incoming electromagnetic waves. Another way to measure the energy involves estimating the strength of the THz electric field by electro-optic sampling using equation (2.19)[35]. If $\Delta I_{probe} = I_1 - I_2$ is the intensity difference measured by the two detectors of the balanced detector, and the intensity of the probe beam can be expressed as $I_{probe} = I_1 + I_2$, then in our system, the ratio $\Delta I_{probe} / I_{probe}$ is 0.05 when measuring the peak amplitude. Using the 1-mm-thck, [110] oriented ZnTe crystal, the peak THz electric field is, from equation (2.19):

$$
\begin{aligned}
E_{THz} &= \frac{\Delta I_{probe}}{I_{probe}} \cdot \frac{\lambda}{2\pi \cdot n^3 \cdot r_{41} \cdot L} \\
&= 0.05 \cdot \frac{800 \times 10^{-9}}{2\pi \cdot (2.8)^3 \cdot 3.9 \times 10^{-12} \cdot 1 \times 10^{-3}} \\
&= 7.4 \times 10^4 (V/m) \quad .
\end{aligned}
\tag{2.20}
$$

The spot size of THz pulse on ZnTe crystal is about 2 mm, thus the total energy of single THz pulse can be calculated by the electromagnetic wave formula:

$$
\begin{aligned}
Energy &= \int \varepsilon_0 E(x)^2 dx \cdot A \\
&\cong 20(pJ) \quad .
\end{aligned}
\tag{2.21}
$$

With $350\,\mu$J of the input 800nm pulse energy for THz generation, the estimated THz generation efficiency is about 10^{-7}.

2.2.2.3 Detector response function

From section 2.1.2 we get from equation (2.19) that the signal from the balanced detector is proportional to the electro-optic coefficient, propagation length, probe intensity, and THz electric field:

$$\Delta I \propto r_{41} L I_p E_{THz} \quad .\tag{2.22}$$

The derivation is based on the assumption that the phase is perfectly matched between the THz pulse and the optical probe pulse. When the phase matching issue is considered, equation (2.19) can be rewritten as [36][37]

$$\Delta I(\tau) \propto \int_0^L dz \int_{-\infty}^{+\infty} I_p(z, t-\tau) P_{EO}(z,t) dt \quad , \tag{2.23}$$

where $P_{EO}(z,t)$ is the propagating EO pulse:

$$P_{EO}(z,t) \propto \int_{-\infty}^{+\infty} \chi_{eff}^{(2)}(\omega_0; \Omega, \omega_0 - \Omega) E_{THz}(\Omega) \exp[ik(\Omega)z] \exp(-i\Omega t) d\Omega \quad . \tag{2.24}$$

The propagation speed of the THz pulse and the optical probe pulse may be different for different frequency components. The sensitivity of the crystal at different frequencies

32

may also be different when the second order susceptibility is a function of the frequency. Therefore, the desired signal $E_{THz}(z,t)$ would be distorted by the detecting system. The equation (2.23) can be rewritten in the frequency domain [37] as

$$\Delta I(\tau) \propto \int_{-\infty}^{+\infty} E_{THz}(\Omega) f(\Omega) \exp(-i\Omega\tau) d\Omega \quad . \tag{2.25}$$

Here $f(\Omega)$ is the detector response function and can be expressed as

$$f(\Omega) = C_{opt}(\Omega) \chi_{eff}^{(2)}(\omega_0; \Omega, \omega_0 - \Omega) \frac{\exp(i\Delta k(\omega_0,\Omega)L) - 1}{i\Delta k(\omega_0,\Omega)} \quad , \tag{2.26}$$

where $C_{opt}(\Omega)$ is the autocorrelation of the optical probe pulse:

$$C_{opt}(\Omega) = \int_{-\infty}^{+\infty} E_{opt}^*(\omega - \omega_0) E_{opt}(\omega - \omega_0 - \Omega) d\omega \quad , \tag{2.27}$$

and $\Delta k(\omega_0,\Omega)$ is the phase mismatch between THz pulse and optical probe pulse:

$$\Delta k(\omega_0,\Omega) = k(\Omega) - \Omega \left(\frac{dk}{d\omega} \right)_{\omega_0} \quad . \tag{2.28}$$

Figure 2-10 shows the calculated detector response function of 1-mm-thick [110] ZnTe crystal using the index of refraction and absorption data for ZnTe from ref. [38].
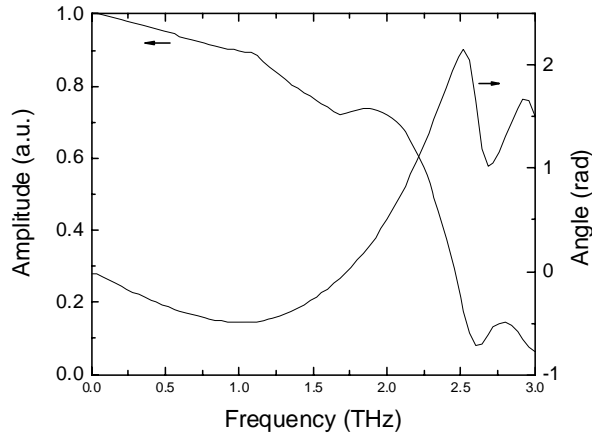
Figure 2-10 Detector response function of 1-mm thick [110] ZnTe crystal.

In steady state THz spectroscopy measurements (which means that the properties of the investigated sample are not time dependent), two measurements are taken: one is with the sample; another is without the sample. The two measured signals will be transferred to the frequency domain and divided by each other in order to obtain the transmission coefficient. We can easily prove that the ratio of the two distorted signals is equal to the ratio of two undistorted signals using equation (2.25):

$$\frac{\Delta I_{sample}(\Omega)}{\Delta I_{ref}(\Omega)} = \frac{E_{THz-sample}(\Omega)f(\Omega)}{E_{THz-ref}(\Omega)f(\Omega)} = \frac{E_{THz-sample}(\Omega)}{E_{THz-ref}(\Omega)} \quad . \tag{2.29}$$

From equation (2.29), except for changes in spectral coverage, the consideration of the distortion due to electro-optical sampling does not affect the THz analysis. However, this effect should be taken into account in a non-steady state measurement and will be discussed in the next chapter.

34

2.3 Experiment setup and Analysis

2.3.1 Experiment setup
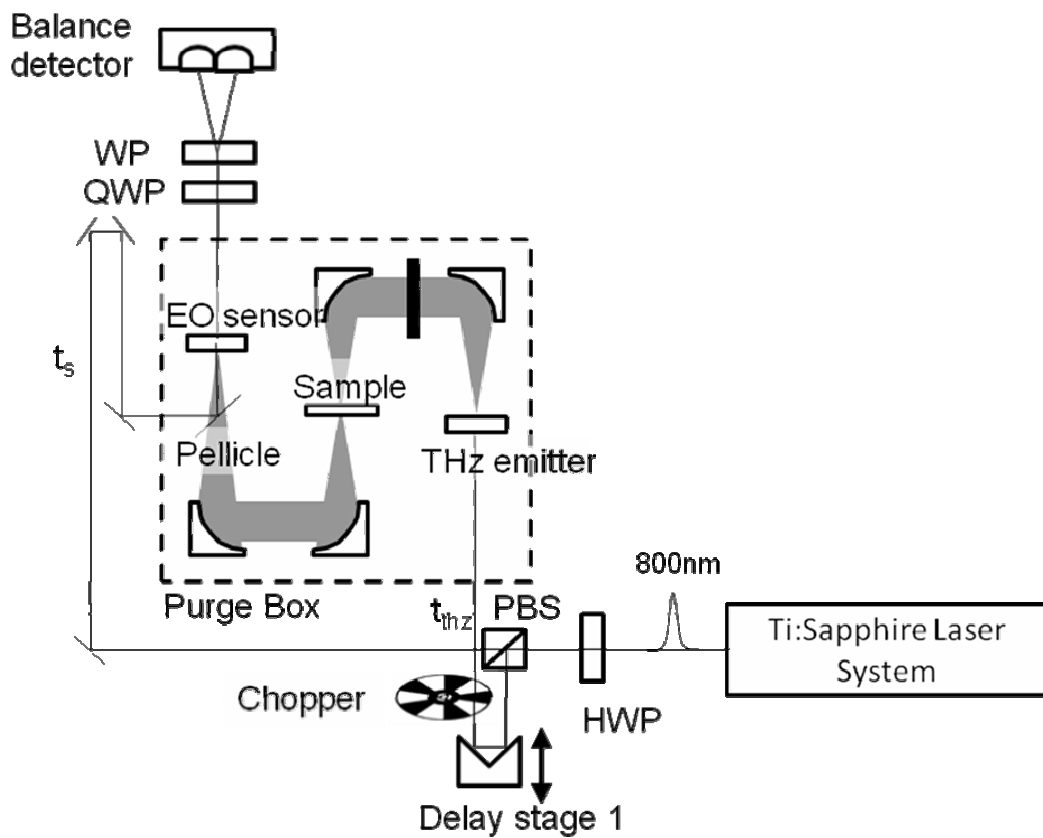
Figure 2-11 Schematic drawing of the experimental setup for THz-TDS

The optical pump-THz probe TDS setup is shown schematically in Figure 2-11. A Ti:Sapphire regenerative amplifier system (Spectra Physics Hurricane) provides a 1 kHz pulse train at a wavelength of 800nm with 120 fs pulse duration (full width half maximum, FWHM, see Figure 2-12 for autocorrelation measurement results) and 1

mJ/pulse energy. The beam is split into two parts. Most of the beam (> 99%) goes to a 1-mm-thick [110] cut ZnTe crystal to generate THz pulses via optical rectification. The remaining part of the beam (< 1%) is used to detect the terahertz radiation via another 1-mm-thick [110] cut ZnTe crystal by electro-optical sampling.
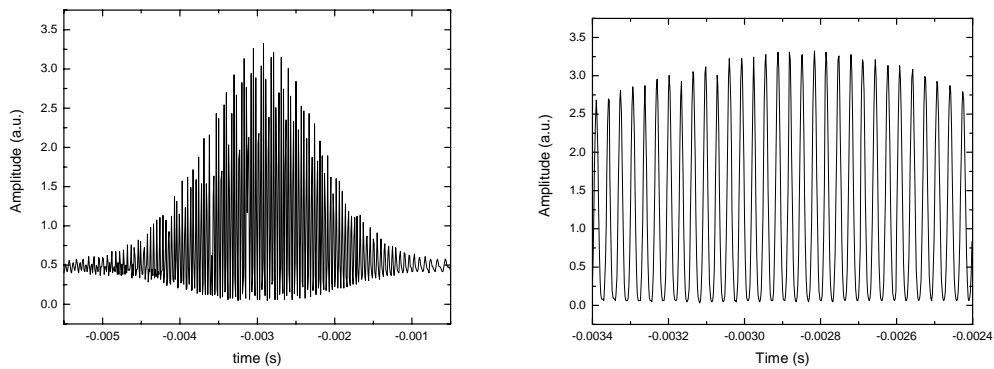
Figure 2-12 Left: autocorrelation measurement result for the 120 fs, 800nm pulse laser; Right: Zoom in plot of the left for higher time resolution.

To increase the sensitivity of the terahertz system, several detecting techniques are applied. A balance detector is used to measure the small polarization change in electro-optic sampling. The signal is gated by boxcar to reduce the background noise. A lock-in amplifier phase-locks with a chopper, which modulates the 800nm laser beam that generates terahertz radiation for measuring the terahertz amplitude.

The whole terahertz beam path from the transmitter to the receiver is enclosed and purged with dry nitrogen, because water vapor absorbs THz radiation strongly at some frequencies. Figure 2-13 shows the terahertz measurement results of the freely

propagating terahertz beam in dry air and in humid air. The water vapor absorption lines are indicated by the arrows[38].
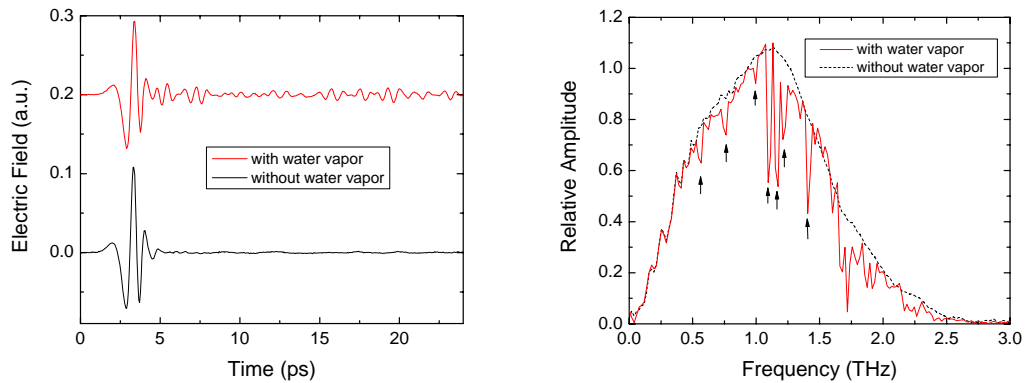
Figure 2-13 (left) THz waveform measurement under humid (top) and dry (bottom) environment. Note the waveform ringing of the top curve in the later time is due to water absorption; (right) THz Amplitude spectrum of the two waveforms.

2.3.2 Analysis

2.3.2.1 Transformation from time domain to frequency domain

The raw data we gathered in the THz spectroscopy is the THz electric field in the time domain. Instead of the data in time domain, sometimes THz spectrum in the frequency domain is more desirable for analysis purpose. Fourier analysis can help us do

such kind of transformation. Since the raw data we collected is discrete in the time domain, we use the discrete Fourier transformation:

$$g(f_k) = \sum_{n=0}^{N-1} f(t_n) \exp(-i \cdot 2\pi \cdot f_k \cdot t_n) \quad ,$$

(2.30)

where $f(t_n)$ is the discrete data in the time domain, $g(f_k)$ is the transformed data in the frequency domain (also discrete), $t_n = n\tau$, n is the index of the data and τ is the time interval of the measurement. The discrete frequency f_k can be expressed as:

$$f_k = \frac{k}{N\tau} \quad ,$$

(2.31)

where k=0,…,N-1, and N is the total number of data points in the time domain. From the above equation we can conclude that the frequency resolution and highest available frequency in the frequency domain depends on the total measuring time and the time resolution of the data in the time domain. To obtain a wider frequency span and higher frequency resolution, a higher time resolution and longer time scan in the time domain are required respectively.

2.3.2.2 Transmission for single layer medium
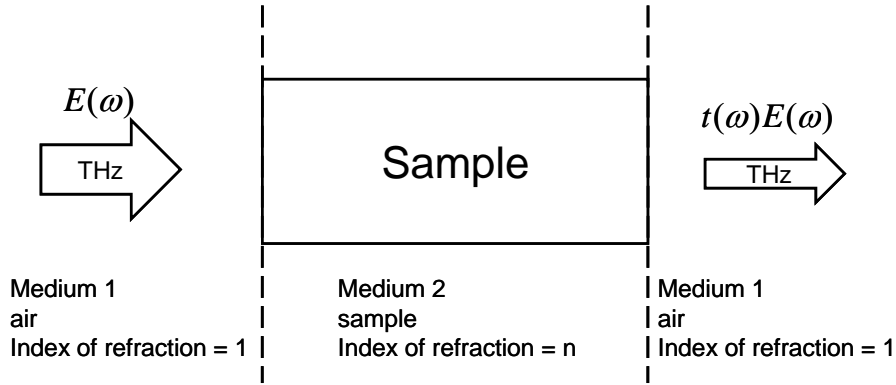
Figure 2-14 Transmission of single layer medium

In THz-TDS measurement, the transmitted THz waveform is measured when a sample is placed in the path of the THz beam. Considering the multiple reflection effect, the transmitted THz wave for a single layer medium can be expressed by[40]

$$t(\omega) = \frac{t_{12}t_{21}\exp(-\dfrac{\omega d}{c}n_i)\exp(i\dfrac{\omega d}{c}n_r)}{1+r_{12}r_{21}\exp(-\dfrac{2\omega d}{c}n_i)\exp(i\dfrac{2\omega d}{c}n_r)} \quad ,$$

(2.32)

where n_r and n_i are the real and imaginary parts of the index of refraction of the medium,

$n= n_r +n_i,\ t_{12}t_{21} = \dfrac{4n}{(1+n)^2}$, $r_{12}r_{21} = \dfrac{1-n}{1+n}\times\dfrac{n-1}{n+1}$, d=sample thickness, c= light speed,

ω =THz frequency. By dividing the sample signal by the reference signal,

$E_{ref}(\omega) = E(\omega)\exp[i\dfrac{\omega d}{c}]$, we get

$$\frac{E_{sam}(\omega)}{E_{ref}(\omega)} = \frac{t_{12}t_{21}\exp(-\dfrac{\omega d}{c}n_i)\exp[i\dfrac{\omega d}{c}(n_r-1)]}{1+r_{12}r_{21}\exp(-\dfrac{2\omega d}{c}n_i)\exp(i\dfrac{2\omega d}{c}n_r)} \quad . \tag{2.33}$$

$E_{sam}(\omega)/E_{ref}(\omega)$ on the left hand side can be obtained from the measured data. By separating the real and imaginary parts of equation (2.33), we can solve numerically for the real and imaginary parts of the index of refraction as a function of frequency. Once we have the real and imaginary parts of the index of refraction, the complex dielectric constant can be obtained by

$$\varepsilon = \varepsilon_r + i\varepsilon_i = (n_r + in_i)^2 \quad . \tag{2.34}$$

The complex dielectric constant and complex conductivity have the following relation:

$$\varepsilon = \varepsilon_{w/o} + i\sigma/(\omega\varepsilon_0) \quad , \tag{2.35}$$

where $\varepsilon_{w/o}$ is the dielectric constant without free carrier presented (or undoped dielectric constant in the semiconductor). When the dielectric constant is measured, the complex conductivity can be calculated as

$$\sigma = -i\omega\varepsilon_0(\varepsilon - \varepsilon_{w/o}) \quad . \tag{2.36}$$

40

2.3.2.3 Drude model

The Drude model of electrical conduction was developed by Paul Drude in 1900 to explain the transport properties of electrons in conductors. It assumes that the motion of electrons is driven by an applied electric field and damped by a frictional force due to collisions of the electrons with the ions:

$$m^* \frac{d}{dt} v_d(t) - \gamma m^* v_d(t) = -eE(t) \quad , \tag{2.37}$$

where v_d is the drift velocity, m^* is the effective mass, and γ is the scattering rate. The differential equation has the solution for an applied sinusoidal field $E(t) = E_0 e^{-i\omega t}$:

$$v_d = -\frac{e}{m^*} \frac{1}{\gamma - i\omega} E_0 e^{-i\omega t} \quad . \tag{2.38}$$

The electron mobility is a quantity determined by the drift velocity of electrons and the applied electric field across a material. It can be written as

$$\mu(\omega) = \left| \frac{v_d}{E} \right| = \frac{e}{m^*} \frac{1}{\gamma - i\omega} \quad . \tag{2.39}$$

The electrical conductivity is equal to the product of carrier density, single carrier charge, and carrier mobility. Using the mobility obtained above, we get

41

$$\sigma(\omega) = Ne\mu(\omega) = \frac{i\varepsilon_0 \omega_p^2}{\omega + i\gamma} \quad, \tag{2.40}$$

where ω_p is the plasma frequency and $\omega_p^2 = \dfrac{Ne^2}{\varepsilon_0 m^*}$. If the value of the complex

conductivity is known, the plasma frequency and damping rate can be calculated:

$$\gamma = \frac{\sigma_r}{\sigma_i}\omega \quad,$$

$$\omega_p = \sqrt{\frac{\sigma_i \omega}{\varepsilon_0}[1 + \left(\frac{\sigma_r}{\sigma_i}\right)^2]} \quad. \tag{2.41}$$

Using the plasma frequency and damping rate, we can calculate the carrier density and

carrier mobility if the effective mass m^* is known:

$$N = \frac{\omega_p^2 \varepsilon_0 m^*}{e^2} \quad,$$

$$\mu = e/(m^*\gamma) \quad. \tag{2.42}$$

2.3.2.4 Summary of analysis process

The chart shows a flow diagram. Left column:

Transmitted THz Waveform in time domain

Fourier transform

THz amplitude and phase in frequency domain

Transmission analysis

$$\frac{E_{sam}}{E_{ref}} = \frac{t_{01}t_{10}\exp\left(i\frac{\omega L}{c}(\tilde{n}_1 - \tilde{n}_0)\right)}{1 + r_{01}r_{10}\exp(i\frac{2\omega L}{c}\tilde{n}_1)}$$

Complex index of refraction of sample

Right column:

Drude model

$$\varepsilon = \varepsilon_r + i\varepsilon_i = (n_r + in_i)^2$$
$$\varepsilon = \varepsilon_{w/o} + i\sigma/(\omega\varepsilon_0)$$

Complex Conductivity

$$\upsilon = \frac{\sigma_r}{\sigma_i}\omega$$
$$\omega_p = \sqrt{\frac{\sigma_i\omega}{\varepsilon_0}[1 + (\frac{\sigma_r}{\sigma_i})^2]}$$

Plasma frequency and Damping rate

$$N = \frac{\omega_p^2\varepsilon_0 m*}{e^2}$$
$$\mu = \frac{e}{m*\upsilon}$$

Carrier density and Mobility

Chart 1 THz-TDS data analysis procedure

Chart 1 shows the procedure of THz-TDS data analysis. The analysis procedure has the following steps:

1. Measure the THz waveforms with and without sample in the THz path.

2. Transfer time domain data to frequency domain by Fourier transformation.

3. Calculate the complex index of refraction of the sample by solving the transmission formula (2.33).

4. Calculate the complex conductivity.

5. Calculate the plasma frequency and scattering rate by Drude model.

6. Calculate the carrier density and mobility.

2.4 Measurements

2.4.1 Silicon measurement

Silicon is a well-known Drude like material. In this measurement, we use a silicon wafer as a benchmark sample to test our THz-TDS. The properties such as carrier density, dc conductivity, and carrier mobility will be extracted and compared with the manufacture's data sheet.

The silicon sample we used to test our terahertz time domain spectroscopy is a 260-um-thick sample of 1~5 ohm-cm, double side polished p-type silicon. The doping level of the p-type silicon is about $2.7 \times 10^{15} \sim 1.4 \times 10^{16} cm^{-3}$. Figure 2-15 (top) shows the THz pulse transmitted through the sample (sample pulse) and the reference THz pulse with no sample present (reference pulse). The peak amplitude of the sample pulse is about 50% of that of the reference pulse. The sample pulse amplitude and shape changed due to reflection losses, frequency-dependent absorption and dispersion of the sample. Figure 2-15 (bottom left) and Figure 2-15 (bottom right) show the frequency dependent amplitude and phase of these two pulses after Fourier transforming the time domain data in Figure 2-15 (top).

44
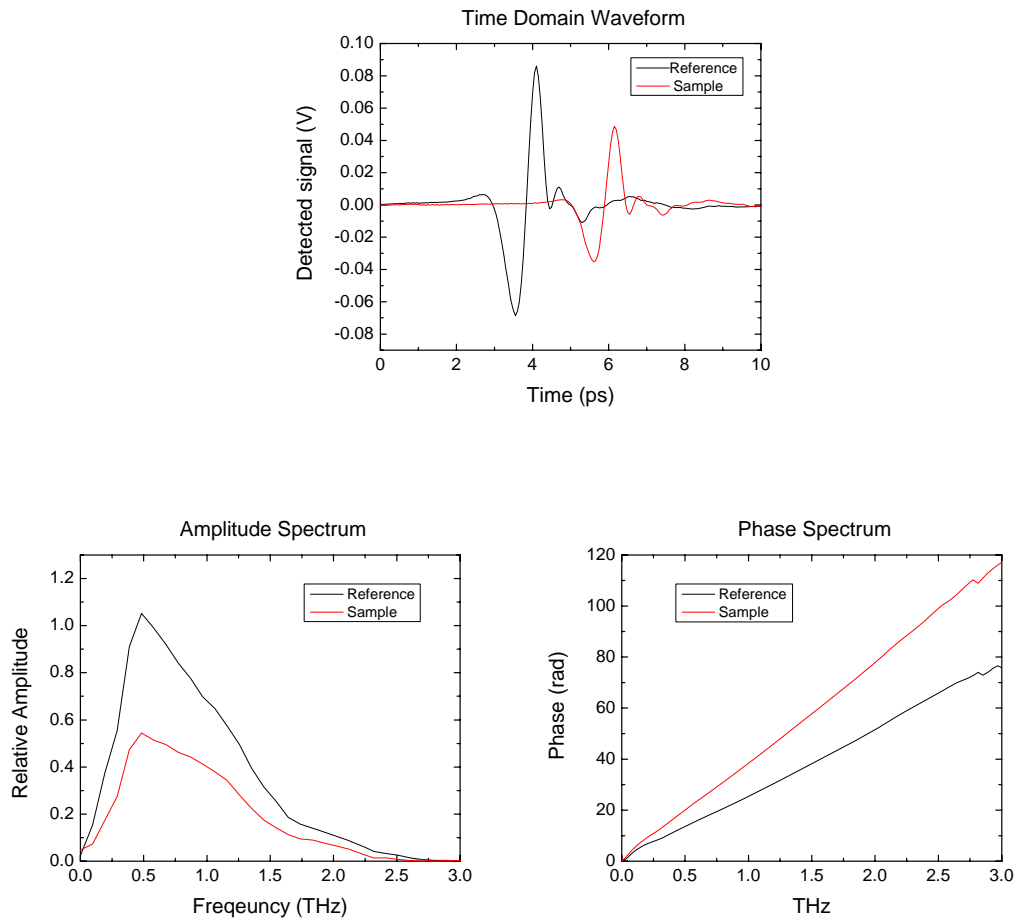
Figure 2-15 (Top) THz pulse transmitted through the p-type silicon and the reference THz pulse with no sample present. (Bottom left) amplitude spectrum and (bottom right) phase spectrum of these two pulses.

Using the transmission equation (2.33) and the frequency dependent data of amplitude and phase, the frequency dependent complex index of refraction of the sample can be obtained, as shown in Figure 2-16. The dielectric constant can be obtained by squaring the index of refraction, and then the complex conductivity can be calculated by equation (2.36). The undoped dielectric constant of silicon is $(3.415)^2$ [30]. Figure 2-17 shows the real and imaginary conductivity of the p-type silicon.
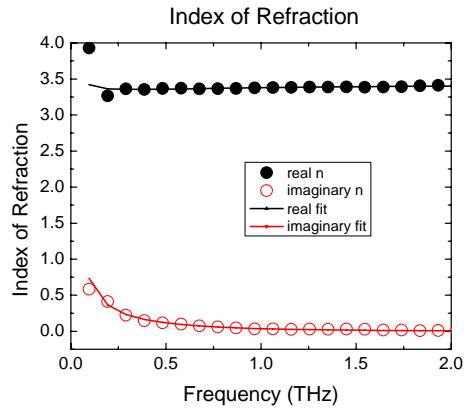
Figure 2-16 Complex index of refraction of the p-type silicon
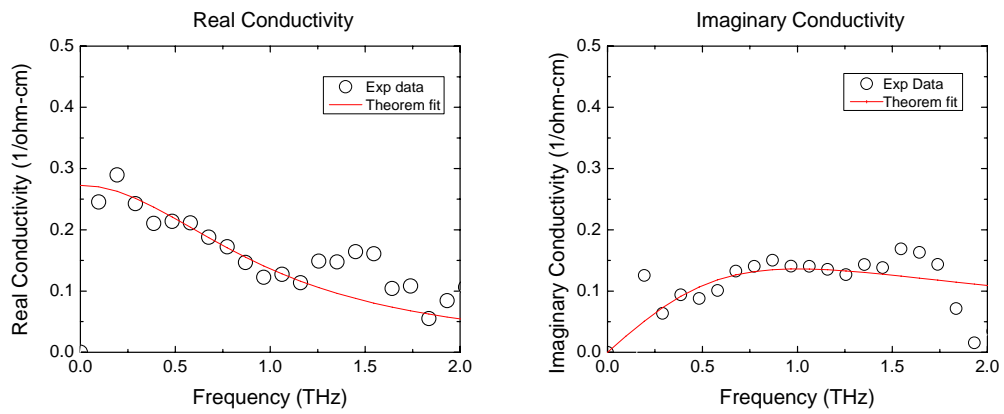
Figure 2-17 Real part (left) and imaginary part (right) of conductivity of the p-type silicon.

Data Comparison

Properties	Measured by THz-TDS	Data from Manufacturer
DC Conductivity (1/ohm-cm)	0.27	0.2~1
Carrier Density (1/cm^3)	2.5×10^{15}	$2.7 \times 10^{15} \sim 1.4 \times 10^{16}$
Plasma Frequency ($\omega_p / 2\pi$,THz)	0.7	
Scattering Rate ($\gamma / 2\pi$,THz)	1	

Table 1 Data comparison of measured data by THz-TDS and the data from manufacturer.

The conductivity can be fitted with the Drude model as shown in equation (2.40). For this P-type silicon we found the plasma frequency ($\omega_p / 2\pi$) is 0.7 THz and the scattering frequency ($\gamma / 2\pi$) is 1 THz. A combination of the measured plasma frequency, scattering rate, and the effective carrier mass, which is 0.37 free electron mass for the average of light and heavy holes [30], yields a carrier density of 2.5×10^{15} cm^{-3} and carrier mobility of 600 cm^2 V^{-1} s^{-1}. These numbers are in good agreement with the data from the manufacture data sheet of the p-type silicon.

2.4.2 ITO measurement

Non-contact measurements of conductivity of thin films have received considerable interest, because a non-contact method eliminates the effects associated with the presence of contacts and simplifies sample fabrication. Terahertz time-domain spectroscopy is a powerful non-contact technique to measure optical and electrical properties of materials in the terahertz region. In this measurement, we use THz-TDS to measure electronic properties of transparent electrode indium tin oxide (ITO) film and compare them with the results from ellipsometry measurement.

The ITO film was obtained from DELTA Technologies™ and had a thickness of 190 nm. The film covered a half of the quartz substrate and the film on another half substrate was removed for comparison measurement. The THz waveform was recorded after the THz passed through the substrate and the ITO film, and then was compared with the reference THz waveform gathered from THz that passed through the quartz substrate only. Figure 2-18(left) shows the complex index of refraction of the ITO versus frequency. Figure 2-18(right) shows the conductivity of ITO versus frequency. The result shows that the ITO has conductivity of 8200/ohm-cm, which agrees with the data from manufacturer, 7800~15000/ohm-cm. Both curves can be fitted well using the Drude model.

Using the Drude parameters obtained from the THz-TDS at THz frequency, we can calculate the n&k value in IR region. Considering the fact that we use the data measured around 1 THz to calculate the complex index of reflection in the IR range

(~200 THz), the calculated IR data generally agrees with n&k measurement using ellipsometry, as shown in Figure 2-19.
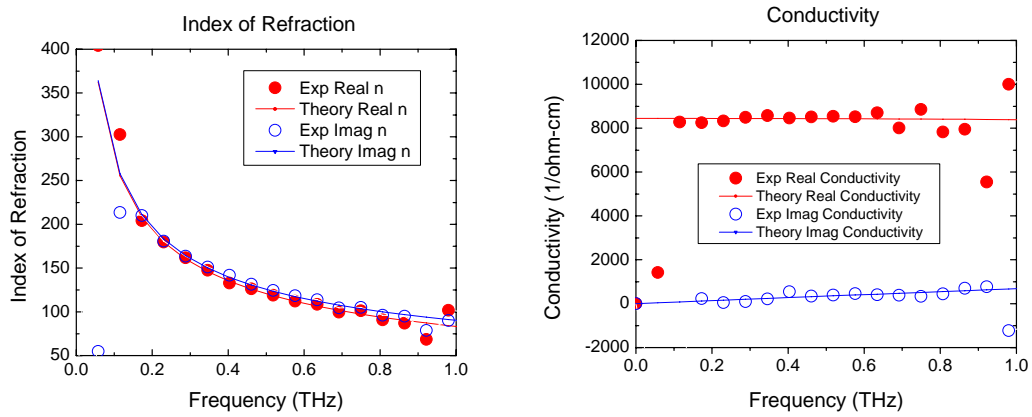
Figure 2-18 (Left) Complex index of refraction of the ITO. (Right) Complex conductivity of the ITO.
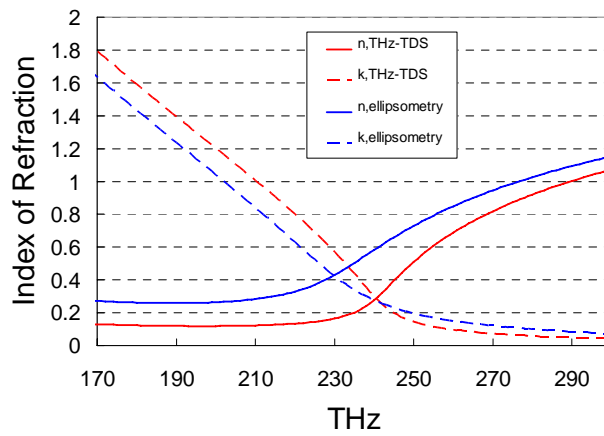
Figure 2-19 Index of refraction of the ITO in IR region. The red curves are calculated using the Drude model from THz-TDS measurement, and the blue curves are from ellipsometry measurement.

Chapter 3: Optical Pump- THz Probe Time Domain Spectroscopy

3.1 Introduction

Optical pump- THz probe time domain spectroscopy (OPTP-TDS) is a technique which combines pump-probe measurement and THz-TDS spectroscopy. In an OPTP-TDS measurement, an ultrafast optical pulse pumps a sample to generate excited carriers. Following the pump pulse, the photoinduced carriers are probed with a broadband pulse of THz radiation. Like other pump-probe measurements, the relative delay time of optical pump pulses and THz probe pulses can be adjusted by varying the flying distance of both pulses. The dynamics of photoexcited carriers thus can be followed in real-time.

The analysis of OPTP-TDS becomes complicated when the event we observe is faster than the THz pulse widths, which have duration around 1 ps. Kindt and Schmuttenmaer [46] suggest that we can measure the THz waveform change by scanning the delay line of the THz transmitter with delays of THz receiver and pump delay fixed. The THz waveform change one obtains directly from the measurement would give directly the transient conductivity. This measurement method is widely used in OPTP-TDS measurements. Recently, Nienhuys and Sundstrom's theoretical analysis of the optical-pump terahertz-probe measurement showed that the conductivity we obtained using this method actually contains two time-dependent kinetics: one is the response of the charge carrier to an electrical field, and another is the time dependent carrier density dynamic. The conductivity does not have a straightforward physical meaning when the carrier population varies abruptly during the time of THz probing (e.g., in the beginning

of the photoexcitation). Also, the fast dynamics we measured in the transient THz peak absorption experiment may not necessarily reflect the true sample dynamics for the same reason. In order to obtain the correct value of conductivity, a series of Fourier and time shifted transformations were suggested in these scenarios.

In this chapter, we focus on two parts: The first part gives the theoretical derivation of the analysis method. The artificial conductivity we obtain directly from the optical pump-THz probe time domain spectroscopy using the conventional analysis method suggested by Kindt and Schmuttenmaer will be derived. A new analysis method regarding a series of transformations suggested by Nienhuys and Sundstrom to obtain true conductivity is also discussed in this part. The second part presents an experiment for transient photoconductivity measurement of photoexcited GaAs. GaAs is a well known Drude like material, and we use it as a benchmark sample to test the new analysis method. A comparison of the results using the new analysis method and the results obtained from the conventional method will be made.

3.2 Experiment method
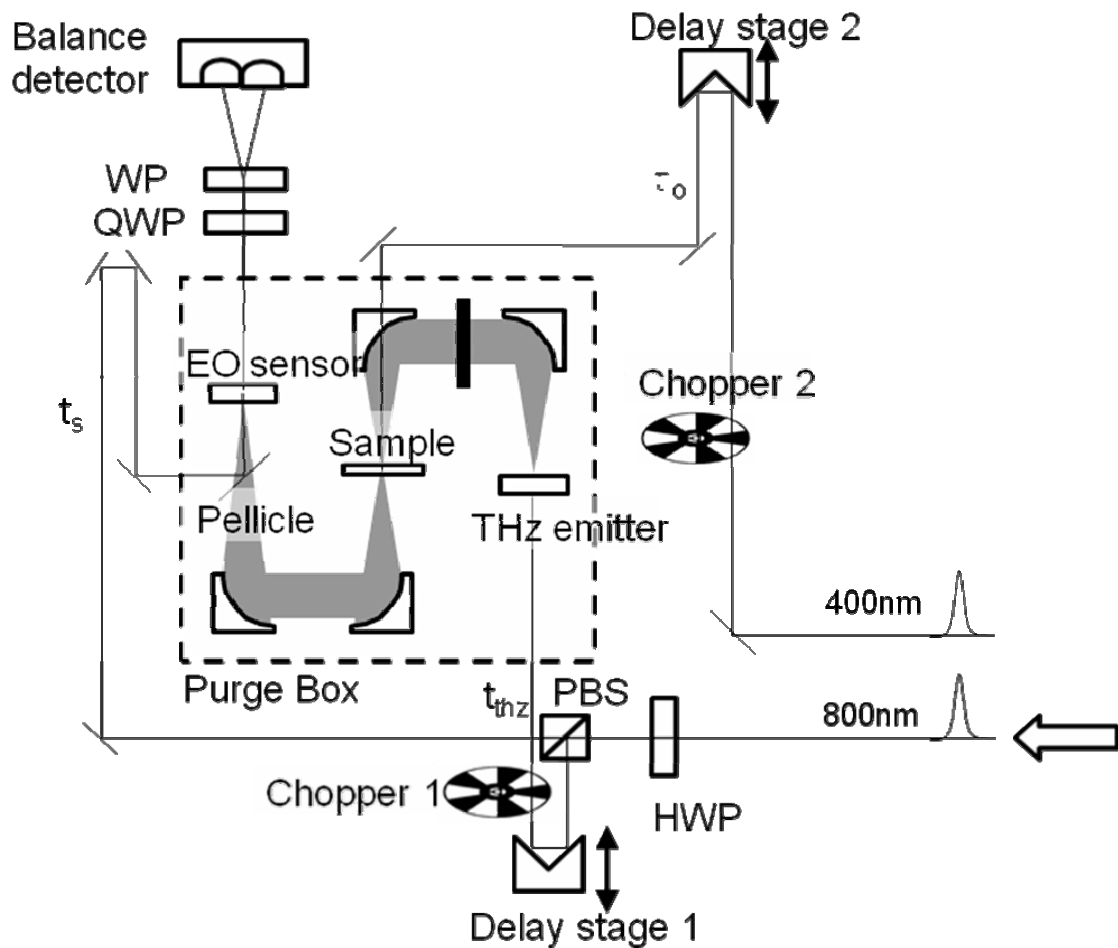
Figure 3-1 Schematic drawing of the experimental setup for OPTP-TDS

The optical pump-THz probe time domain spectroscopy (OPTP-TDS) is a technique for measuring the time-resolved complex dielectric constant, absorption coefficient, and conductivity of a photo-excited sample in the THz frequency range. The experimental setup for OPTP-TDS is basically the same as the experimental setup for

THz time domain spectroscopy, as described in chapter 2, plus an optical delay arm for photoexcitation, as shown in Figure 3-1. The pumping wavelength, depending on the material properties of the sample, could be 800 nm pulse from the oscillator itself, or 400 nm from a frequency doubler. To minimize temporal smearing, the pump pulses pass through the off-axis parabolic mirror and are collinear with the THz probe pulses before pumping the sample. Another important issue for OPTP-TDS experiment is that the pump pulse spot size must be larger than the THz probe spot size at the probing area [41][42]. In any pump-probe experiment, a uniformly excited medium is desired for probing. For THz experiments, the THz pulse is a broadband source ranging in frequency from 0.2 THz to 2 THz, corresponding to wavelengths of 1.5 mm to 0.15 mm. The spot size at focus point can be calculated from the diffraction limit formula [43]:

$$d = \frac{\lambda}{2N.A.} \quad ,$$

(3. 1)

where d is the diameter of the spot, λ is the wavelength of the THz wave, and N.A. is the numerical aperture. The N.A. for our system is 0.25. For the longest wavelength of the THz pulse, the spot size is 3 mm. The beam diameter of the optical pump pulses is 5 mm, which is larger than the diameter of 3 mm for the lowest frequency of the THz probe pulses at the sample thus making a uniform excitation on the probing area.

There are two measuring modes for OPTP-TDS experiments: optical pump scans and THz probe scans. In optical pump scans, the peak of the transmitted THz waveform is monitored while changing the optical path length of the optical pump [44][45]. When the optical pump pulses reach the sample earlier than the THz probe pulses do, the peak

amplitude of the transmitted THz waveform will decrease due to the photoexcitation of the sample. This measuring method provides a rough idea of the time dependent photo-induced conductivity dynamic of the sample in a single scan measurement. However, it may not represent the exact conductivity dynamic, because the phase shift of the transmitted THz waveform for the different pump delay time might not be the same.

The second measuring mode for OPTP-TDS experiments is THz probe scan [41][46][47]. This mode is suggested by Kindt and Schmuttenmaer [46] and involves scanning two different delay lines to obtain the two-dimensional (2D) plot. To clarify the measurement method, first we descrive the 3 delay lines in our OPTP-TDS system: (1) a delay line for optical pump (pump delay); (2) a delay line for THz generation (probe delay); (3) a delay line for THz detection (gating delay). There are 2 ways to do it: the first is to scan the gating delay at different pump delay times, as shown in Figure 3-2 and Figure 3-4 (a); another is to scan the probe delay at different pump delay time, as shown in Figure 3-3 and Figure 3-4 (b). The data obtained from the first method requires a 45 degree transformation, thus each point in the measured waveform has passed through the sample after the same amount of time from the photoexcitation event [46]. The transformed data from the first method is exact the same as the data collected from the second method [46]. However, Nienhuys and Sundstrom [29] have shown that there are significant complications in obtaining the time dependent conductivity from this experimental method when the pump delay time is very short. Additional transformations are necessary for recovering the true time dependent conductivity. This part of the analysis will be discussed in the next section.
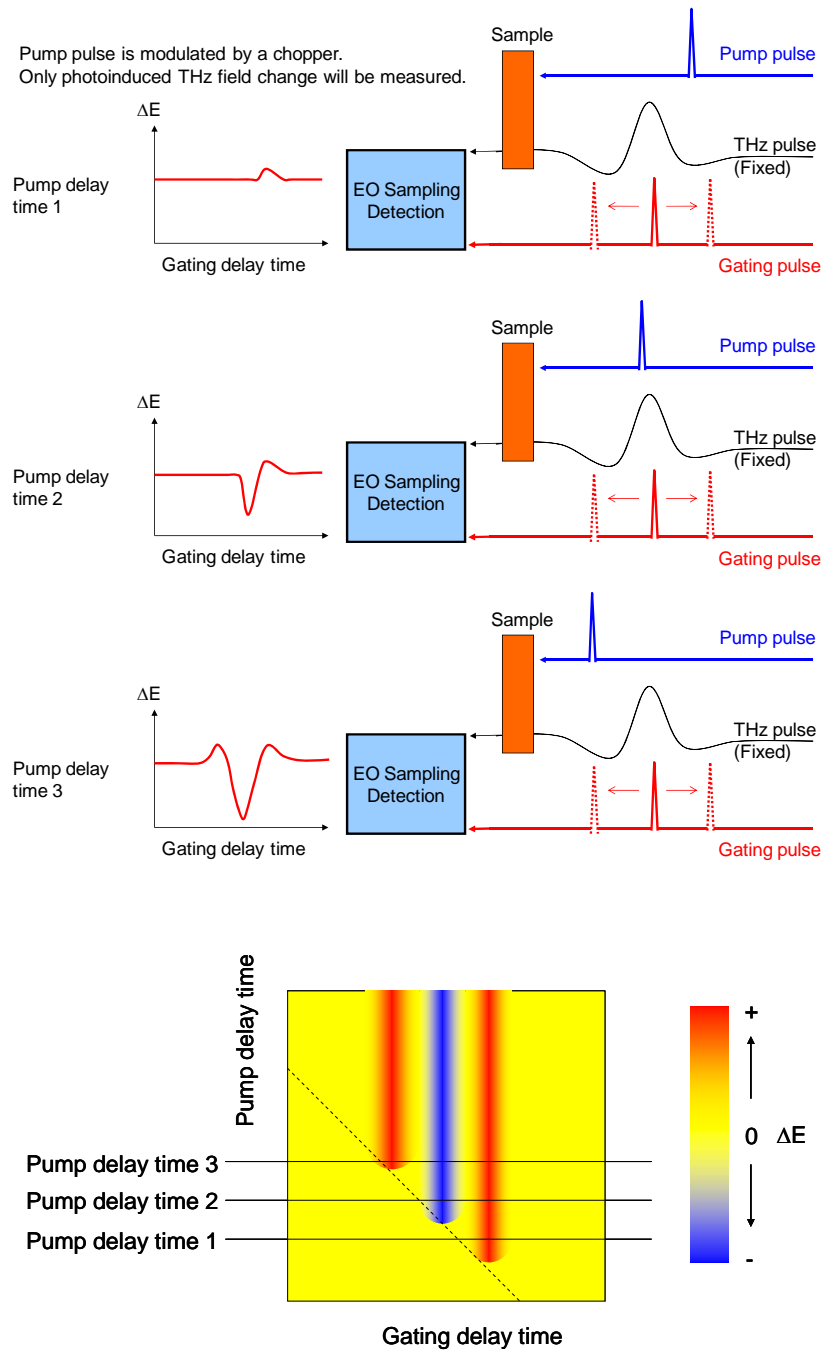
Figure 3-2 OPTP-TDS measurement method 1. The gating delay is scanned at different pump delay time

(time 1, 2, and 3). The results can be presented in a 2D plot, as shown in the bottom plot. The results need

to be transformed so that the 45 degree dash line will be the new x-axis of the plot after transformation. The

transformed result is exactly the same as the 2D plot in Figure 3-3

55
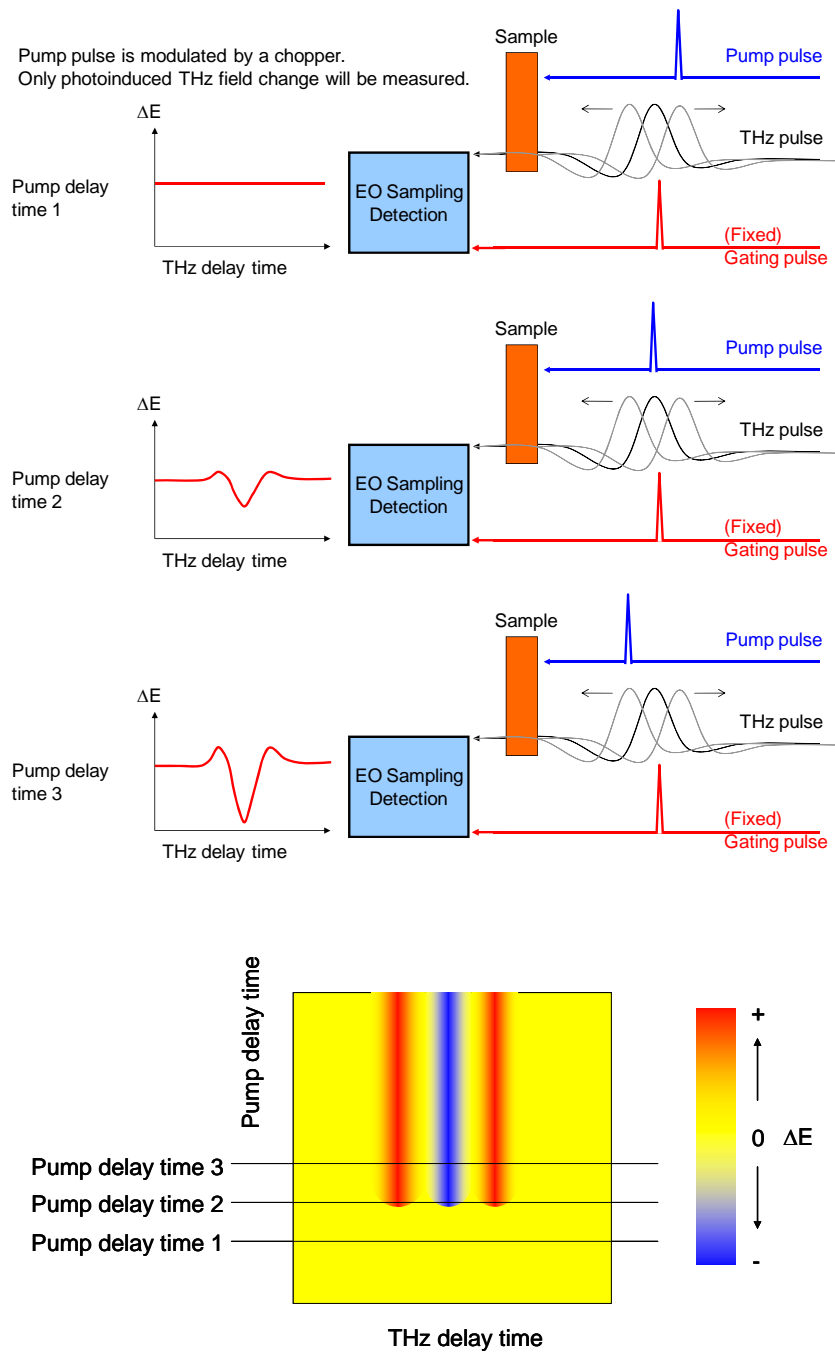
Figure 3-3 OPTP-TDS measurement method 2. The THz (probe) delay is scanned at different pump delay time (time 1, 2, and 3). The results can be presented in 2D plot, as shown in the bottom plot.
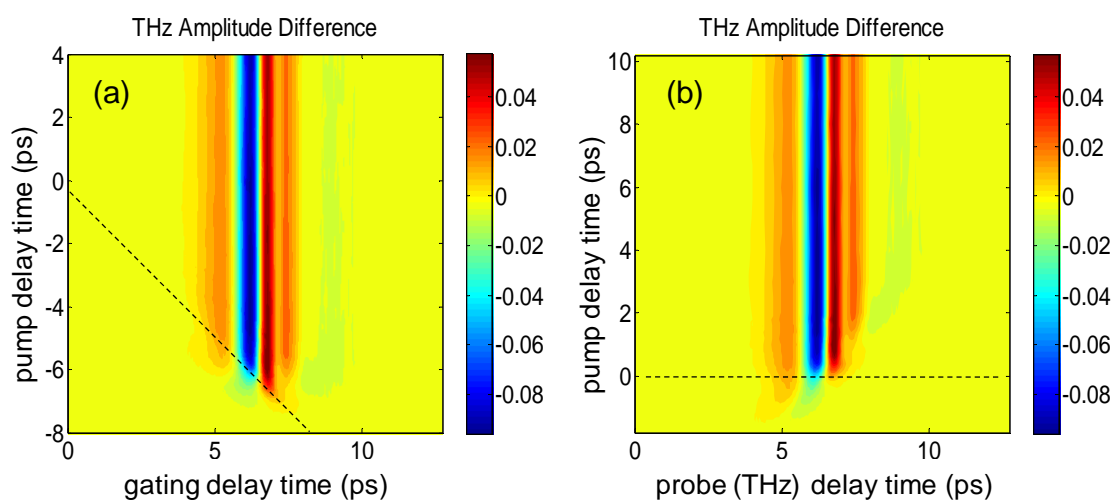
Figure 3-4 Two-dimensional (2D) contour plot of THz amplitude difference for photo-exited GaAs. Plot (a) was obtained by varying the gating delay time (x axis) and pump delay time (y axis). Plot (b) was obtained by varying probe delay time (x axis) and pump delay time (y axis). The dash lines in (a) (45 degree) and in (b) (0 degree) represent the same THz amplitude difference data.

In THz-TDS systems, linear translation stages are usually used for varying the optical path length. They are accurate and have a long range, but they scan slowly. In OPTP-TDS system, linear translation stages can be used when the degradation of the sample is negligible, such as many inorganic semiconductors. However, when a sample suffers considerable degradation during the measurement, such as some semiconducting polymers, the slow scan inherent to the linear translation stages may produce incorrect data because the properties of the sample have been changed during the scan. To overcome this scenario, we use mechanical vibrators to drive the retroreflectors to get a rapid scan (1 Hz). The mechanical vibrator we used is basically a big speaker which can be driven by an external applied electric field. The retroreflectors are mounted on the

vibrators which are driven by a 1 Hz sinusoidal electric wave. The scan result is monitored on an oscilloscope, which can average the result of multiple scans. Because the movement of the vibrators is not linear, a displacement (or time) calibration is necessary. By comparing the measurement result from the vibrators and linear translation stages, the calibration curve between the data measured by the vibrators and the linear stages can be obtained, as shown in Figure 3-5.
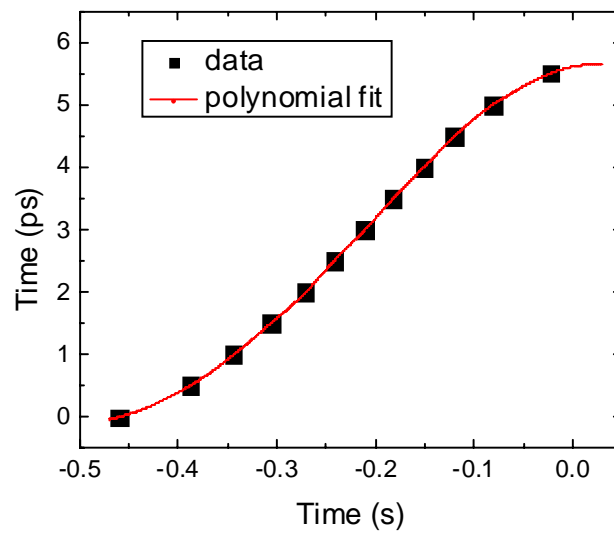
Figure 3-5 Calibration plot for converting the time readout from the oscilloscope to real time.

3.3 Analysis method

3.3.1 Multilayer transmission

In OPTP-TDS experiment, the samples are photo-excited by optical pump pulses and photo-induced carriers are generated. Unlike the carriers in the homogeneous samples for steady state THz-TDS measurements, the photo-induced carriers are not uniformly distributed in the sample when the sample thickness is larger than the penetration depth of the optical pump. When the absorption is linear (i.e. no two photon absorption or other higher orders involved), the photo-induced carrier density decays exponentially, as shown in Figure 3-6. To calculate the THz transmission of the sample, the photo-excited sample can be treated as an N-layer system and each layer has a homogeneous carrier distribution.
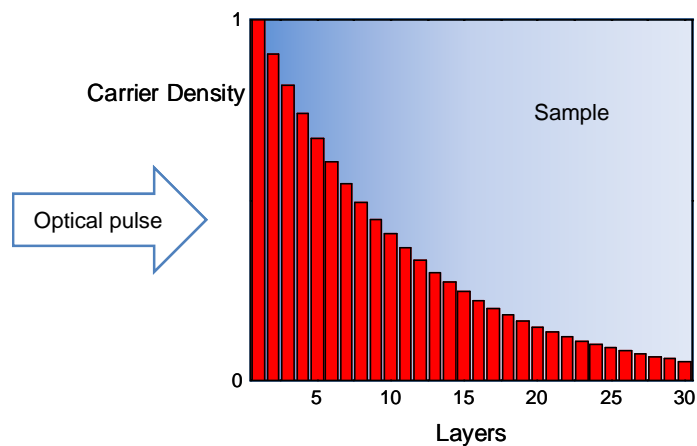
Figure 3-6 The decay of the carrier density in the photo-excited sample. The carrier density can be approximated by a series of homogeneous layers.

The relationship between transmission and index of refraction of the excited

region can be obtained using a multilayer transmission formula [40]:

$$t = \frac{2\gamma_0}{\gamma_0 m_{11} + \gamma_0 \gamma_s m_{12} + m_{21} + \gamma_s m_{22}} \quad , \tag{3.2}$$

where

$$\begin{bmatrix} m_{11} & m_{12} \\ m_{21} & m_{22} \end{bmatrix} = M_1 \cdot M_2 \cdot M_3 \cdots M_n \quad ,$$

$$M_i = \begin{bmatrix} \cos(k \cdot n_i \cdot d_i) & \dfrac{i \sin(k \cdot n_i \cdot d_i)}{\sqrt{\dfrac{\varepsilon_0}{\mu_0}} \cdot n_i} \\ \sqrt{\dfrac{\varepsilon_0}{\mu_0}} \cdot n_i \cdot i \sin(k \cdot n_i \cdot d_i) & \cos(k \cdot n_i \cdot d_i) \end{bmatrix} \quad ,$$

$$\gamma_0 = \sqrt{\frac{\varepsilon_0}{\mu_0}} \cdot n_0, \gamma_s = \sqrt{\frac{\varepsilon_0}{\mu_0}} \cdot n_s \quad , \tag{3.3}$$

where k is the angular wavenumber of the probing electromagnetic wave, n_i and d_i are the

index of refraction and thickness of the layer i, n_0 is the index of refraction of the medium

of incident wave, and n_s is index of refraction of the medium of transmission wave. The

transmission coefficient t can be measured directly by measurement. Following the same

analysis procedures for single layer medium, we can calculate the complex index of

refraction numerically, and then compute the corresponding conductivity.

3.3.2 Thin film approximation

The sample in OPTP-TDS experiment can be treated as a very thin sample when the skin depth of the sample for optical pump wavelength is much smaller than then THz probe wavelength (~ 300 micron). For a very thin sample, one can derive that the current induced on the sample is equal to the electric field difference between the reference electric field (which is the field that passes through the un-excited sample) minus the electric field that passes through the excited sample [29], as shown below:

First consider Maxwell equations:

$$
\begin{cases}
\nabla \cdot D = \rho_f \\
\nabla \cdot B = 0 \\
\nabla \times E = -\dfrac{\partial B}{\partial t} \\
\nabla \times H = J_f + \dfrac{\partial D}{\partial t}
\end{cases}
$$

(3. 4)

Using the curl of the curl identity, we get

$$
\because \nabla \times (\nabla \times E) = \nabla (\nabla \cdot E) - \nabla^2 E \quad,
$$

$$
= \nabla \frac{\rho}{\varepsilon} - \nabla^2 E = \nabla \times \left(-\frac{\partial B}{\partial t} \right) = -\frac{\partial}{\partial t}(\nabla \times B) = -\mu \frac{\partial}{\partial t} J - \mu\varepsilon \frac{\partial^2}{\partial t^2} E \quad,
$$

$$
\therefore \nabla^2 E - \mu\varepsilon \frac{\partial^2}{\partial t^2} E = \nabla \frac{\rho}{\varepsilon} + \mu \frac{\partial}{\partial t} J \quad.
$$

(3. 5)

Assuming $\nabla \rho = 0$ (net charge = 0 in the medium)

$$\Rightarrow \nabla^2 E - \frac{n^2}{c^2}\frac{\partial^2}{\partial t^2}E = \frac{1}{\varepsilon_0 c^2}\frac{\partial}{\partial t}J \quad .$$

(3. 6)

Let $J(z,t) = J(t)\cdot L\cdot\delta(z)$ by the limit of $L\to 0$, therefore

$$\frac{\partial^2}{\partial z^2}E(z,t) - \frac{n^2}{c^2}\frac{\partial^2}{\partial t^2}E(z,t) = \frac{L\cdot\delta(z)}{\varepsilon_0 c^2}\frac{\partial}{\partial t}J(t)$$

$$\Rightarrow \int_{0-}^{0+}\left(\frac{\partial^2}{\partial z^2}E(z,t) - \frac{n^2}{c^2}\frac{\partial^2}{\partial t^2}E(z,t)\right)dz = \int_{0-}^{0+}\left(\frac{L\cdot\delta(z)}{\varepsilon_0 c^2}\frac{\partial}{\partial t}J(t)\right)dz$$

$$\Rightarrow \frac{\partial}{\partial z}E(z,t)\Big|_{0-}^{0+} - \frac{n^2}{c^2}\frac{\partial^2}{\partial t^2}\int_{0-}^{0+}E(z,t)dz = \frac{L}{\varepsilon_0 c^2}\frac{\partial}{\partial t}J(t)$$

$$\Rightarrow \frac{\partial}{\partial z}E(z,t)\Big|_{0-}^{0+} = \frac{L}{\varepsilon_0 c^2}\frac{\partial}{\partial t}J(t) \quad .$$

(3. 7)

Assuming the THz absorption is very small and can be neglected, the THZ pulses can be described as wave packets, as shown in Figure 3-7:

$$E(z,t) = \begin{cases} A_{in}(t - zn_A/c) + A_r(t + zn_A/c) & (z<0) \\ A_{tr}(t - zn_B/c) & (z>0) \end{cases} \quad .$$

(3. 8)

J(t)

A_in

A_tr

A_r

L

O

z
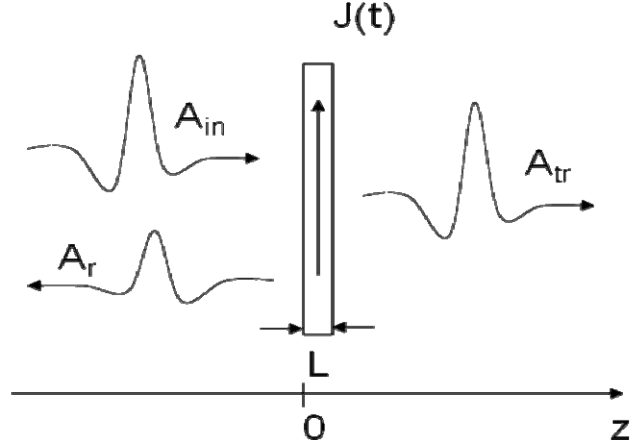
Figure 3-7 The current J(t) is generated in a thin sample with thickness L. A_{in}, A_{tr}, and A_r represents the incident THz pulse, transmitted THz pulse, and reflected THz pulse.

Substitute (3. 8) into (3. 7), we get

$$\Rightarrow \frac{L}{\varepsilon_0 c^2}\frac{\partial}{\partial t}J(t) = \frac{\partial}{\partial z}E(z,t)\Big|_{z=0+} - \frac{\partial}{\partial z}E(z,t)\Big|_{z=0-}$$

$$= \frac{\partial}{\partial z}A_{tr}(t - zn_B/c)\Big|_{z=0+} - \frac{\partial}{\partial z}\big(A_{in}(t - zn_A/c) + A_r(t + zn_A/c)\big)\Big|_{z=0-}$$

$$= \frac{\partial A_{tr}(t - zn_B/c)}{\partial(t - zn_B/c)}(\frac{-n_B}{c})\Big|_{z=0+} - \left(\frac{\partial A_{in}(t - zn_A/c)}{\partial(t - zn_A/c)}(-\frac{n_A}{c}) + \frac{\partial A_r(t + zn_A/c)}{\partial(t + zn_A/c)}(\frac{n_A}{c})\right)\Big|_{z=0-}$$

$$= \frac{-n_B}{c}\frac{\partial A_{tr}(t)}{\partial t} + \frac{n_A}{c}\frac{\partial A_{in}(t)}{\partial t} - \frac{n_A}{c}\frac{\partial A_r(t)}{\partial t} \quad .$$

(3. 9)

At time=0, there is no electric field nor photo-induced current:

$$\because J(0) = A_{in}(0) = A_r(0) = A_{tr}(0) = 0 \quad ,$$

$$\therefore \frac{L}{\varepsilon_0 c}J(t) = -n_B A_{tr}(t) + n_A A_{in}(t) - n_A A_r(t) \quad .$$

(3. 10)

63

The boundary condition requires that E is continuous at z=0, therefore

$$\therefore A_{in}(t) + A_r(t) = A_{tr}(t)$$

$$\Rightarrow \frac{L}{\varepsilon_0 c} J(t) = -n_B A_{tr}(t) + n_A A_{in}(t) - n_A (A_{tr}(t) - A_{in}(t))$$

$$\Rightarrow \frac{L}{\varepsilon_0 c} J(t) = -(n_A + n_B) A_{tr}(t) + 2n_A A_{in}(t)$$

$$\Rightarrow J(t) = \frac{\varepsilon_0 c}{L} [-(n_A + n_B) A_{tr}(t) + 2n_A A_{in}(t)] \quad .$$

(3. 11)

Without optical pump, there is no photo-induced current,

$$\Rightarrow J(t) = 0 = \frac{\varepsilon_0 c}{L} [-(n_A + n_B) A_{tr}^0(t) + 2n_A A_{in}(t)] \quad .$$

(3. 12)

Combine (3. 11) and (3. 12), we obtain

$$J(t) = \frac{\varepsilon_0 c (n_A + n_B)}{L} [A_{tr}^0(t) - A_{tr}(t)] \quad .$$

(3. 13)

64
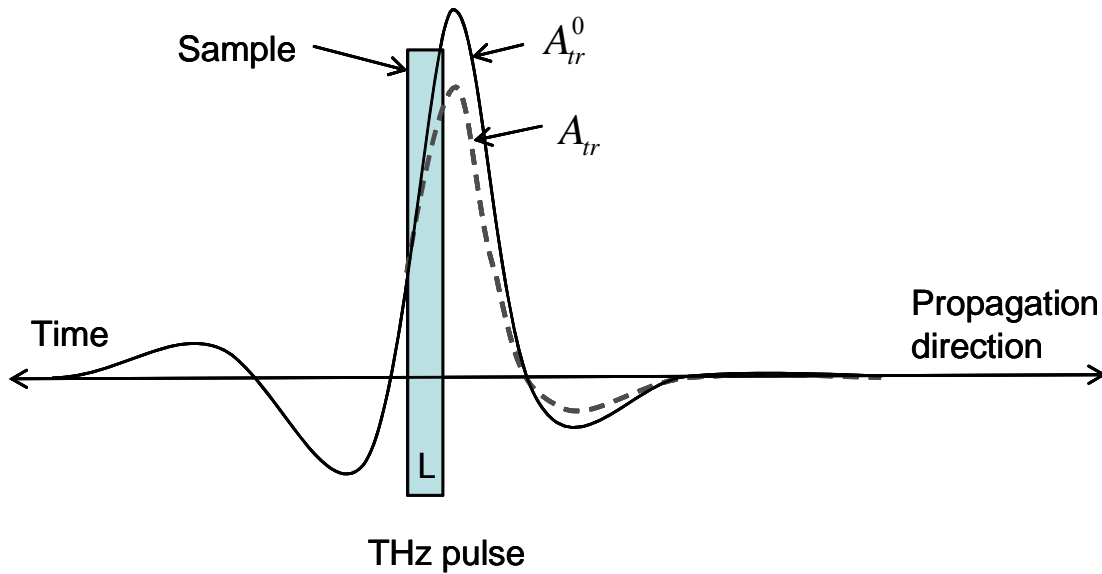
Figure 3-8 The photo-induced current in the sample is proportional to the difference of the electrical field of the reference THz pulses A_{tr}^{0} (without optical pump) and signal THz pulses A_{tr} (with optical pump).

3.3.3 Data correction in the beginning of excitation

THz pulses are single cycle electric pulses with duration around 1 ps. In OPTP-TDS measurement, when the THz pulses are probing an event which is much slower than the duration of the THz pulses, it can be treated as a steady state problem and the physical properties of the sample can be analyzed as we described in the previous chapter. However, when the THz pulses are probing an event which is comparable or even faster than the duration of the THz pulses, like the properties at the time when the material is just photo-excited, it becomes a non-trivial problem and needs to be considered carefully. In order to measure the photoconductivity in the situation when the material is just photo-excited, or shortly thereafter, Kindt and Schmuttenmaer introduced a measurement method that let each point in the measured waveform that has passed through the sample

65

after the same amount of time from the photo-excitation event [46]. It can be done by either applying 45 degree transformation analysis to the data obtained from fixing the optical pump delay line and the THz probe delay line and scanning the gating delay line, or keeping the optical pump delay line and gating delay line fixed and scanning the THz probe delay line [41][46][47]. This method has been followed by many OPTP-TDS measurements [48][49][50]. Recently, Nienhuys and Sundstrom showed that there are significant complications in obtaining time resolved conductivity from this experiment method for the time when the sample is just excited or shortly thereafter [29]. They also suggested a series of transformations for data analysis to obtain the true conductivity. This shall be explained below.

First let us consider the single charge impulse response. For a monochromatic wave $E(t) = E_0 e^{-i\omega t}$, the relation between complex conductivity $\sigma(\omega)$, $E(t)$, and electric current density J(t) is

$$J(t) = \text{Re}[\sigma(\omega)E_0 e^{-i\omega t}] \quad .$$

(3. 14)

Thus, The frequency-domain conductivity can be defined as

$$\sigma(\omega) = \frac{F[J(t)](\omega)}{F[E(t)](\omega)} \quad .$$

(3. 15)

Because the THz time domain spectroscopy collects data in the time domain, we should also derive every formula in the time domain. The single charge impulse response is the

66

current density that would result from applying a delta-pulsed electric field to a single charge. Using (3. 15), the conductivity for single charge impulse response is

$$\sigma(\omega) = \frac{F[j_0(t)](\omega)}{F[\delta(t)](\omega)} = \frac{F[j_0(t)](\omega)}{1} \quad .$$

(3. 16)

Therefore, the current induced by the input impulse field (delta function) is

$$j_0(t) = F^{-1}[\sigma(\omega)](t) \quad .$$

(3. 17)

For example, if we consider a material whose electrical conductivity follows the Drude model, the single charge input response can be calculated by applying inverse Fourier transformation of Drude model for conductivity in frequency space:

$$
\begin{aligned}
\sigma(t) &= \frac{1}{\sqrt{2\pi}} \int_{-\infty}^{\infty} \frac{\sigma_{01}}{1 - i\omega\tau_D} \exp(i\omega t) d\omega \\
&= \sqrt{2\pi} \frac{e\mu}{\tau_D} \exp(-\frac{t}{\tau_D}) U(t) \\
&= \sqrt{2\pi} \frac{e^2}{m^*} \exp(-\frac{t}{\tau_D}) U(t) \quad ,
\end{aligned}
$$

(3. 18)

where U(t) is the unit step function. The response is an exponential decay function, as shown in Figure 3-9.
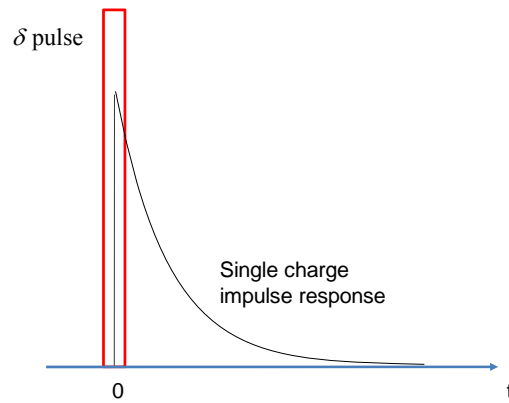
Figure 3-9 Single charge impulse response in Drude like conductor.
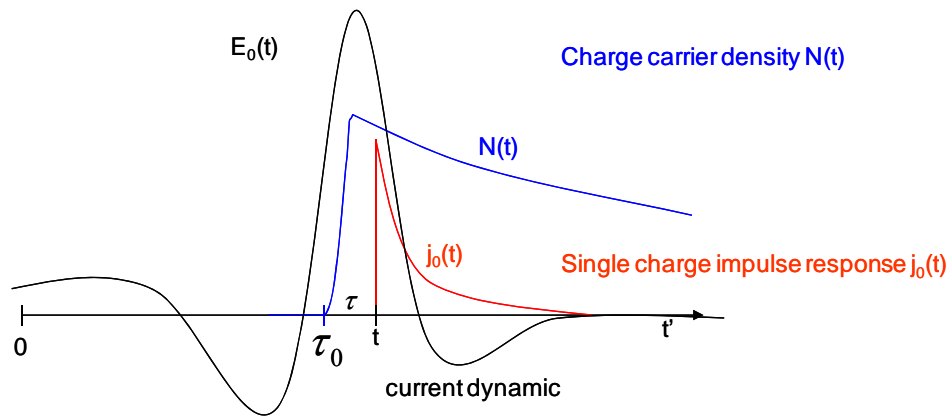
Figure 3-10 The single charge impulse response $j_0(t)$, charge carrier density $N(t)$, and the THz electrical field $E_0(t)$.

Consider a picture that relative to the input THz probe wave, the optical pump pulse arrives at time τ_0 and the sampling pulse arrives at time t, as shown in Figure 3-10. The current dynamic related with the time dependent charge carrier density function and the single charge impulse response is a convolution:

$$J(t, \tau_0) = [E_0(t)N(t - \tau_0)] \otimes j_0(t)$$

$$= \int_{-\infty}^{\infty} E_0(t')N(t' - \tau_0)j_0(t - t')dt' \quad .$$

(3. 19)

In the experimental method proposed by Kindt and Schmuttenmaer, which fixes the optical pump delay line and gating delay line while scanning the THz probe delay line, the time difference between the optic pump arrives τ_0 and the sampling time (gating time) t is fixed with a certain time τ. In other words, τ_0 is a function of the time t and τ. Therefore, we make the transformation:

$$\tau \equiv t - \tau_0$$

$$J(t, \tau_0) = J(t, t - \tau)$$

$$= \int_{-\infty}^{\infty} E_0(t')N(t' - (t - \tau))j_0(t - t')dt'$$

$$= \int_{-\infty}^{\infty} E_0(t')N(\tau - (t - t'))j_0(t - t')dt'$$

$$= E_0(t) \otimes [N(\tau - t)j_0(t)]$$

$$\equiv J_T(t, \tau) \quad .$$

(3. 20)

The current J_T is related to the THz wave difference measurement in our experiment, as shown in (3. 13). The conductivity in frequency space can be calculated by

$$\sigma_T(\omega, \tau) = \frac{F[J_T(t, \tau)](\omega)}{F[E_0(t)](\omega)}$$

$$= \frac{F\{E_0(t) \otimes [N(\tau - t)j_0(t)]\}(\omega)}{F[E_0(t)](\omega)}$$

$$= \frac{F[E_0(t)](\omega) \cdot F[N(\tau - t)j_0(t)](\omega)}{F[E_0(t)](\omega)}$$

$$= F[N(\tau - t)j_0(t)](\omega) \quad .$$

(3. 21)

69

which is different from the result of the steady state case: $\sigma(\omega) = N \cdot F[j_0(t)](\omega)$ and does not have a straightforward physical meaning because carrier density function couples into the conductivity in the frequency domain.

In order to retrieve the true conductivity, a series of transformations are suggested [29]. First transfer (3. 21) back to the time domain:

$$
\begin{aligned}
\sigma_T(t,\tau) &= F^{-1}[\sigma_T(\omega,\tau)](t) \\
&= F^{-1}[F[N(\tau-t)j_0(t)](\omega)](t) \\
&= N(\tau-t)j_0(t) \quad .
\end{aligned}
$$
(3. 22)

Define a new conductivity that

$$
\begin{aligned}
\sigma(t,\tau) &\equiv \sigma_T(t,\tau+t) \\
&= N(\tau)j_0(t) \quad .
\end{aligned}
$$
(3. 23)

Take the Fourier transform to transfer back to the frequency domain:

$$
\begin{aligned}
\sigma(\omega,\tau) &\equiv F[\sigma(t,\tau)](\omega) \\
&= N(\tau)F[j_0(t)](\omega) \quad .
\end{aligned}
$$
(3. 24)

Notice that the new conductivity is not coupled with a time varying carrier density function anymore. We successfully decouple the dynamic of carrier density from the transient conductivity, and the new conductivity now represents the true conductivity. In

order to perform the transformation in (3. 23), we note that a two dimensional scan is necessary to obtain sufficient information.

3.3.4 Detector response correction

In chapter 2 we have discussed that the measured THz waveform is actually the result of a convolution of true THz waveform and the detector response function, due to the dispersion effect in the E-O detecting crystal. We have proven that the distortion caused by the detector can easily be canceled out when we only consider the ratio of the transmitted THz wave and the reference THz wave in the steady state THz-TDS measurement. In non-steady state OPTP-TDS measurements, due to the complications of THz duration and carrier dynamics, several transformations are required in order to obtain the true physics, as we discussed in the previous section. Prior to performing that data analysis, obtaining the undistorted transmitted THz wave from the measurement is essential for accurate measurement.

To acquire the undistorted transmitted THz wave in a OPTP-TDS measurement, first we need to know the detector response function. The detector response function can be calculated if we know the index of refraction of the detecting crystal at both THz and optical frequencies, as we discussed in chapter 2. Second, we need to know the distorted THz waveform. It can be measured directly by fixing the optical pump delay line, the THz probe delay line, and scanning the gating delay line. Another way to do it is applying the 45 degree transformation to the data obtained by fixing the optical pump delay line and the gating delay line, while scanning the THz probe delay line. Each

71

undistorted transmitted THz waveform is then deconvolved from the detector [41]. Finally, the deconvolved data are numerically transformed back to the constant pump-gating times so that every portion of measured THz transient experiences the same delay from the optical pump. Once the data have been correctly deconvolved and numerically projected, the correction transformation we discussed in the previous section can be applied to retrieve the true time-resolved conductivity.

3.4 Measurement

3.4.1 Photoexcited silicon

In this experiment, we measure electric properties of the photoexcited silicon by OPTP-TDS at a time 10 ps after photoexcitation. Although it is a photoexcitation experiment, the measurement and analysis are similar to the steady-state measurement we discussed in chapter 2. The reason is that the photo-induced charge carrier density at the time around 10 ps is almost a constant, just like steady state, for the duration of the THz probe pulse. The experimental setup is described in section 3.2. The silicon sample is photoexcited by 400nm pulses, and each pulse has energy 4 μJ. The silicon sample is a p-type, 4 ohm-cm silicon wafer. The wafer is double side polished, and has a thickness of 276 micron and [111] orientation. Figure 3-11 shows the THz peak amplitude changes resulting from varying the 400nm pump pulse delay. It shows that silicon has a short rise time of about 3 ps but a very long decay time.
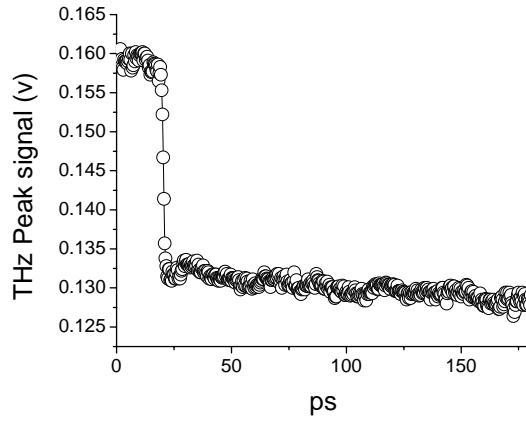
Figure 3-11 THz peak amplitude change versus 400nm pump pulse delay time

Two THz measurements were made for the analysis. THz probe signals were collected at 10 ps increment delays after exposing the sample to the 400nm optical pulse, and a reference THz signal was taken before the 400nm pump pulse arrived the sample. The absorption coefficient of silicon at 400nm is 50000 cm^{-1} [51], so most of the photoexcited carriers will be generated within the skin depth which is less than 1 micron. We assume that the photoexcited carrier density decreases exponentially, so one hundred 10nm thick homogeneous layers were used to model the graded index change. The relationship between transmission and index of refraction of the excited region can be obtained using a multilayer transmission formula (3. 2). Figure 3-12 (left) shows the obtained complex index of refraction versus frequency. The Drude model describes the frequency dependence of the complex dielectric constant ε (equal to the square of the complex index of refraction) and the complex conductivity σ according to the relations

$$\varepsilon = \varepsilon_{w/o} + i\sigma/(\omega\varepsilon_0) \quad , \tag{3.25}$$

73

$$\sigma = i\varepsilon_0 \omega_p^2 /(\omega + i\upsilon) \quad ,$$

(3. 26)

where $\varepsilon_{w/o} = (3.415)^2$ [30], ω_p is the plasma frequency and $\upsilon = 1/\gamma$ is the scattering rate. Using the complex index of refraction, the complex conductivity can be obtained, as shown in Figure 3-12 (right). The experimental data can be fit reasonably well by the Drude model, as shown in Figure 3-12. The values of plasma frequency $\omega_p / 2\pi$ = 32 THz and scattering rate $\upsilon / 2\pi$ =4 THz were then obtained from the complex conductivity fitting. For photoexcitation, we assume that the number of generated electrons and holes are the same. We use the effective carrier mass 0.315 m_e obtained by averaging effective the electron mass and effective hole mass of silicon, where m_e is the free electron mass [30]. With this assumption, the photoexcited carrier density of 4×10^{18} cm^{-3} and the carrier mobility of 200 cm^2 V^{-1} S^{-1} were calculated. The measured carrier mobility of 200 cm^2 V^{-1} S^{-1} is much lower than the mobility of 500 cm^2 V^{-1} S^{-1} of the p-type silicon before photoexcitation. The measured photoexcited carrier density roughly agrees with the average absorbed photon density of 8×10^{18} cm^{-3} obtained by dividing the 400nm pulse fluence by the skin depth.
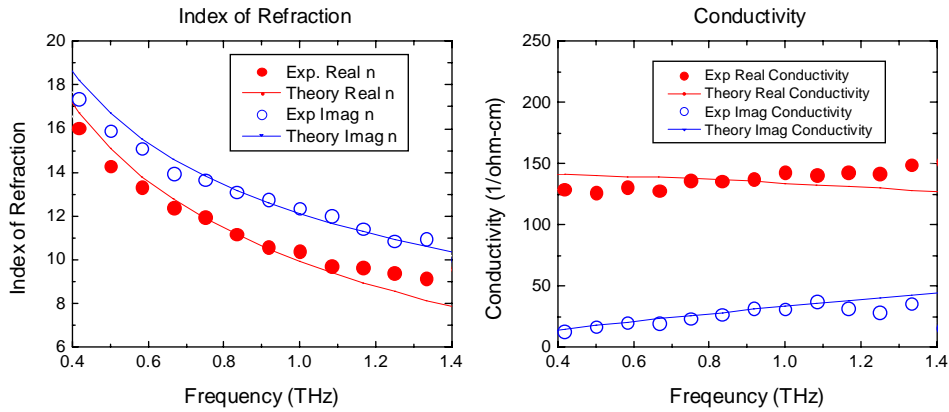
Figure 3-12 (Left) Complex index of refraction of photoexcited p-type silicon. (Right) Complex conductivity of photoexcited P-type silicon. The solid lines are fits using a Drude model.

3.4.2 Photoexcited GaAs

In the previous section we discussed the measurement of photo-induced conductivity of photoexcited silicon at 10 ps after excitation. Although it is an OPTP-TDS experiment, the physical properties of photoexcited silicon at 10 ps after photoexcitation do not change much. It is effectively a steady state THz-TDS measurement, so we used the steady state analytic method to analyze the data. Beard et al. [41] measured the transient photoconductivity in GaAs by OPTP-TDS using Kindt and Schmuttenmaer's analysis method, as we discussed in 3.2. Because the physical properties change abruptly during this period, however, it is a non steady state measurement. They observed that the conductivity for higher THz frequencies rises initially and then gradually decreases to the steady state value, while the conductivity for lower frequencies rises continuously until reaching the steady state value [41]. Later, Nienhuys and Sundstrom's theoretical paper pointed out that the transient conductivity

75

data are more complicated than originally thought [29]. They suggest a series of transformations to obtain the true conductivity from coupled data, as we discussed in 3.3.3. In this section, we are going to discuss the photo-induced conductivity measurement of photoexcited GaAs from a time before the photoexcitation to a time 10 ps after the excitation, verifying the Nienhuys and Sundstrom's theoretical prediction, and obtaining the true transient conductivities from the correction transformations.

GaAs is used as a benchmark sample in our OPTP-TDS measurement. This is because GaAs is a sample that the carrier dynamics can be well described by the simple Drude model. The experimental setup is described in section 3.2. The optical pump is 800 nm pulses (1.55 eV), which is just above the energy gap of GaAs (1.43 eV for temperature = 300 k [52]) to eliminate the possibility of higher energy band transition [41]. The pump beam has energy 0.12 μJ/pulse with 5 mm diameter (fluence: 2.46×10^{16} photons/m^2) to keep the photoexcited carrier density low. The sample is double side polished 2" semi-insulating GaAs wafer from AXT. The thickness is 0.35 mm and the surface orientation is [100] to ensure that it doesn't generate THz radiation upon normal incidence photoexcitation [53].

Complete OPTP-TDS measurements require collecting a series of THz difference probe scans by changing the optical pump delay time step by step. The results of measurement are shown in Figure 3-4. The detector response was deconvolved from the measured wave form as we discussed in section 3.3.4 before further data analysis.

First we analyze the photo-conductivity at the time 10 ps after the initial pump (steady state condition) to obtain the key parameters and as benchmark. Figure 3-13 shows the THz difference scan of the photoexcited GaAs at a time 10 ps after the initial

pump as well as the THz reference scan of the unexcited GaAs. Because it has reached

the steady state (we can judge it from the raw difference data in Figure 3-4.), we can

analysis the data in the same way as we do in THz-TDS measurements.
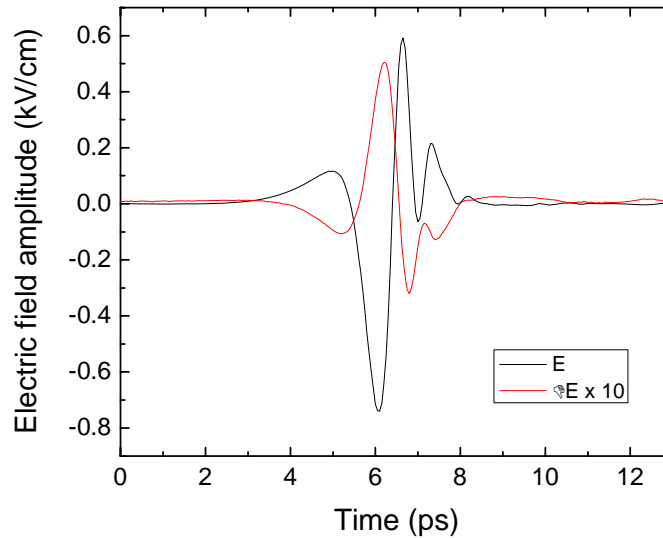
Figure 3-13 Typical THz probe scan obtained from GaAs. Black line is the reference scan of the unexcited

GaAs. Red line is the difference scan of the photoexcited GaAs at the time 10 ps after the initial pump

multiplied by a scaling factor 10.

Figure 3-14 shows the real and imaginary conductivity of the photoexcited GaAs

at the time 10 ps after the initial pump. The lines are the results of fitting using the Drude

model. Here, we use 0.067 m_e as the effective mass of the electron in GaAs [54], the

dielectric constant = $(3.595)^2$ for undoped GaAs [55], and the skin depth=0.66 μm [52].

The Drude model fits the experimental data well, and generates reasonable numbers of

the electron mobility and carrier density, as shown in Table 3-1. The room temperature

electron mobility obtained from the fits is 5750 $cm^2V^{-1}s^{-1}$, which is similar to the value

measured by ref [41]. The carrier density obtained from the fit is 1.9×10^{16} cm^{-3} and is similar to that calculated based on the fluence, the transmittance, and the skin depth ($N = 2.53 \times 10^{16}$ cm^{-3}).
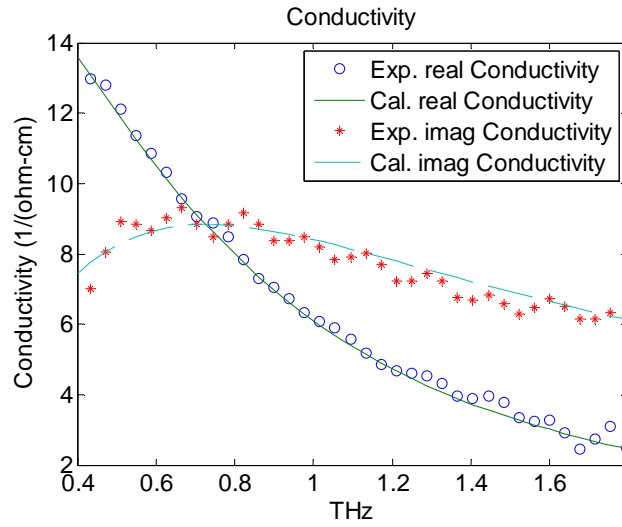
Figure 3-14 Real and imaginary conductivity of the photoexcited GaAs at the time 10 ps after the initial pump. The lines are the results of fitting using the Drude model.

Carrier density	1.9×10^{16} cm^{-3}
Mobility	5750 cm^{2}V^{-1}s^{-1}
Plasma frequency ($\omega_p/2\pi$)	4.8 THz
Scattering rate (γ)	4.5 THz
Scattering time ($\tau = 1/\gamma$)	0.22 ps

Table 3-1 Fitting parameters for Drude model in Figure 3-14

78

Figure 3-15 (a) and (c) shows the two-dimensional (2D) contour plot of the real part and imaginary part of the photo-induced conductivity of photoexcited GaAs from -2 to 10 ps. We also observed the phenomenon that the conductivity for higher frequencies rises initially and then gradually decreases to the steady state value, while the conductivity for lower frequencies rises continuously until reaching the steady state value as in ref [41]. According to Nienhuys and Sundstrom's analysis [29], this is an artificial phenomenon caused by the convolution of the time dependent carrier density function and the single charge current response function, as shown in (3. 21). Using the Drude parameters we measured in Table 3-1 and assuming the time dependent carrier density function is

$$
\begin{cases}
N(t) = 0, t < 0 \quad, \\
N(t) = 1 - \exp(\dfrac{-t}{t_r}), t \ge 0 \quad.
\end{cases}
$$

(3. 27)

where t_r = 0.15 ps is the carrier density rising time, we can simulate the real part and imaginary part of the photo-induced conductivity of photoexcited GaAs, as shown in Figure 3-15 (b) and (d). From the results of simulation, the artificial conductivities in the beginning of the photoexcitation are similar to those resulting from analysis of the experimental data using the Kindt and Schmuttenmaer's method, as shown in Figure 3-15 (a) and (c).
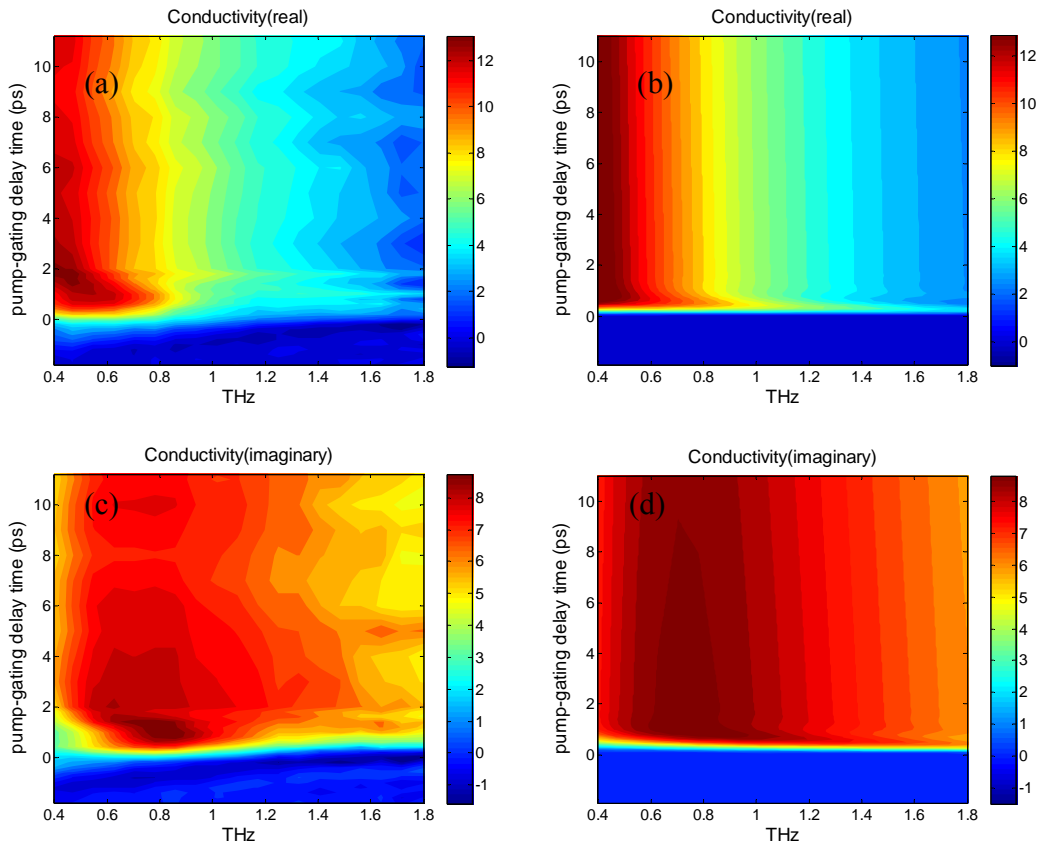
Figure 3-15 Two-dimensional (2D) contour plot of real part (a) and imaginary part (c) of photo-conductivities using Kindt and Schmuttenmaer's analytic method. (b) and (d): Simulation results of real part (b) and imaginary part (d) of photo-conductivities.
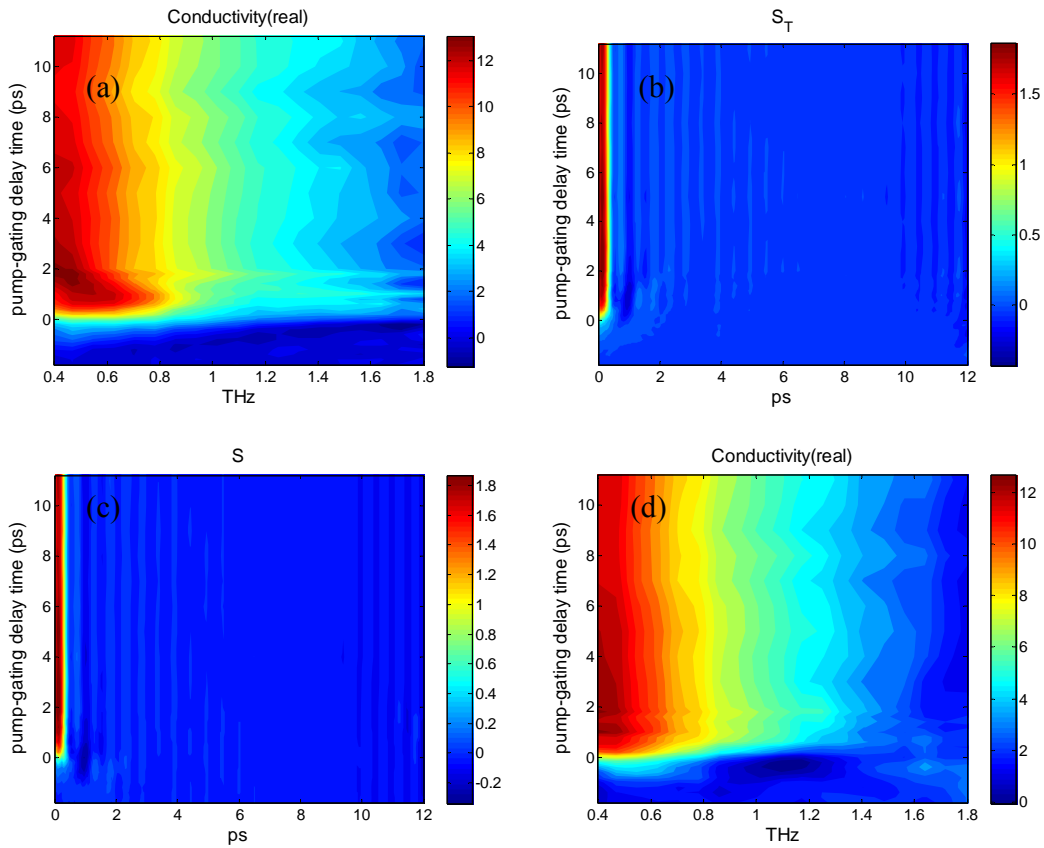
Figure 3-16 Two-dimensional (2D) contour plot of (a) real uncorrected photo-conductivity of photoexcited GaAs in the frequency domain; (b) the uncorrected photo-conductivity in the time domain; (c) the corrected photo-conductivity in the time domain; (d) the corrected photo-conductivity in the frequency domain.

Now we apply the correction transformations, as discussed in section 3.3.3, to the uncorrected conductivity data. The uncorrected real conductivity is shown in Figure 3-16 (a). First we transform the frequency domain data to the time domain using equation (3. 22), and the result is shown in Figure 3-16 (b). Next, we apply the equation (3. 23) to make the 45 degree axis transformation. Figure 3-16 (c) shows the results and is actually the product of the time dependent carrier density function and the single charge current response function. In the last step, we transform the result back to the frequency domain using equation (3. 24), and the result of the corrected conductivity is shown in Figure 3-16 (d). Comparing Figure 3-16 (a) and (d), it is clear that the artificial conductivities disappear after the correction transformation.
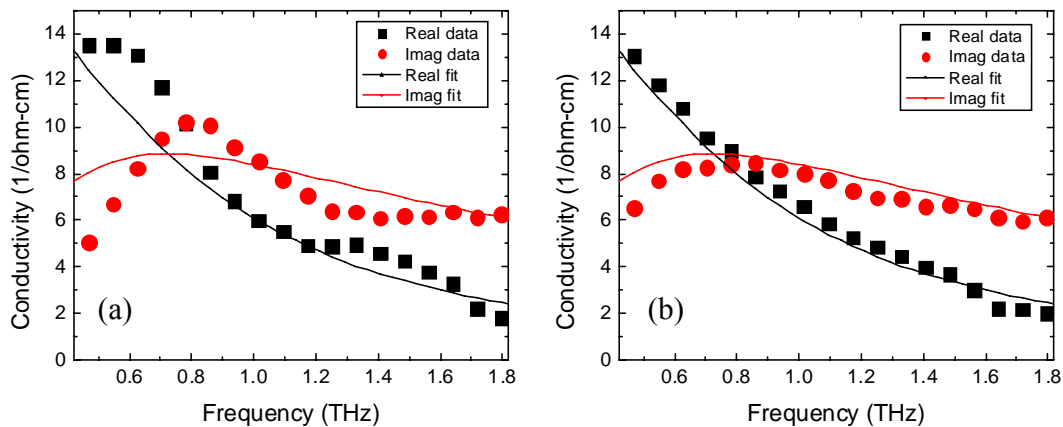
Figure 3-17 (a) uncorrected and (b) corrected complex photo-induced conductivity of photoexcited GaAs at the time 0.8 ps after the initial photoexcitation. The lines show the Drude model fit.

Figure 3-17 shows the uncorrected and corrected complex photo-induced conductivity of photoexcited GaAs at the time 0.8 ps after the initial photoexcitation. The lines show the Drude model fits using the parameters in Table 3-1, which are obtained from the conductivity measured at the time 10 ps after the photoexcitation. For the uncorrected data in Figure 3-16 (a), the conductivities deviate from the conductivities obtained the later time in the steady state condition. However, after the data correction transformations, the conductivities at 0.8 ps basically are the same as the conductivities measured at later time and follow the simple Drude model.

From this experiment, we establish the correct measurement and analysis methods for OPTP-TDS to obtain the time-resolved photo-induced conductivity. The photo-induced conductivities of photoexcited GaAs from just after excitation to the time 10 ps after excitation basically follow the simple Drude model. The artificial conductivities at the beginning of the excitation predicted by Nienhuys and Sundstrom are observed, and the true transient conductivities are obtained by applying the correction transformations to the Kindt and Schmuttenmaer's OPTP-TDS analysis method.

Chapter 4: Photo-induced Carrier Dynamics in P3HT/PCBM Blends

4.1 Introduction

Photovoltaic devices based on bulk heterojunctions consisting of conjugated polymer and fullerene composites have been intensively investigated recently as alternative renewable energy sources. The development of this technology promises to produce low-cost solar energy harvesting devices capable of being implemented on large area surfaces with high form factor. The current state-of-the-art power-conversion efficiency of 6% has been reported using regio-regular poly(3-hexylthiophene) (P3HT) as donor and [6,6]-phenyl-C_{61}-butyric acid methyl ester (PCBM) as acceptor molecules (see Figure 4-1 for molecular structures) in a tandem cell device structure [28]. The efficiency of these photovoltaic devices is governed by a series of optoelectronic processes starting with light absorption, followed by ultrafast charge-transfer from donor to acceptor and subsequent exciplex dissociation into electron and hole, and concomitant charge transport and collection to the respective electrodes [77]. Understanding the charge dynamics in each of these processes is critical towards the development of high efficiency polymer-based solar cells.

Time domain terahertz (THz) spectroscopy is a powerful non-contact technique for measuring both the real and imaginary parts of the complex conductivity, allowing an investigation of transient dynamics of carriers in semiconducting polymers by means of optical-pump THz-probe time domain spectroscopy (OPTP-TDS) [48] [50][77] [78]. Recently, Nienhuys and Sundstrom's theoretical analysis of the optical-pump terahertz-

probe experiment points out that there are significant complications in obtaining correct conductivities from experimental data for times just after the sample is photoexcited [29]. In chapter 3, we conducted time resolved photoconductivity measurements of GaAs and verified the theoretical analysis. In this chapter, we study the charge-carrier dynamics in P3HT/PCBM blends using the modified THz data analysis processes suggested by Nienhuys and Sundstrom. We find that a significant drop in conductivity during the first pico-second after carrier generation is mainly due to the time dependence of the mobility.
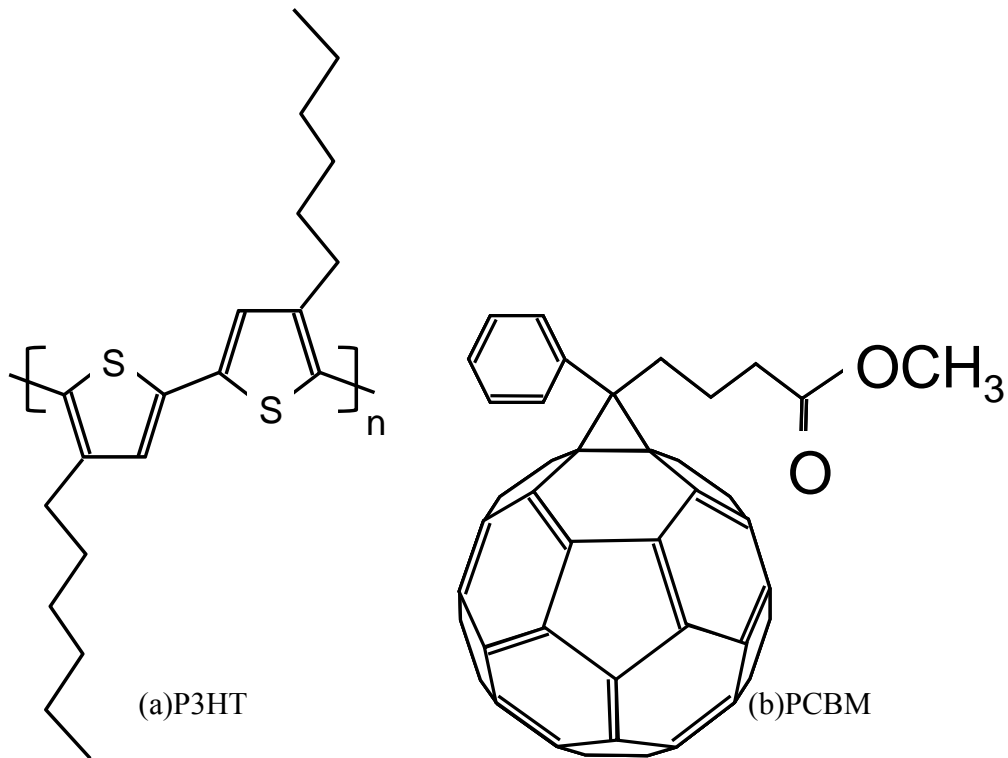
Figure 4-1 Molecular structure of (a) Poly(3-hexylthiophene) (P3HT), and (b) [6,6]phenyl-C_{61}-butric acid methyl ester (PCBM)

4.2 Experimental methods

Organic bulk heterojunctions consisting of a blend of regioregular P3HT (Rieke Metals, 90~93% regioregular) as donor and PCBM (Nano-C) as acceptor molecules were investigated for this work. The photovoltaic characteristics of devices fabricated using these materials as the active layer are known to depend on the blend composition. To study the carrier dynamics that are responsible for the photovoltaic properties, a series of P3HT:PCBM solutions of varying ratio by weight (weight ratio = 1:0, 4:1, 1:1, 1:4, and 0:1) were prepared. The solutions were stirred overnight at $50^{o}C$ to uniformly disperse the organic components in dichlorobenzene. Films, approximately 10 μm thick were prepared by drop-casting the solution onto a quartz substrate and allowed to dry slowly at room temperature to promote the ordering of the P3HT chains. We estimate the optical densities (OD) of the samples at 400 nm wavelength to be larger than 3.0, which ensures that the sample absorbs all of the excitation light. The films were prepared under nitrogen atmosphere inside a glovebox system to minimize the photo-oxidative degradation.

Details of the setup of the optical pump THz probe time domain spectroscopy measurement (OPTP-TDS) were discussed in chapter 3. A 1 mJ, 800 nm, 100 fs amplified Ti:sapphire laser with 1 kHz repetition rate is used as the fundamental laser source for the THz system. The THz probe pulses, about 1 ps duration single cycle electromagnetic pulses, are generated via optical rectification by shining 350 μJ, 800 nm pulses onto a 1-mm-thick [110] ZnTe crystal. The THz pulses are collected, collimated, and focused onto the sample with 90 degree off-axis gold coated parabolic mirrors to generate the THz peak electric field of about 0.8 kV/cm. At the same time the samples

are pumped with 300 μJ, 400 nm pulses (fluence = 3×10^{19} photons/m^2) obtained from second harmonic generation of the 800 nm pulses using an optical frequency doubler. The 400 nm pump pulse has a beam diameter of 5 mm, which is much larger than the 1 mm diameter of the THz probe pulse at the sample ensuring a uniform excitation of the probed region. The THz probe pulses are transmitted through the photoexcited sample to modulate the carrier density. The pump-induced modulation of the THz electric field is less than 1% in the measurement, as shown in Figure 4-2. The transmitted THz pulses are again collected, collimated and focused onto another 1-mm-thick [110] ZnTe crystal. The pulses are collinear with the 10 nJ of 800 nm gate pulses to measure the electric field amplitude via the free space electro-optic sampling.
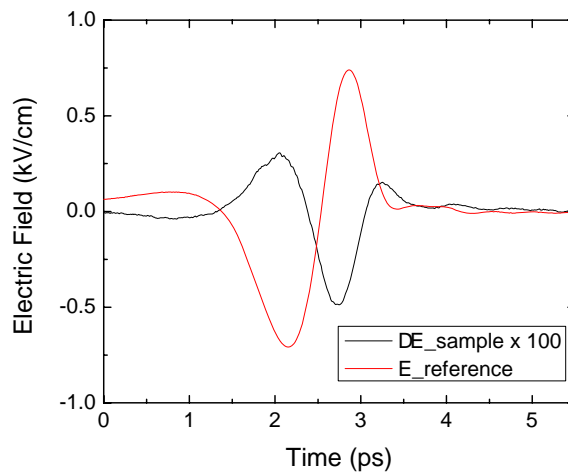
Figure 4-2 The electric field E(t) of the THz pulse (red line) transmitted through the P3HT/PCBM 1:1

blend sample with the modulation ΔE(t) measured 2 ps after photoexcitation (black line)

87

The experimental data are collected by the two-dimensional (2D) scan method as described in Refs [41][46]. A series of THz difference waveforms are obtained by chopping the optical pump pulses and delaying the optical pump arrival time. We use a mechanical vibrator to drive a retroreflector to get the rapid scan (1 Hz) in order to minimize the effect of degradation of the polymer, as we discussed in section 3.2. Each THz difference waveform scan is obtained by averaging 1000 rapid scans on an oscilloscope (about 15 minutes), and has different optical pump arrival times in increments of 0.5 ps, as shown in Figure 4-3. The distortion from the detector response of 1-mm-thick ZnTe crystal is deconvolved numerically from each measured wave form, as we described in section 2.3.2.3. The data are processed so that each point in the measured waveform has passed through the sample after the same amount of time from the photoexcitation event [46].
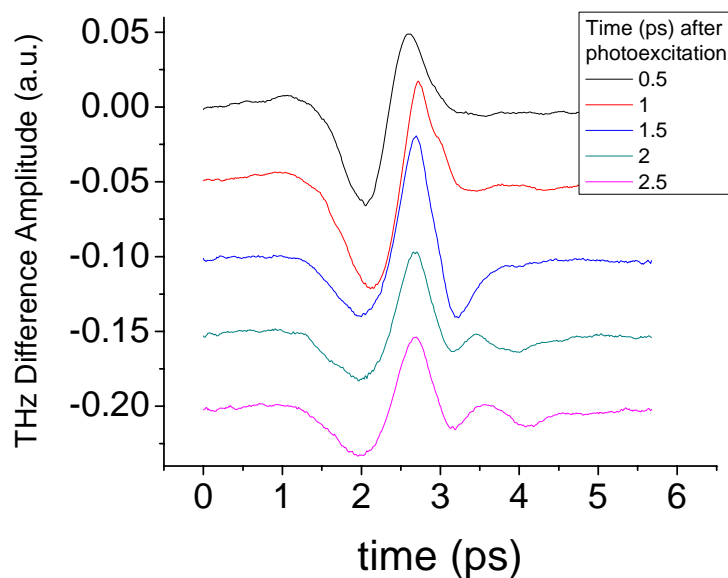
Figure 4-3 Several THz difference scans in photoexcited P3HT measurement for different probing times.

Equation (3.6) and (3.7) are used to calculate the complex conductivity. The terahertz refractive indices of the P3HT/PCBM blends are approximated by the weight average of P3HT, the index = 2.22, and PCBM, the index = 1.35 [49]. The skin depth of the blends for 400-nm photoexcitation can be calculated from the optical absorption spectra of P3HT and PCBM [80], as shown in Figure 4-4. The 2-D real and imaginary conductivity contour plots are obtained by calculation directly from each different waveform scan, as shown in Figure 4-5 (a) and (c). In the final step, the correction transformations as we discussed in section 3.3.3 are applied to the uncorrected conductivity data, and the corrected true complex conductivity is shown in Figure 4-5 (b) and (d).
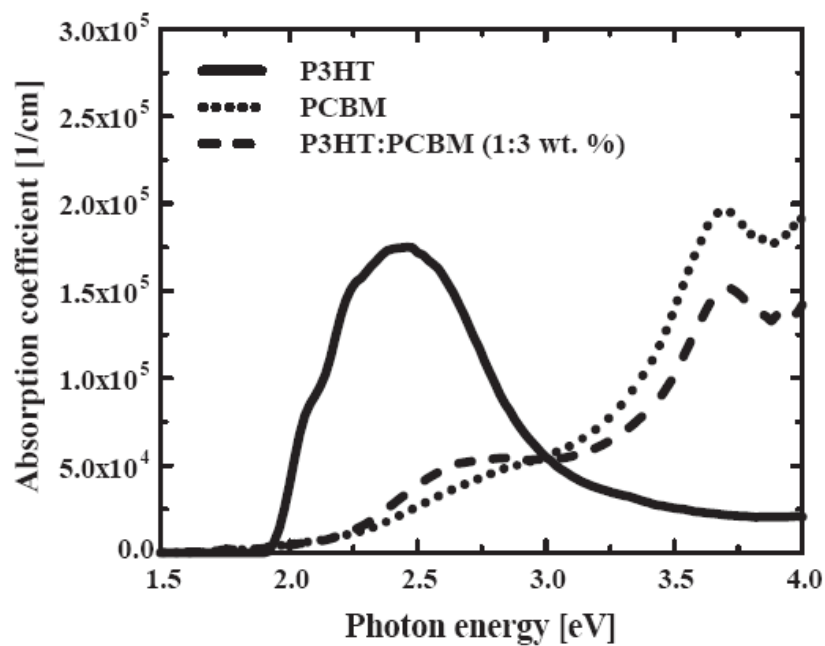
Figure 4-4 Optical absorption spectra of P3HT, PCBM, and a blend of both (1:3 wt%) in film [80].
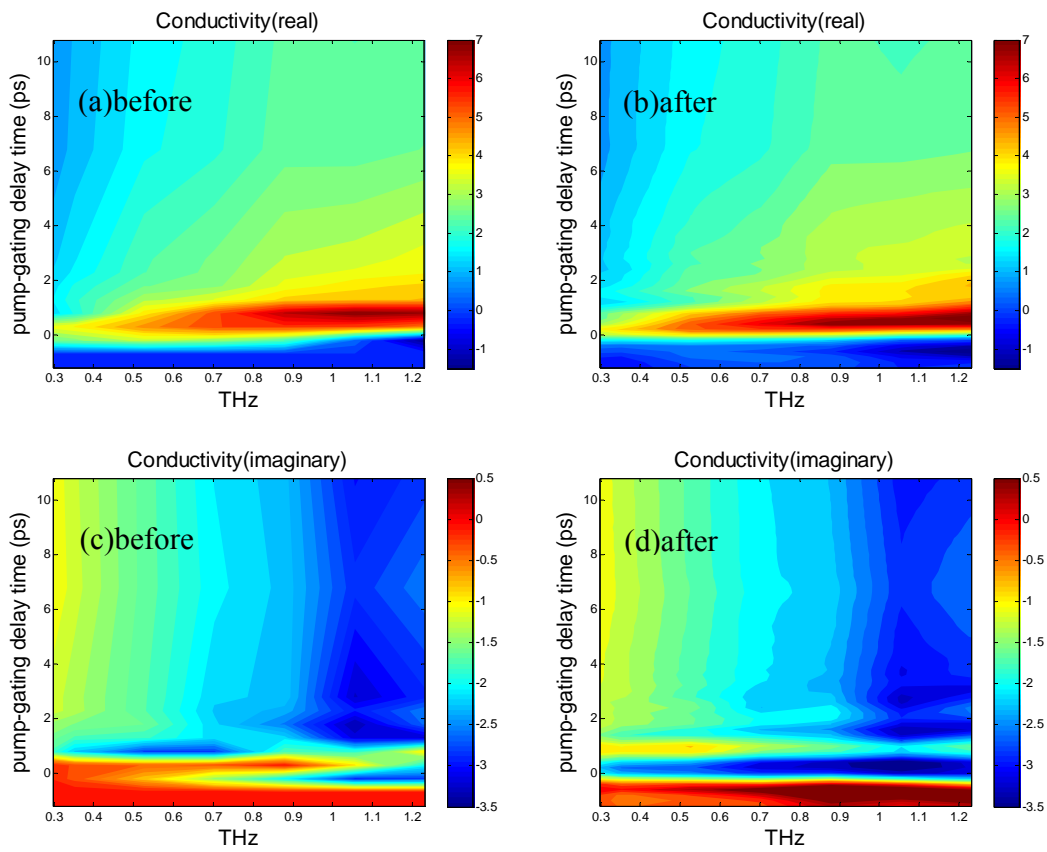
Figure 4-5 2-D real and imaginary conductivity contour plots of P3HT/PCBM 1:1 before (a,c) and after

(b,d) correction transformation.

4.3 Analytic methods

4.3.1 Drude-Smith model

The Drude-Smith model was derived by N. V. Smith [75] based on the impulse response approach and Poisson statistics. It is used to describe the infrared properties of poor metals that display a peak in the optical conductivity at nonzero frequency, which cannot be explained by simple Drude model. The model is derived in the following paragraphs.

In probability theory, the Poisson distribution is a probability distribution that describes the probability of a number of events occurring in a fixed period of time if these events occur with a known average rate and independently of the time since the last event. The equation is

$$f(k,\lambda) = \frac{\lambda^k \exp(-\lambda)}{k!} \quad , \tag{4.1}$$

where k is the number of occurrences of an event, and λ is the expected number of occurrences that occur during the given interval. Suppose that a charge experience collisions that are randomly distributed in time but with an average time interval τ between collision events. The probability $p(N, t/\tau)$ of N collision events in the time interval (0,t) is then given by

$$p(N, \frac{t}{\tau}) = \frac{\left(\frac{t}{\tau}\right)^N \exp(-\frac{t}{\tau})}{N!} \quad,$$

(4. 2)

Assume that the initial impulse response current at time 0 is *j(0)*, then the impulse response current at time t is the product of the initial current and all possibilities of collision events:

$$j(t) = j(0) \cdot \left(p(0,\frac{t}{\tau}) + p(1,\frac{t}{\tau}) + p(2,\frac{t}{\tau}) + \cdots + p(n,\frac{t}{\tau}) + \cdots \right)$$

$$= j(0) \cdot \exp(-\frac{t}{\tau}) \cdot \left(1 + c_1 \frac{(\frac{t}{\tau})^1}{1!} + c_2 \frac{(\frac{t}{\tau})^2}{2!} + \cdots + c_N \frac{(\frac{t}{\tau})^N}{N!} + \cdots \right)$$

$$= j(0) \cdot \exp(-\frac{t}{\tau}) \cdot \left(1 + \sum_{N=1}^{\infty} c_N \frac{(\frac{t}{\tau})^N}{N!} \right) \quad,$$

(4. 3)

where the coefficient c_N represents that fraction of the charge's original velocity that is retained after the *N*th collision. It can be interpreted as a memory or persistence of velocity effect. The complex frequency-dependent conductivity is the Fourier transform of *j(t)*. Therefore,

$$\tilde{\sigma}(\omega) = \int_0^{\infty} j(t) \exp(i\omega t) dt$$

$$= \frac{ne^2\tau/m}{(1-i\omega\tau)} \left(1 + \sum_{N=1}^{\infty} \frac{c_N}{(1-i\omega\tau)^N} \right) \quad.$$

(4. 4)

92

This generalized Drude formula is what we called Drude-Smith model. In the case that there is no memory effect in the scattering events ($c_N = 0$), the Drude-Smith model reduces to the original simple Drude model.

Under the first order approximation, we assume that persistence of velocity is retained for only one collision ($c_N = 0$ for n>1), and the truncated Drude-Smith model becomes

$$\widetilde{\sigma}(\omega) = \frac{ne^2\tau/m}{(1-i\omega\tau)}\left(1+\frac{c}{(1-i\omega\tau)}\right) \quad .$$

(4. 5)

The effects of persistence of velocity in the real part and imaginary part of conductivity are shown in Figure 4-6. In the real part of conductivity, when c is equal to 0 (Drude), the maximum conductivity is at zero frequency. When c is a negative number, the maximum conductivity shifts to some non zero frequency. The differences are also shown in imaginary conductivity. When c is close to -1, the conductivity even goes to negative values in the low frequency region. Smith applied this model to some poor conductors which have unusual low-frequency behavior of conductivities. He successfully modeled the conductivity of liquid mercury with a value c= -0.49, and the conductivity of the quasicrystal compound $Al_{63.5}Cu_{24.5}Fe_{12}$ with a value c= -0.973 for the persistence of velocity parameters.
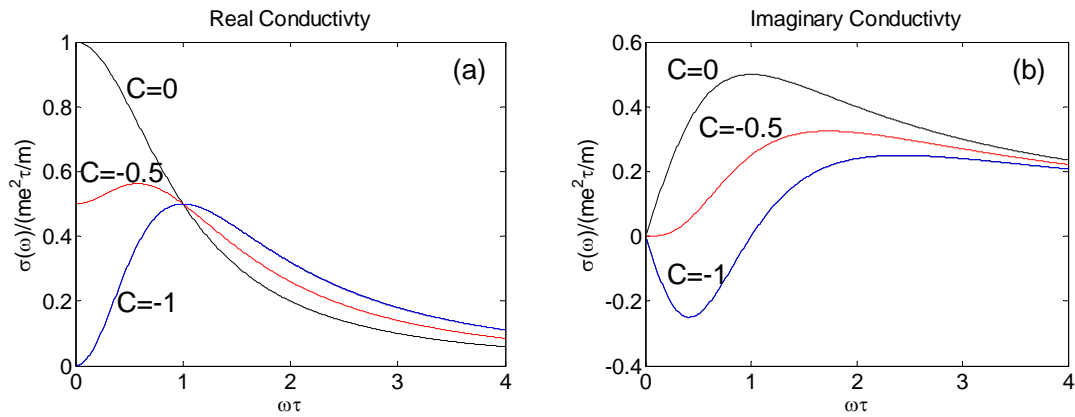
Figure 4-6 The effects of persistence of velocity in (a) real part and (b) imaginary part of conductivity.

In the data analysis, the average effective mass of carriers in the Drude-Smith model for the P3HT/PCBM blends is held constant at 1.7 m_e [79]. The Drude-Smith model is used to fit the conductivity spectra data obtained from processed experimental data discussed in previous section. The least squares fitting method is used to fit both real and imaginary parts of conductivity simultaneously. The carrier density, scattering time, and parameter c can be extracted from the fit for a given photoexcitation time.

4.4 Results and Discussion

4.4.1 Short Term Conductivity

Figure 4-7 shows the real part and imaginary part of the frequency dependent conductivity of photoexcited P3HT/PCBM 1:1 blend before and after the correction transformations for 0.5 ps after photoexcitation. The solid lines are the results of a fit of the data using the Drude-Smith model. Comparing the uncorrected conductivities with the corrected conductivities, some obvious differences are observed. In the real part of the conductivities, the uncorrected data are underestimated at lower frequency. On the other hand, the uncorrected data are overestimated at lower frequency and underestimated at higher frequency in the imaginary part of the conductivities. When we apply the Drude-Smith model to fit the data, the corrected conductivities allow better fitting of the results than the uncorrected data, as shown in lines in Figure 4-7. It is similar to the GaAs measurement that the corrected data have better fitting to a pure Drude model than the uncorrected data in the early times after photoexcitation.
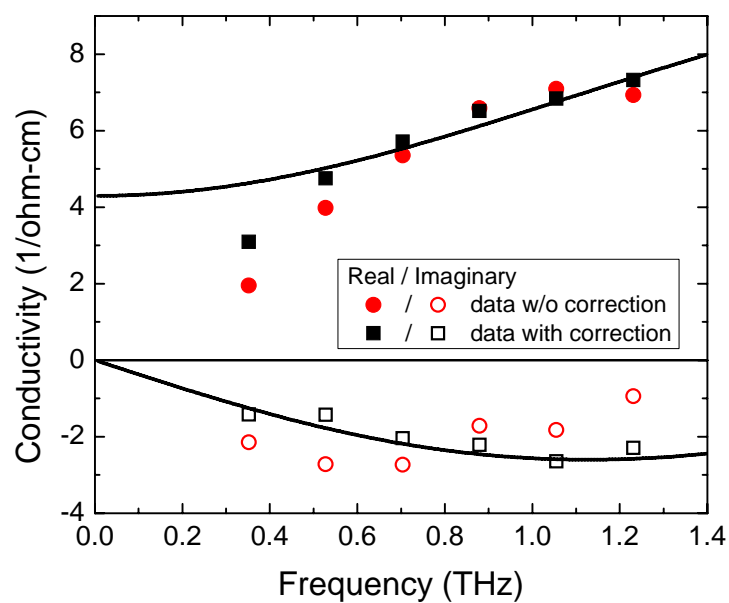
Figure 4-7 The real part and imaginary part of the frequency dependent conductivity of photoexcited P3HT/PCBM 1:1 blend before and after the correction transformations for times 0.5 ps after photoexcitation. The lines are the results of Drude-Smith model fit.
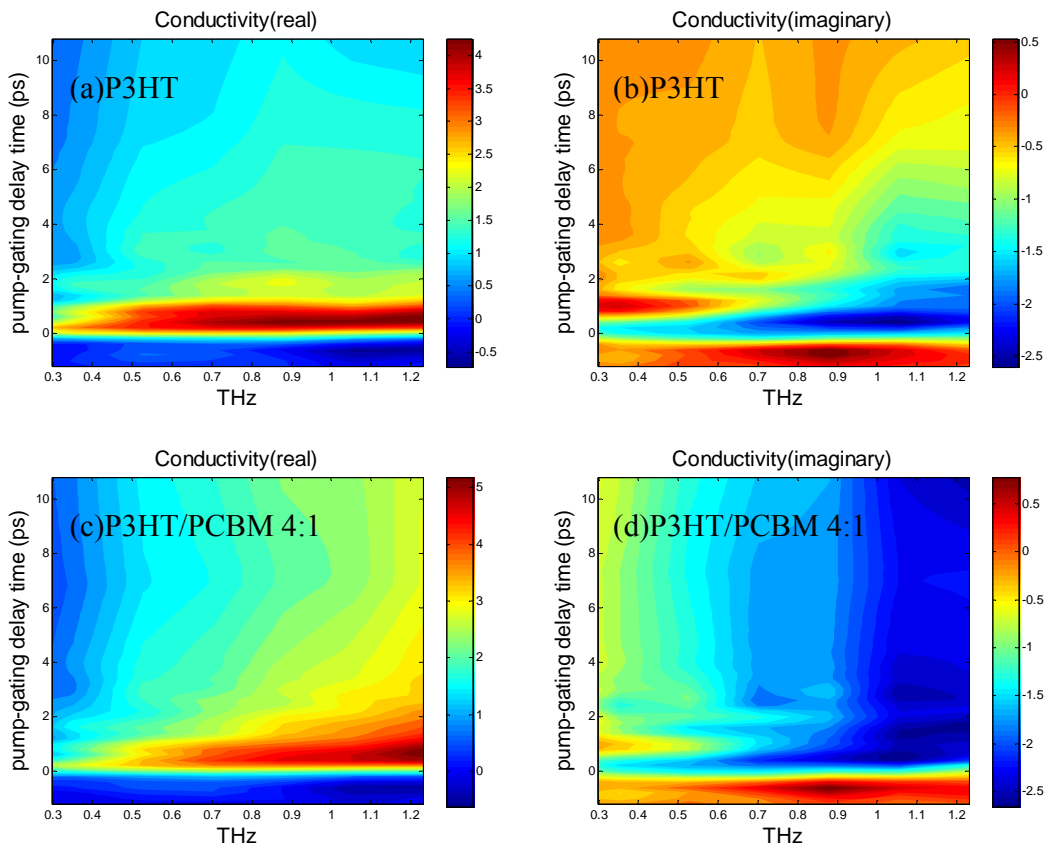
Figure 4-8 Corrected 2-D real and imaginary time-resolved conductivity spectra contour plots of P3HT (a) and (b), P3HT/PCBM 4:1 (c) and (d)
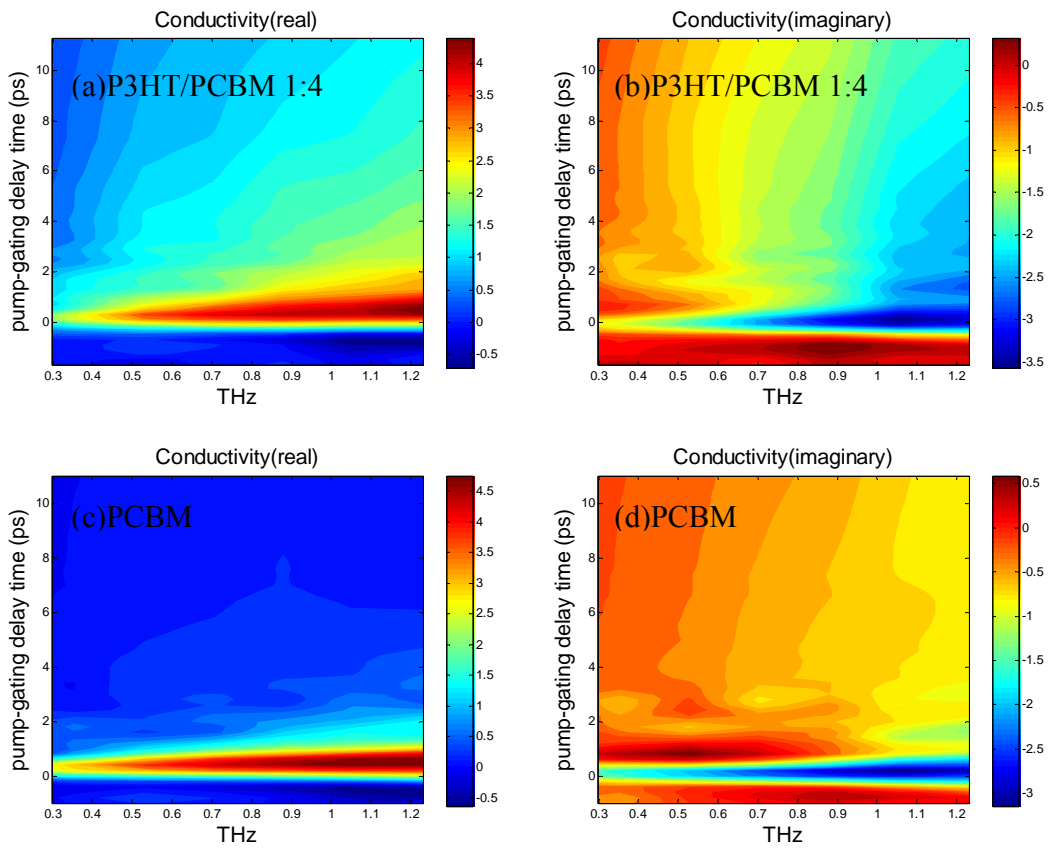
Figure 4-9 Corrected 2-D real and imaginary time-resolved conductivity spectra contour plots of P3HT/PCBM 1:4 (a) and (b), and PCBM (c) and (d)

Figure 4-8, Figure 4-9, and Figure 4-5 (b,d) show the corrected 2-D real and imaginary time-resolved photo-induced conductivity spectra contour plots of P3HT, P3HT/PCBM 4:1 blend, 1:1 blend, 1:4 blend, and PCBM. In order to compare the conductivity in different blends, we slice the corrected 2D time resolved conductivity spectra at frequency 1 THz, and the result of the corrected real (σ_{real}) and imaginary (σ_{imag}) parts of the time-resolved conductivity of P3HT/PCBM blends at 1 THz from -2 to 10 ps delay time is shown in Figure 4-10. Presenting the data this way for carrier dynamics is different from the traditional method, which is to measure the time resolved transmittance changes of the peak of the THz probe [48][77][50][78]. This method avoids the influence of the time profile of the THz probe pulse to the peak transmittance changes measurement, which is the result of the convolution of the THz probe pulse, carrier density function, and single charge impulse response [29]. For different blend ratios, the P3HT/PCBM 1:1 blend has the highest conductivity. Figure 4-11 shows the results of comparing the real conductivity of different P3HT/PCBM blends at frequency of 1THz at the time 2.5 ps after photoexcitation. It agrees with the results of P3HT/PCBM photocell measurements that 1:1 blend give the best performance. The data also show two different temporal behaviors for real conductivity for all blends. The first one is the very fast rise and fast decay in the first pico-second. The second one is a slower gradual decay after 2 ps. For the time resolved imaginary conductivities, the mixtures (0.8, 0.5, and 0.2 blends) don't change much after photoexcitation, while the pure materials (P3HT and PCBM) change like their real parts do.
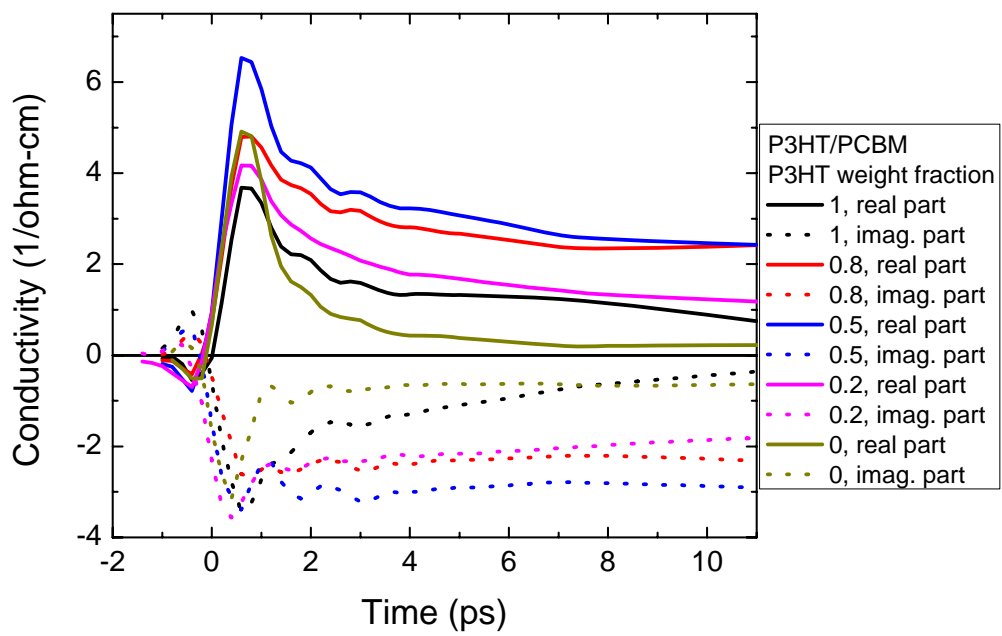
Figure 4-10 Time-resolved complex conductivity of P3HT/PCBM blends at frequency = 1 THz
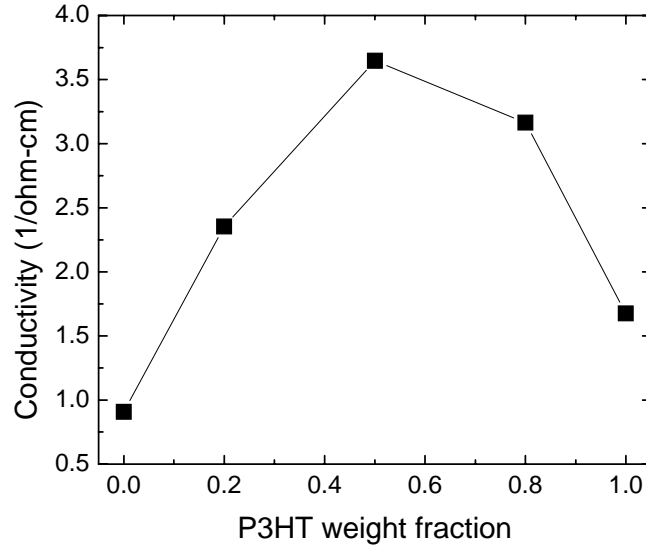
Figure 4-11 Real conductivities for 1 THz at 2.5 ps after excitation versus different P3HT/PCBM blend ratio.

In order to analyze these dynamics, model fitting to the time resolved conductivity spectrum is carried out to obtain other physical properties. Figure 4-12 shows the complex conductivity at the probe delay time 0.5, 1.5, and 8.5 ps for the different weight ratio of the P3HT/PCBM blends. The lines are the results of fitting using the Drude-Smith model, and the extracted parameters are shown in Table 4-1. The scattering time, τ, plasma frequency, ω_p, and the parameter of persistence of velocity, c, were extracted directly from the fitting. The dc mobility, $\mu\_DC = e\,\tau/m^*[1+c]$, and carrier density, $N = \varepsilon_0 \omega_p^2 m^*/e^2$, can be obtained by assuming 1.7 m_e as the effective mass [79]. Indeed, the uncertainties in the effective mass affect the uncertainties in the values of the mobility and carrier density. Nevertheless, we can still compare the relative changes of the time resolved properties for the same material.
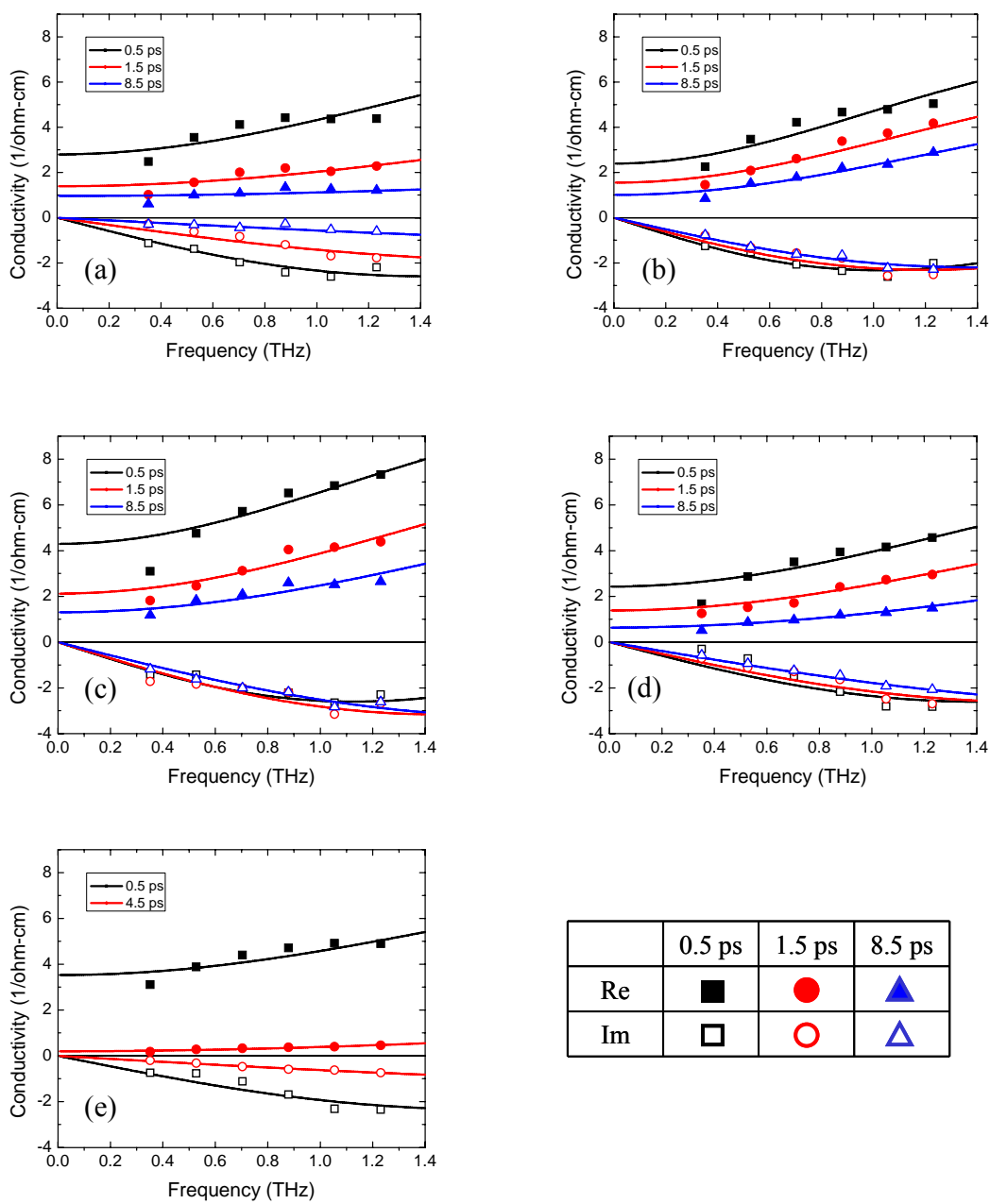
Figure 4-12 Complex conductivity at the probe delay time 0.5, 1.5, and 8.5 ps for (a) pure P3HT, (b) P3HT/PCBM 4:1, (c) P3HT/PCBM 1:1, (d) P3HT/PCBM 1:4, and (e) pure PCBM Lines are the fit with Drude-Smith model.

Table 4-1 Results of the application of a Drude-Smith model based analysis of frequency dependent

conductivity data measured for the P3HT/PCBM blends at probe delays of 0.5, 1.5, 2.5, 4.5, and 8.5 ps

Delay (ps)	τ (fs)	$e\tau/m^*$ (cm²/Vs)	N (x10¹⁸ cm⁻³)	Yield (%)	C	μ_DC (cm²/Vs)
			P3HT			
0.5	42	43	2.46	1.64	-0.84	7.1
1.5	31	32	2.11	1.41	-0.87	4.1
2.5	31	32	1.59	1.06	-0.87	4.1
4.5	30	31	1.49	0.99	-0.86	4.3
8.5	29	30	1.08	0.72	-0.83	5.1
			P3HT:PCBM 4:1			
0.5	58	60	1.56	1.04	-0.84	9.6
1.5	51	53	1.53	1.02	-0.88	6.3
2.5	48	49	1.56	1.04	-0.89	5.4
4.5	48	49	1.45	1.14	-0.9	4.9
8.5	45	46	1.5	1	-0.91	4.2
			P3HT:PCBM 1:1			
0.5	50	52	2.47	1.65	-0.79	10.9
1.5	42	44	2.55	1.7	-0.88	5.2
2.5	38	40	2.62	1.75	-0.9	4
4.5	39	40	2.47	1.65	-0.9	4
8.5	34	35	2.92	1.96	-0.92	2.8
			P3HT:PCBM 1:4			
0.5	42	44	2.33	1.55	-0.85	6.5
1.5	37	38	2.26	1.51	-0.9	3.8
2.5	36	37	2.06	1.38	-0.93	2.6
4.5	28	29	2.92	1.96	-0.94	1.7
8.5	27	28	2.84	1.9	-0.95	1.4
			PCBM			
0.5	34	36	3.09	2.06	-0.8	7.2
1.5	28	29	1.34	0.88	-0.88	3.5
2.5	24	25	1.29	0.85	-0.94	1.5
4.5	23	23	1.36	0.9	-0.96	0.9

The photon-to-carrier yields we observed for all blends are about 1~2%. The carrier yields agree with other OPTP-TDS reports [50][78], but are much lower than the efficiency obtained from the polymer solar cell measurements. A possible explanation lies in the built-in potential that is present for solar cell measurements but not for THz measurements. In a solar cell, the polymer is sandwiched between two different electrodes. Because of the different work functions of the two electrodes (e.g., aluminum and ITO), the polymer experiences a built-in electric field. The field can be as high as 10^5 V/cm, which is 2 orders of magnitude higher than the electric field of our THz probe. The build-in high electric field may help to dissociate the excitons generated by photoexcitation to free carriers. In contrast, the contactless polymer sample in OPTP-TDS measurement experiences no other electric field except the weak THz probe. Furthermore, the THz only last for 1~2 ps while the built-in potential is present at all times. That's why we observed a much lower quantum efficiency in OPTP-TDS than in the solar cell measurements.

The dc mobilities of P3HT/PCBM blends obtained from OPTP-TDS are several cm^2/Vs, as shown in Table 4-1. These values are several orders of magnitude larger than those measured at GHz frequencies [82]. The reason for the difference is that the dc mobilities we obtained here are the results of prediction from THz measurement. Because of the high frequency nature of the THz wave, the carriers driven by the THz field move only on a small length scale. The factors limiting the carrier mobility for long range transportation (e.g., disorders in the film) will not contribute to the THz mobility. It has been shown that the measured mobilities of the conducting polymers depend strongly on the probing frequency for the low frequency regime [83].

104

Figure 4-13 shows the dc mobility and carrier density for P3HT/PCBM 1:1 blend from the probe delay time 0 ps to 10 ps. The dc mobility drops significantly during the first pico-second and stays at the same value afterward, while the carrier density is almost constant after photoexcitation in this time period. Similar results can be found on P3HT/PCBM 4:1 and 1:4 blends. The results indicate that the significant drop in conductivity during the first pico-second after carrier generation is mainly due to the time dependence of the mobility.

To understand these differences, we recall that the free-carrier Drude conductivity for $\omega\tau \ll 1$ is $\sigma_{real} \approx Ne^2\, \tau\, /m^*$ where N is the carrier density, m^* and τ are the carrier effective mass and scattering time, respectively. Prior to 0.5 ps, the temporal conductivity response is due to increasing N, most likely associated with the rise time of the pump pulse intensity and exciton dissociation. After 0.5 ps, when free carriers are generated, charge-carrier transport is renormalized by interaction effects. In this case, the temporal conductivity response is governed by the mobility. In the Drude-Smith model, the dc mobility is $\mu\_DC = e\, \tau/m^*\left[1+c\right]$ and we assume the m^* is a constant. In our measurement results, the parameter c for the P3HT/PCBM blends decreases and is more closes to -1 after 0.5 ps. Recall that the parameter c is a measure of the persistence of velocity effect in the Drude-Smith model. A more negative value for the parameter c means more velocity damping. When the free carriers are generated, their electric field starts to induce polarization of the nearby molecules and forms polarons. The formation time of the polaron is sub-picosecond. The resulting polaron formation acts as a potential well that hinders the movements of the charge. In other words, the carriers become heavier, or the effective mass increases in the Drude model after polaron formation. This

105

explanation matches the observation of the decrease in the parameter c in the first picosecond after free carrier generation. Meanwhile, the carrier density does not change much in this period of time. Therefore, we conclude that the decrease of σ_{real} in the first picosecond after photoexcitation is attributed to a decrease in the parameter c (or an increase in m^* for the Drude model) due to polaron formation on a sub-picosecond time scale.

Comparing the rate of decrease of the parameter c for different P3HT/PCBM blends in Table 4-1, we notice that the higher weight ratio of PCBM in the blend has the higher rate of decrease. The result implies that the charge carriers in PCBM induce stronger polarons than those in P3HT do.
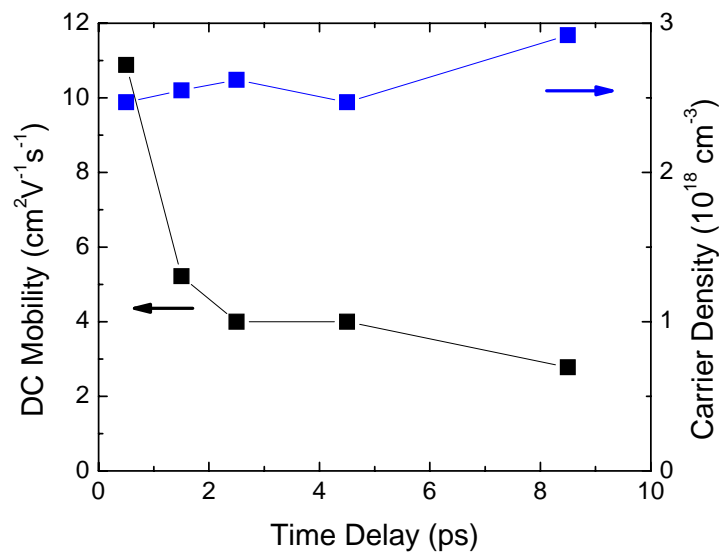
Figure 4-13 Comparison of time dependant DC mobility (left axis) and carrier density (right axis) for P3HT/PCBM 1:1 blend.

4.4.2 Long Term Conductivity

Figure 4-14 shows the long term (0~300 ps) conductivities of P3HT and P3HT/PCBM 1:1 blend. The data indicate that the conductivity of P3HT/PCBM 1:1 blend decays slower than that of pure P3HT. This phenomenon can be explained by the following picture. The lowest unoccupied molecular orbital (LUMO) energy and the highest occupied molecular orbital (HOMO) energy of P3HT is 3.2 eV and 5.1 eV, respectively, while the HOMO and LUMO energy of PCBM is 4.3 eV and 6.1 eV [28]. When electrons or holes are generated in the P3HT/PCBM blend material, electrons in P3HT will transfer to PCBM and holes in PCBM will transfer to P3HT to lower energy levels, as shown in Figure 4-15. Therefore, electrons and holes will transport separately in the different media. The chance of electron-hole recombination is reduced in this manner, so the carriers have longer life time. On the other hand, both types of carriers will transport in the same media when they are generated in the neat material (e.g., P3HT). The chance of electron-hole recombination becomes higher. Thus, the carriers suffer a shorter life time.
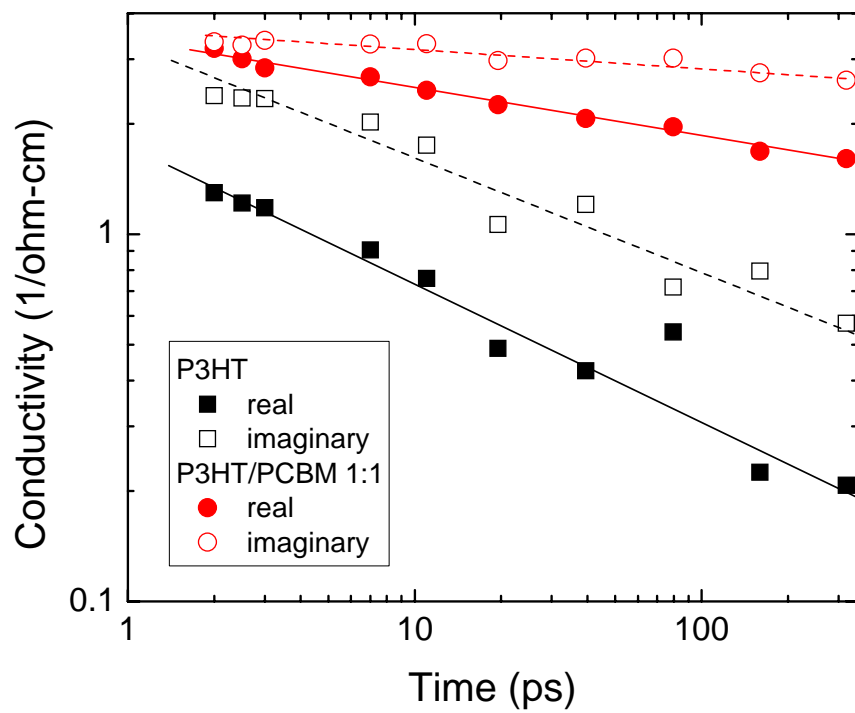
Figure 4-14 Decay of the long term conductivities for P3HT and P3HT/PCBM 1:1 blends.
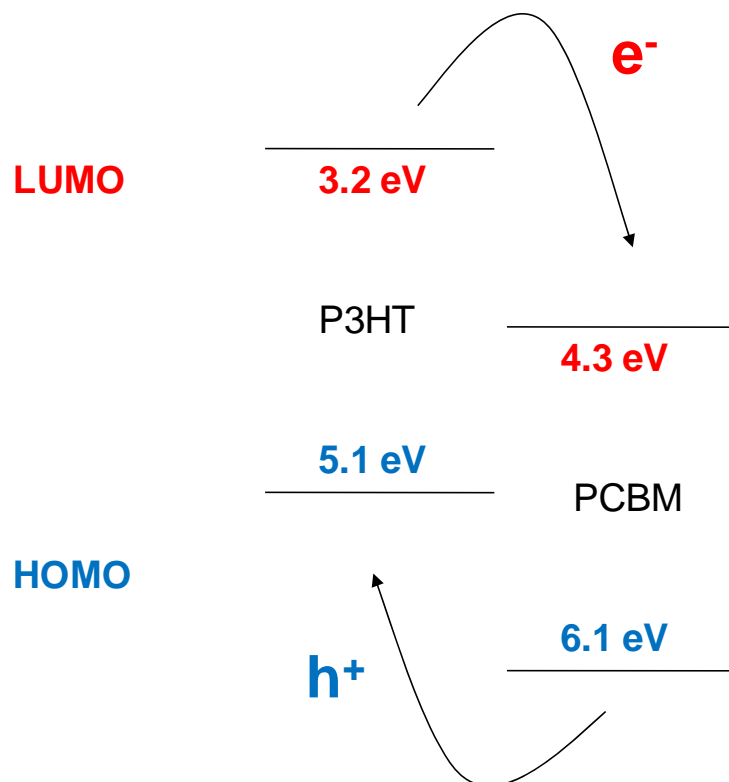
Figure 4-15 Energy levels of P3HT and PCBM. The energy diagram show the HOMO and LUMO

molecular orbitals of the materials, and the arrows show the direction of electron (e⁻) and hole (h⁺) transfer.

4.5 Conclusions

We have investigated the photoinduced carrier dynamics of P3HT/PCBM blends using OPTP-TDS with subpicosecond resolution. The data process method suggested by Nienhuys and Sundstrom is used for the first time on experimental data to obtain the time resolved frequency dependent complex photoconductivity with subpicosecond resolution. The time resolved conductivity is analyzed using the Drude-Smith model to determine the photon-to-carrier yields, average carrier mobility, and carrier density. The result that a 1:1 blend film shows the highest conductivity among other blends is consistent with independent photovoltaic measurements. The significant drop of real conductivity in the first picosecond after photoexcitation for P3HT/PCBM blends can be attributed to the transient mobility change due to polaron formation within sub-picosecond time scale. We also measure the long term conductivity of the polymers and find that the difference of the free carrier life time of neat P3HT and P3HT/PCBM blend can be explained by the interchain interaction of charge carriers.

Chapter 5: Transient photoinduced properties of MEH-PPV

5.1 Introduction

Electrically conducting polymers have attracted considerable attention since the first report of metallic conductivities in doped polyacetylene in 1977, [56] and subsequent research has led to progress in understanding the physics of conduction in polymers. As high-purity polymers have become available, a series of semiconducting polymer devices have been realized, ranging from light-emitting diodes (LEDs), solar cells, photodetectors, thin film transistors, to plastic lasers [57][58][59][60][61][62][63]. Although considerable progress has been made toward understanding the properties of semiconducting polymers, some issues still remain controversial. An unresolved question is whether the photocarriers are generated via direct interband excitations and relaxations [64] or via exciton formation and dissociation afterwards [65]. Some earlier work indicated the presence of free carriers in the photocarrier generation process [66], but limited time resolution made it difficult to resolve the excitation process. More recently, researchers employed THz time domain spectroscopy (THz-TDS) to study the carrier dynamics [48][67]. This gives a better time resolution and explains the conductive and dielectric properties well around 1 THz. Direct measurement of photoconductivity can be achieved by photo-conductive sampling, which has a time resolution only restricted by the laser pulsewidth and the RC time constant of the sample device structure. With a carefully designed structure, a resolution of subpicosecond can be obtained. Recently, direct measurement of photoconductivity in a polyphenylenevinylene (BAMH-PPV) was

reported [68] using two photoconductive switches, one as signal generator and the other as sampler. The resolution was limited to 2 ps because of the capacitance of the complicated structure. Other electronic properties, such as carrier density and carrier mobility, were not directly obtained but estimated after assuming a value for quantum efficiency. Using ultrafast measurements of transient excited-state absorption in the spectral region spanning the infrared-active vibrational (IRAV) modes in poly{2-methoxy-5-(2'-ethyl-hexyloxy)-p-phenylene} (MEH-PPV) (see Figure 5-1), Heeger's group reported that charge carriers were generated within 100 fs after photoexcitation and a photocarrier quantum efficiency of 10% in MEH-PPV was achieved [69]. Those were inconsistent with the predictions of traditional exciton-based models of carrier generation for conjugated polymers (e.g., the Onsager model) [70] and with a more recent report using THz to probe photocarrier generation in MEH-PPV [48]. This report quoted a photocarrier generation quantum efficiency of less than 1%.

In this chapter, we report the measurement of photocarrier dynamics using both conductive and dielectric properties of the polymer film. Photoconductivity was directly measured with two equal intensity 400 nm femtosecond laser beams. Both laser beams illuminate the same MEH-PPV switch with variable time delay to study the dynamic photoconductive properties. We also report the measurement of photo-induced change in reflectivity in MEH-PPV using a two-color femtosecond laser system (400 nm pulse as pump and 800 nm pulse as probe). In addition, the complex conductivity of photoexcited MEH-PPV films was investigated by THz-TDS, which separates the transient dynamics of the real part and the imaginary part of the photoconductivity. For the same pump intensity, the test results in all three wavelength regions (DC, THz, and ooptical) are

112

consistent. Free photocarrier quantum efficiency of 10^{-3} was obtained. A peak transient mobility up to 23 cm^2/Vs was estimated for the free photocarriers. All three measurements verified that the fast part of the lifetime of the photocarriers in MEH-PPV is less than 1ps.
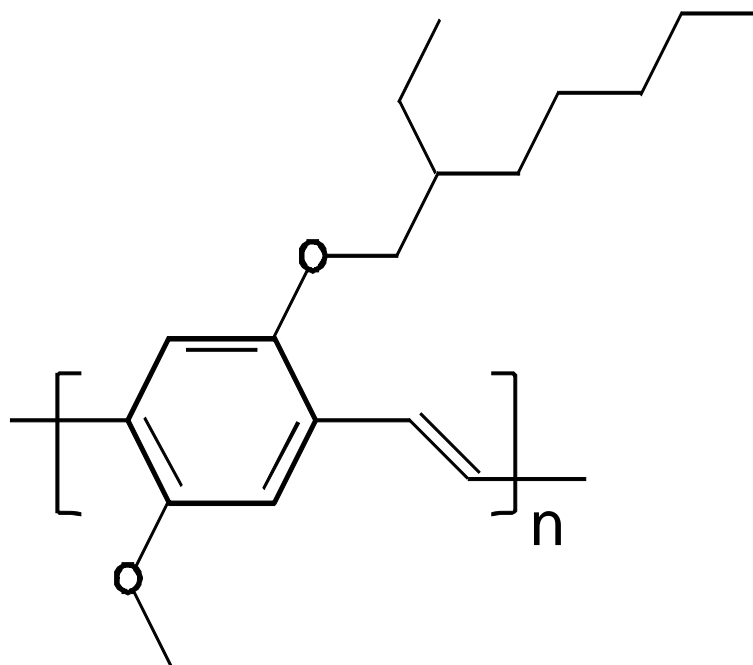
Figure 5-1 Molecular structure of poly{2-methoxy-5-(2'-ethyl-hexyloxy)-p-phenylene} (MEH-PPV)

5.2 Experimental methods

5.2.1 MEH-PPV preparation

MEH-PPV samples were prepared in a nitrogen filled glove box to minimize photo-oxidation. Four sets of samples were prepared for UV-VIS-NIR absorption measurement, OPTP-TDS measurement, DC-bias transient photoconductivity measurement, and photo-induced reflectivity change measurement, respectively. The first set of films, which have thickness 100 nm, were made by spin-coating onto quartz substrates to measure the absorption coefficient. Figure 5-2 shows the absorption spectrum of MEH-PPV in the UV-VIS-NIR region. The result shows that MEH-PPV has an absorption coefficient 50000/cm at wavelength 400 nm, and negligible at wavelength 800 nm. The second set of films was made by drop casting on quartz substrates for OPTP-TDS measurement. The thicknesses of those films were about 15 μm. The third set of films was made by spin-coating on the quartz substrates which have interdigitated switch patterns on them. The thicknesses were controlled to 100-nm. The last set of films was made by drop casting on quartz substrates for photoinduced reflectivity change measurement.

114

MEH-PPV absorption spectrum
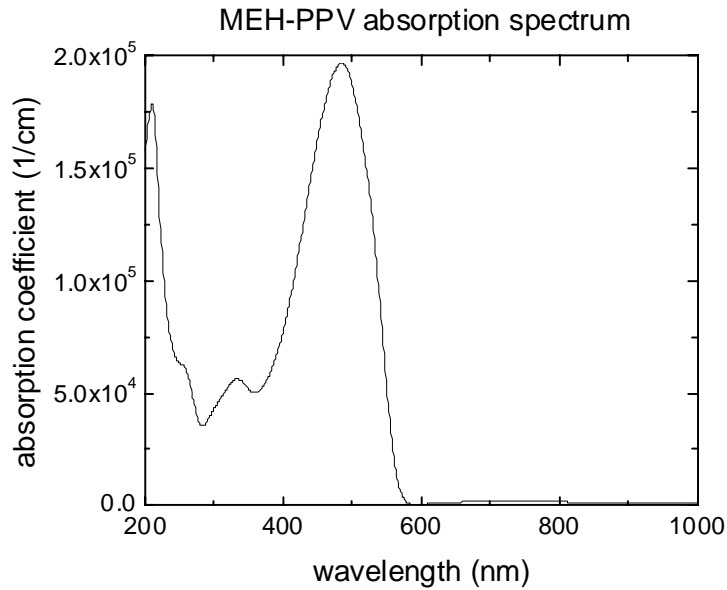
Figure 5-2 Absorption spectrum of MEH-PPV

5.2.2 Optical pump- THz probe time domain spectroscopy

The OPTP-TDS setup is similar to that in chapter 3. The MEH-PPV samples are photoexcited with 400 nm, 100 fs pulses. The pumping energy is 200 μ J/pulse, and the fluence is 2×10^{19} photons/m^2. The photoinduced modulations in the field transmitted through the sample $\Delta E(t)$ at different probe delay times are directly measured in the time domain, as shown in Figure 5-3. At all time delays the modulation depth is less than 1% of the THz probe field. The transient photo-conductivity are obtained by applying correction transformations. The details of data treatment, analysis, and correction are described in chapter 3.
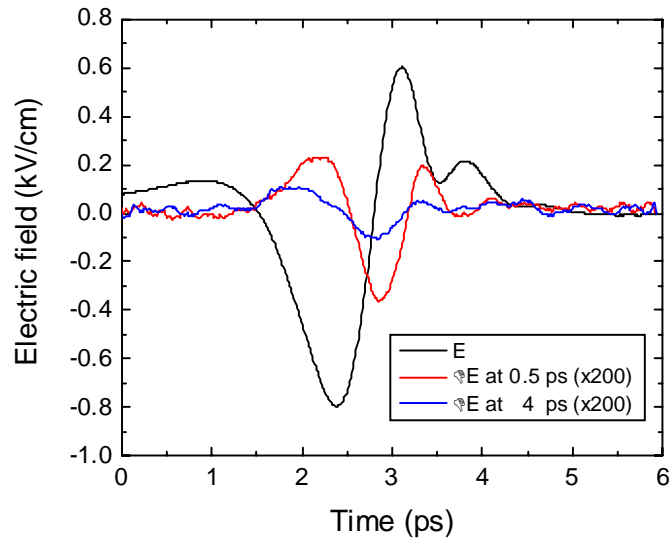
Figure 5-3 The electric field E(t) of the THz pulse transmitted through the MEH-PPV sample (black line), with the modulation ∆E(t) measured 0.5 (red line) and 4 ps (blue line) after photoexcitation

5.2.3 DC-bias transient photoconductivity measurement

A photoconductive switch was fabricated on a fused quartz substrate using photolithography to pattern the interdigitated electrodes, as reported elsewhere [68]. The MEH-PPV polymer solution was spin-coated on top of the metal electrodes to form the active layer. The interdigitated Metal-Polymer-Metal (MPM) switch structure (13 line-pair) was positioned in the center of a co-planar transmission line and illuminated with two equal intensity 400 nm 100 fs laser pulses that were overlapped in space. The structure of the MEH-PPV switch is shown in Figure 5-4.

Using just one 400 nm laser beam, the transient photoconductive signal was measured with a Tektronics sampling oscilloscope. The MEH-PPV film thickness was ~100 nm, the electrode finger gap was 1μm and the external bias field was kept at a fixed

value of 25V/μm. The time varying photo-conductance $G_{PCS}(t)$ can be calculated from the oscilloscope voltage traces using [68]

$$G_{PCS}(t) = \frac{V_{OSC}(t)}{50\Omega[V_{DC} + V_{OFF} - 2V_{OSC}(t)]}$$

(5. 1)

where $V_{osc}(t)$ is the measured time-varying voltage from the oscilloscope, V_{DC} is the bias voltage on the MEH-PPV photoconductive device, and V_{OFF} is the leakage voltage on the oscilloscope before the arrival of the laser pulse. The peak conductance was limited by the resolution of the sampling oscilloscope in this case.

(a)   (b)
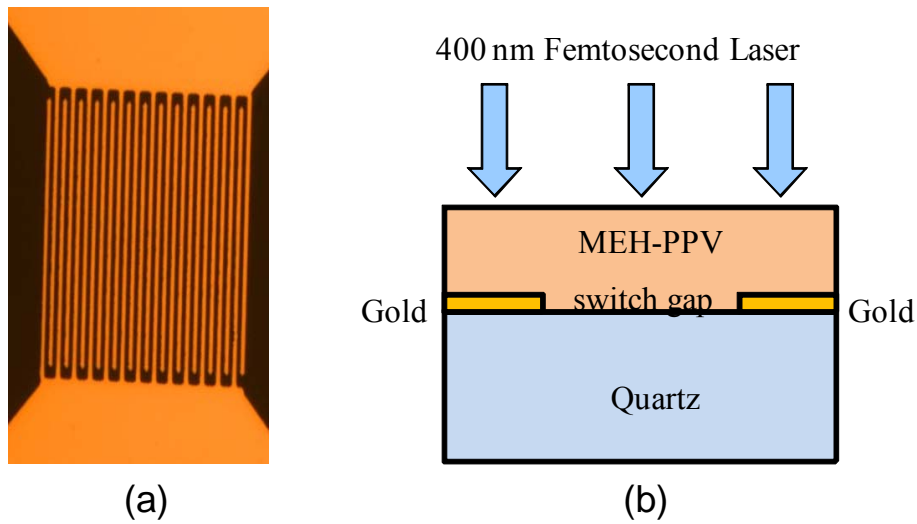
Figure 5-4 (a) Top view of the interdigitated MEH-PPV switch; (b) Schematic of the MEH-PPV switch

117
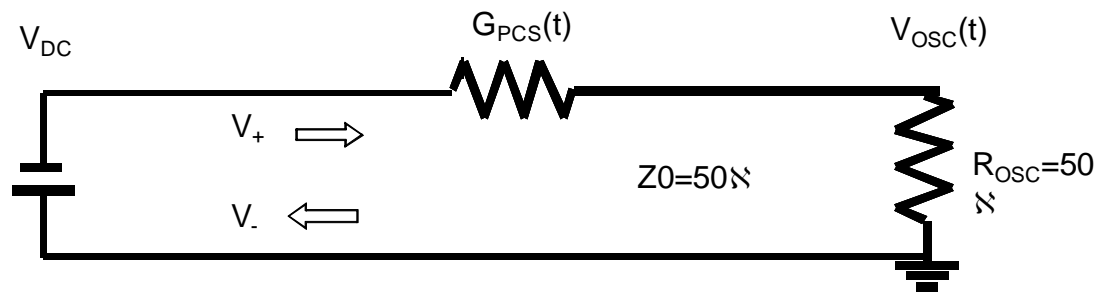
$$G_{PCS}(t) = \frac{V_{OSC}(t)}{50\Omega * [V_{DC} + V_{OFF} - 2V_{OSC}(t)]}$$

Figure 5-5 The electric circuit of the measurement

5.2.4 Photo-induced reflectivity change measurement

To probe the optically induced change of the dielectric property of the MEH-PPV film, the photo-induced change in reflectivity, $\Delta R/R$, in the film was measured using a two wavelength pump-probe laser system. The system setup is shown in Figure 5-6. The 400 nm pump laser beam (MEH-PPV film absorption coefficient $\alpha=0.2$ μm^{-1}) was modulated with a chopper at 5 kHz. In addition, a vibrating retro-reflector oscillating at 3 Hz was used in the 800 nm probe beam to vary the time delay with respect to the pump laser beam. This double modulation plus boxcar time gating provides a sensitivity of 10^{-7} in $\Delta R/R$.
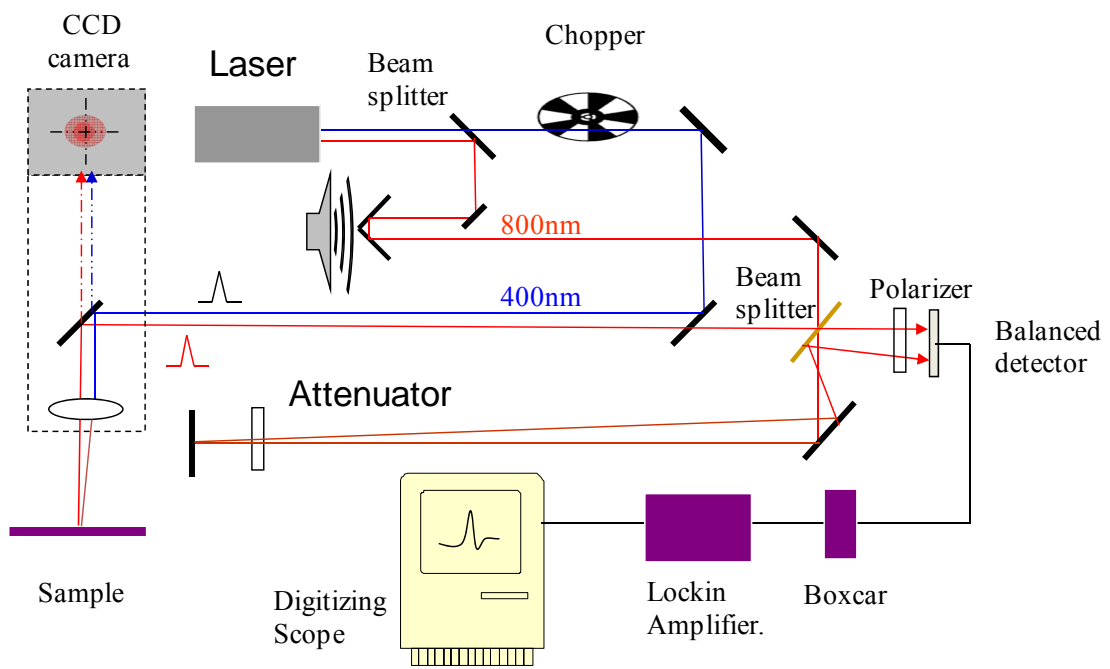
Figure 5-6 The experiment setup of the photoinduced reflectivity change measurement

5.3 Analytic methods

5.3.1 Carrier models

There are two kinds of carriers in a medium: free carriers and bound carriers. The dynamic of simple free carriers can be described by the Drude model, which we have discussed in the section 2.3.2.3. The dynamics of bound carriers can be described by a Lorentzian oscillation model. In the case of free carriers in disordered conductors, Smith [75] introduced a generalized Drude formula to describe the free carrier dynamics in this situation. In this section, first we will discuss the Drude-Smith model for the localized free carriers. Then the Lorentzian oscillation model will be discussed for the bound carriers.

5.3.1.1 Drude-Smith model

To describe the carriers in the semiconducting polymer which has strong carrier localization due to nanoscale inhomogeneity and disorder, we use the Drude-Smith model [75]:

$$\sigma_{DSM}(\omega) = \frac{Ne^2\tau/m^*}{1-i\tau\omega}\left[1+\frac{c}{1-i\tau\omega}\right] \quad , \tag{5.2}$$

where N is the carrier density, τ is the scattering time, m^* is the effective mass. Details of the Drude-Smith model are discussed in chapter 4. The coefficient c represents that fraction of the charge carrier's original velocity that is retained after the first collision. Unlike the simple Drude model, it has a memory or persistence of velocity effect after the scattering. The truncated single-scattering approximation suggested by Smith has well described the semimetals near the metal-insulator transition, such as liquid mercury [75]. See section 4.3.1 for a detail derivation of the Drude-Smith model.

5.3.1.2 Lorentzian oscillation model

A simple bound carrier is an electron-hole pair. When the external electric field applied to the dipole, it will be forced to oscillate by the driving force exerted on the electron. Here we assume that the mass of the hole is much larger than the mass of the electron, so that we can ignore the motion of the hole. The displacement x of the electron is governed by an equation of motion of the form [73]:

$$m_0 \frac{d^2 x}{dt^2} + m_0 \gamma \frac{dx}{dt} + m_0 \omega_0^2 x = -eE \quad , \tag{5.3}$$

where γ is the damping rate, e is the magnitude of the electric charge of the electron, ω_0 is the resonant frequency of the dipole, and E is the external electric field. The terms on the left had side represent the acceleration, the damping, and the restoring force

respectively. We assume the damping force is a frictional force which is proportional to the velocity.

We consider the external electric field is a monochromatic wave with amplitude E_0 and frequency ω. The solution of the equation (5. 3) is

$$x(t) = X_0 \exp(-i\omega t) \quad,$$

(5. 4)

where

$$X_0 = \frac{-eE_0/m_0}{\omega_0^2 - \omega^2 - i\gamma\omega} \quad.$$

(5. 5)

A time varying dipole moment, $p(t)$, is formed from the movement of the electron. The polarization density (P) is given by

$$\begin{aligned}
P &= Np \\
&= -Nex \\
&= \frac{Ne^2}{m_0} \frac{E_0}{\omega_0^2 - \omega^2 - i\gamma\omega} \quad.
\end{aligned}$$

(5. 6)

Therefore, the frequency dependent relative dielectric constant is

$$\varepsilon(\omega) = \varepsilon_{background} + \frac{Ne^2}{\varepsilon_0 m_0} \frac{1}{\omega_0^2 - \omega^2 - i\gamma\omega} \quad.$$

(5. 7)

Using $\varepsilon = \varepsilon_{background} + i\sigma/(\omega\varepsilon_0)$, the frequency response of the dipole in conductivity is

$$\sigma(\omega) = \frac{-i\varepsilon_0 \dfrac{Ne^2}{\varepsilon_0 m_0}\omega}{\omega_0^2 - \omega^2 - i\gamma\omega}$$

$$= \frac{-i\varepsilon_0 G\omega}{\omega_0^2 - \omega^2 - i\gamma\omega} \quad , \tag{5.8}$$

where $G = Ne^2/\varepsilon_0 m_0$ is the strength of the oscillator. Figure 5-7 shows the real and imaginary parts of the conductivity resulting from a typical Lorentzian oscillation.
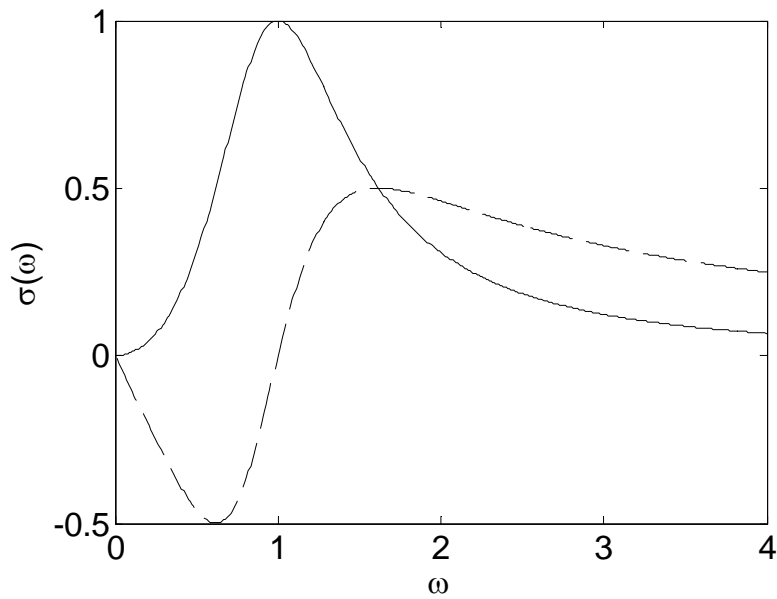
Figure 5-7 The real and imaginary part of conductivity resulting from a typical Lorentzian oscillation

5.3.2 DC-biased transient photoconductivity analysis

Ultrafast DC-biased transient photoconductivity (TPC) leads to the propagation of a low frequency (compared to optical frequency) electromagnetic wave (voltage or current) through the semiconducting polymer containing photocarriers as shown in Figure 5-8. This has been referred to as the conductive mode of operation [71][72]. The electromagnetic pump wave (including DC signal) enters the layer of photocarriers and will be reflected, absorbed and transmitted. In order to investigate the effect of the photocarriers on the propagation of the electromagnetic field, we use the Drude-Smith model for free photocarriers in the disordered medium and the Lorentz model for bond carriers. Generally, the dielectric response is described by the following relationship, independent of the functional form of the conductivity:

$$\varepsilon = \varepsilon_\infty + \frac{i}{\varepsilon_0 \omega} \sigma \quad .$$

(5. 9)

The conductivity is contributed by free and bound carriers:

$$\sigma = \sigma_f + \sigma_b \quad ,$$

(5. 10)

where

$$\sigma_f(\omega) = \frac{\varepsilon_0 \omega_p^2 \tau}{(1 - i\omega\tau)} \left(1 + \frac{c}{(1 - i\omega\tau)} \right) \quad , \tag{5.11}$$

$$\sigma_b(\omega) = \frac{-i\varepsilon_0 G\omega}{\omega_0^2 - \omega^2 - i\gamma\omega} \quad , \tag{5.12}$$

where ε is the complex dielectric constant, ε_∞ is the dielectric constant of the host lattice of the polymer; σ is the complex photoconductivity; ω is the frequency of the propagating wave; σ_f and σ_b are the photoconductivity induced by free and bound photocarriers respectively; ε_0 is the permittivity of free space; τ is the average scattering time of the free photocarriers and ω_p is the plasma frequency of the photocarrier given by

$$\omega_p^2 = Ne^2 / (\varepsilon_0 m^*) \quad , \tag{5.13}$$

where N is the free photocarrier density; m^* is the effective mass of the free photocarriers and e is the electron charge; ω_0, G and γ are the resonant frequency, oscillator strength and spectral width for the bond photocarriers respectively.

When the frequency ω of the electromagnetic wave is much lower than $1/\tau$ and ω_0, we have:

$$\sigma = \varepsilon_0 \omega_p^2 \tau (1 + c) = \frac{Ne^2\tau}{m^*}(1 + c) = Ne\mu \quad , \tag{5.14}$$

125

where μ is the free photocarrier mobility. Equation (5. 14) is the standard expression for photoconductivity which can be measured directly using DC-biased TPC measurement [71].
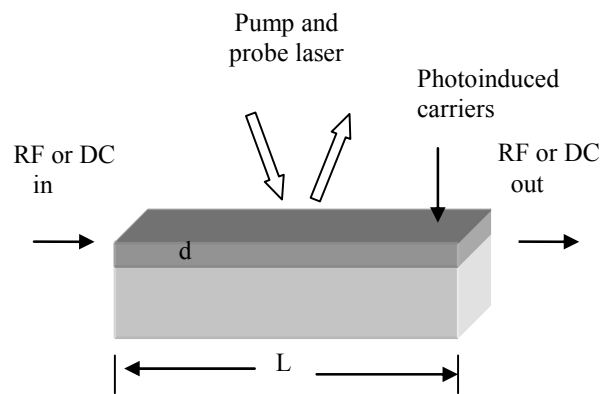
Figure 5-8 Interaction of electromagnetic waves with photocarriers in a semiconducting polymer.

5.3.3 Reflectivity analysis

When an optical wave is used to probe the material, the frequency ω of the electromagnetic wave is much higher than $1/\tau$ and ω_0, we have

$$\sigma = i\frac{\varepsilon_0}{\omega}(\omega_p^2 + G),$$

(5. 15)

and

$$\varepsilon = \varepsilon_\infty - \frac{\omega_p^2 + G}{\omega^2} = n_0^2 + \Delta(n^2)$$

(5. 16)

where n_0 is the refractive index of the polymer at the frequency ω of the optical wave, which can be easily measured. This is referred to as the dielectric mode of interaction [71]. In the absence of photoexcitation, the refractive index is n_0. The change in refractive index upon photoexcitation can be determined by measurements of the photoinduced change in reflectivity. The well-known expression for reflectivity at normal incidence is given by

$$R = \left(\frac{n-1}{n+1}\right)^2$$

(5. 17)

So calculating the relative change in reflectivity and using $\Delta(n^2)$ from Equation (5. 16) gives

$$\frac{\Delta R}{R} = -\frac{2}{n_0(n_0^2-1)} \cdot \frac{\omega_p^2+G}{\omega^2},$$

(5. 18)

which can be measured in the experiment of photo-induced change in reflectivity.

5.4 Results and discussion

From OPTP-TDS measurement, time-resolved photo-conductivities of MEH-PPV in the THz region are obtained. Figure 5-9 shows the 2D real and imaginary time-resolved conductivity spectra contour plots of MEH-PPV before and after applying correction transformations. The correction transformations convert *measured* conductivity to *true* conductivities in OPTP-TDS measurement. For the details of the data analysis, see Chapter 3.
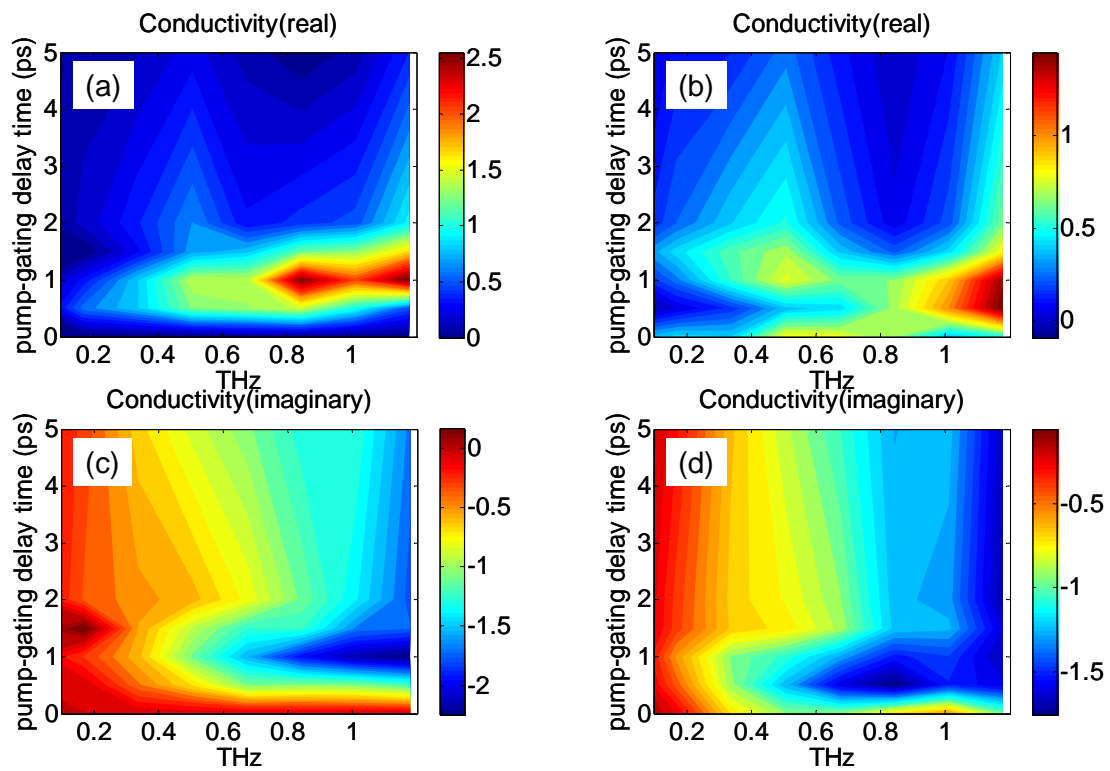
Figure 5-9 2-D real and imaginary time-resolved conductivity spectra contour plots of MEH-PPV before (a, c) and after (c, d) correction transformations.
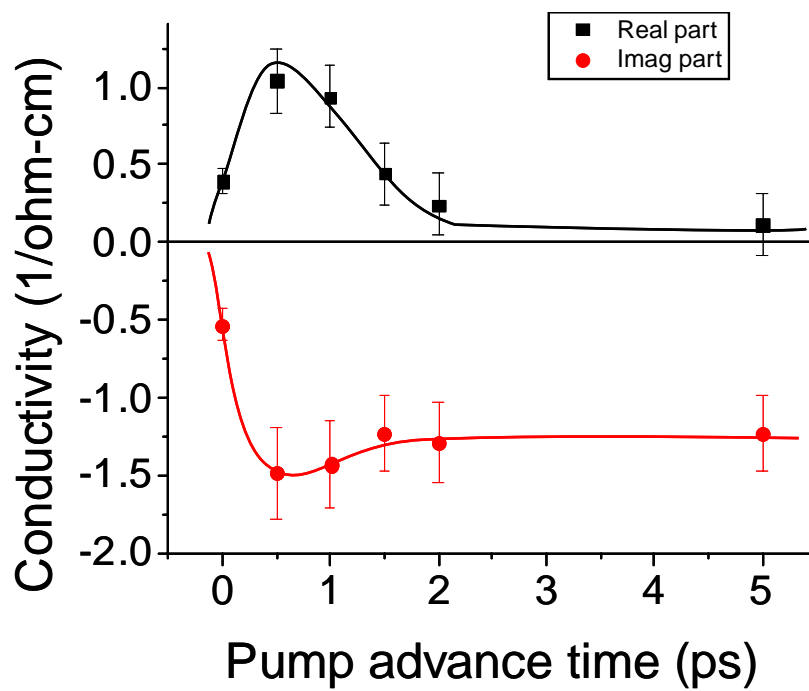
Figure 5-10 Dynamics of the real part and imaginary part of photo-conductivities of MEH-PPV at frequency 1 THz. The lines through the data points are to guide the eye.

Figure 5-10 shows the dynamics of the real and imaginary part of the photo-conductivity of MEH-PPV at a frequency 1 THz. The results show that the real conductivities rise and decay in the first picosecond after photoexcitation. After 2 ps, the real conductivity drops to almost zero. On the other hand, the magnitude of the imaginary part of the conductivity rises in a sub-picosecond time scale and sustains for a longer time.

Figure 5-11 shows the real and imaginary part of conductivities extracted for the MEH-PPV sample, measured at 1 and 5 ps after photoexcitation. The 1 ps conductivities show non-Drude behavior in that the real part of the conductivity rises with frequency, and the negative imaginary conductivity decreasing with frequency. The 5 ps conductivities show the same negative imaginary conductivity decreasing with frequency but near zero real conductivity. The non-Drude behavior is characteristic of free charge transport in a disordered medium, where localization is caused by the disorder in the material structure. We would like to use a model combining the Drude-Smith model and the Lorentz oscillator model to describe MEH-PPV, which has short lived real conductivity for free carriers, and relative long lived imaginary conductivity for the bound carriers. Some may wonder why not use the simple Drude model instead of the Drude-Smith model. Indeed, we have tried to use just the simple Drude model and the Lorentzian model instead of the Drude-Smith model to describe the phenomenon that the real conductivity increase with frequencies in the first picosecond by setting the resonance frequency of the Lorentz oscillator very close to 1 THz. Although it can give similar fitting results in the 1 ps data, however, this model cannot explain the near zero real conductivity in the later time when no free charge carriers exist.

In order to get a good data fit using the Drude-Smith and Lorentzian model, DC-biased transient photoconductivity measurement and a transient optical reflectivity change experiment are performed to get the DC conductivity and high frequency optical conductivity.
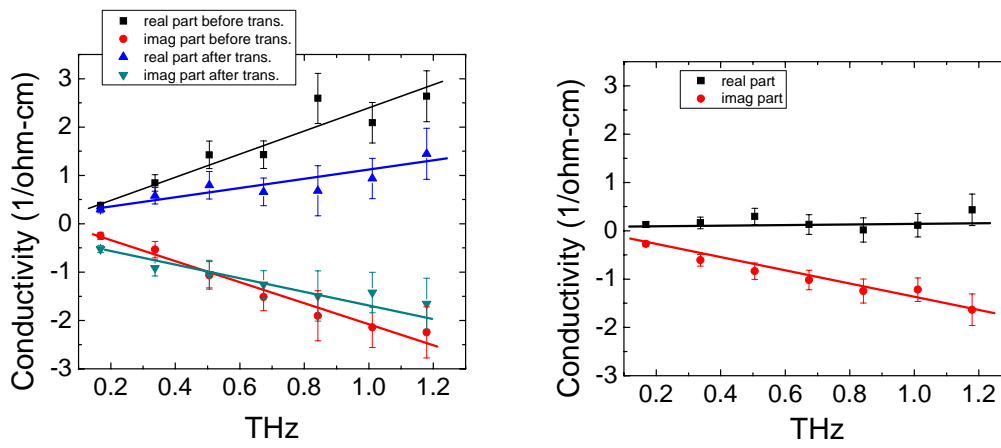
Figure 5-11 (a) Complex conductivities before and after the correction transformation for photoexcited MEH-PPV sample measured at 1 ps. (b) Complex conductivities at 5 ps after photoexcitation. The lines through the data points are to guide the eye.

DC-biased transient photoconductivity is measured using a photo-conductive switch. Because the measured response time is limited by the capacitance of the switch, to acquire the true carrier response time it is essential to obtain the transient DC photoconductivity. To measure the carrier lifetime, two pulsed 400 nm laser beams were used to pump the switch. At this time a chopper was used to modulate both beams and a vibrating mirror at 3 Hz was used in one beam to vary the time delay with respect to the other beam. The photoconductive signal was first sent to a boxcar averager and then a

lock-in amplifier. Finally a digitizing oscilloscope, synchronized with the vibrating mirror, was employed to scan and average the photoconductive signal from the lock-in amplifier. Because of identical modulation, the photoconductive signal from the lock-in amplifier is the sum of signals induced by each beam whether they are overlapped in time or not. When the two beams were separated in time, the voltage across the photoconductive switch prior to the arrival of each laser pulse was the same. When the two laser pulses partially overlapped, the leading pulse experienced higher bias voltage than the delayed one because the photocurrent caused by the leading pulse reduced the bias voltage for the delayed pulse. This led to a sum signal that was less than that for the two pulses separated and resulted in a "dip" in the induced photocurrent as shown in Figure 5-12. This time varying behavior represents the carrier lifetime. The autocorrelation full width at half maximum is 1.8 ps and consequently a carrier lifetime of 0.9 ps is obtained if a Lorentz pulse shape is assumed. This number is consistent with the real conductivity decay time in the OPTP-TDS measurement. The time resolution was limited by the capacitance of the switch, which was measured to be 20 fF. The transient conductance G_{osc} measured by the scope is then multiplied by a factor equal to the ratio of the scope pulse width to the pulse width of the photoconductive sampling signal, a factor of 25 in this case. That is, $G_{peak}=25G_{osc}$.

The peak photoconductivity σ can be obtained from

$$\sigma = \frac{G_{peak}L}{A}$$

(5. 19)

133

where A ,the cross section of the switch, is equal to $50 \times 25 \times 0.1 = 125 \mu m^2$ (finger length 50 μm, 13 pairs of fingers, 0.1 μm thick film), and $L=1$ μm is the width of the finger gap. The signal waveforms of the MEH-PPV film at various pump levels are presented in Figure 5-13. At the fluence level 2×10^{19} photons/m^2, a photoconductivity of 0.28/Ω-cm was achieved.
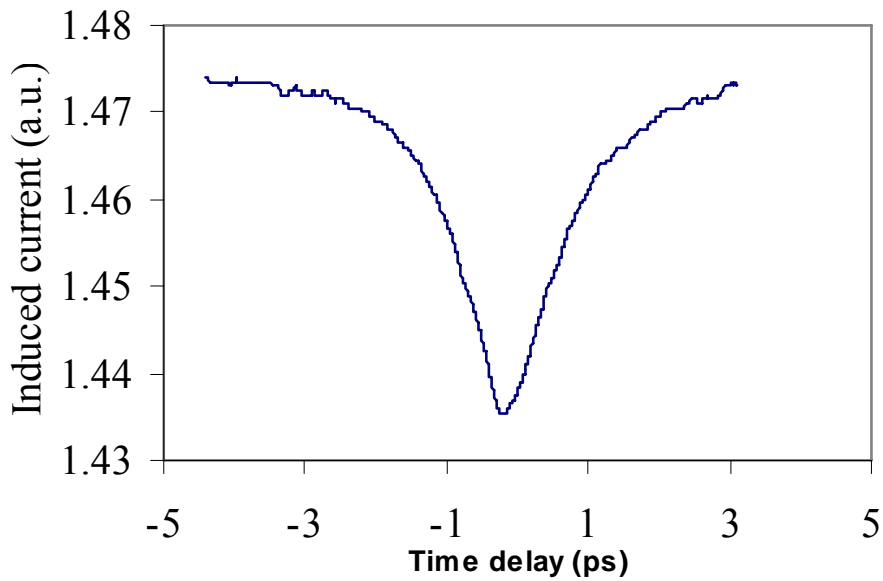
Figure 5-12 Photoconductive signal vs. time delay
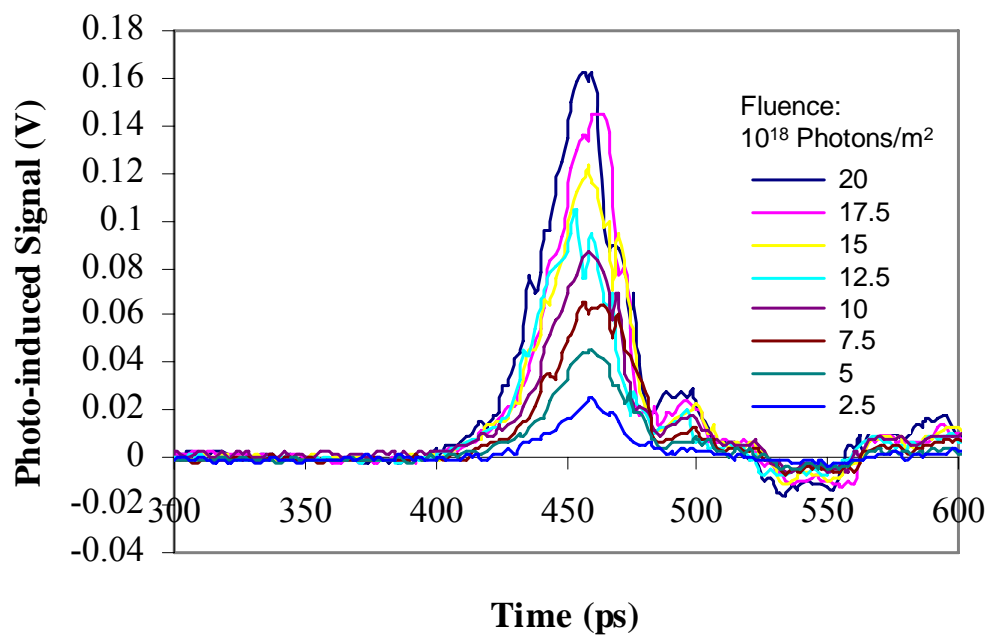
Figure 5-13 Photoconductive signal at various pumping energy measured by a 50 GHz sampling oscilloscope

The time dependent reflectivity change of MEH-PPV at 800 nm was measured by 400 nm pump- 800 nm probe reflectivity change measurement. The typical probe time delay dependence of the change in reflectivity is presented in Figure 5-14. The result shows a 270 fs leading edge and a 500 fs fast decay followed by a tail extending for hundreds of picoseconds. We will discuss this fast respond in the later paragraph. At the fluence level 2×10^{19} photons/m^2, a photo-induced change of -4×10^{-4} in reflectivity at wavelength of 800 nm was obtained.
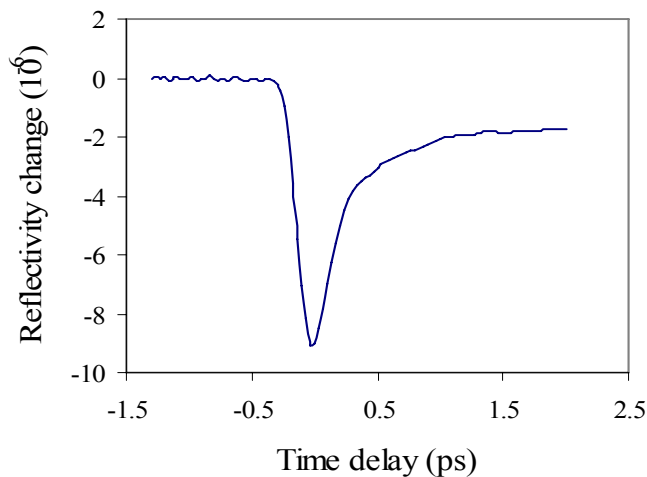
Figure 5-14 Photo-induced change in reflectivity vs. probe delay time. The fluence of the reflectivity measurement is 1×10^{17} photons/m^2, which is 1/200 of the fluence of THz measurement, 2×10^{19} photons/m^2

Now we can try to fit our experimental data with the Drude-Smith model and the Lorentz oscillator model. Hendry and co-workers [48] measured the transient conductivity of photo-excited MEH-PPV and got similar results. They concluded that the

long life response of the imaginary part of the conductivity is due to bound carriers, and the short life response of real conductivity is due to free carriers. Following this conclusion, we use the Drude-Smith model to describe the free carriers and Lorentz oscillator model to describe the bound carriers. First we consider the conductivity at 5 ps after photoexcitation when there are no free carriers and only excitons. The binding energy of the exciton in MEH-PPV is about 0.2 [74] to 0.8 [76] eV. We assume the binding energy is 0.2 eV, so the resonant frequency (f) of the oscillator is 50 THz. Figure 5-15 (b) shows the fitting result with parameter G= 2.6×10^{29}, $\gamma = 2\pi \times 1$ THz, $\omega_0 = 2\pi \times 50$ THz. With the determined Lorentz oscillator, we fit the conductivity at 1 ps after photoexcitation with the Drude-Smith model and the Lorentz oscillator, as shown in Figure 5-15 (a), the parameters for Drude-Smith model are ω_p=15 THz, τ =0.1 ps, and c=-0.87. By assuming the effective mass equal to the electron mass, we find that the quantum efficiency of free carriers is about 10^{-3} using $N = \varepsilon_0 m^* \omega_p^2 / e^2$, and that the mobility is about 23 cm^2/Vs using equation $\mu = e\tau(1+c)/m^*$. We can also estimate the quantum efficiency of the excitons by substituting the parameter G into the equation $G = Ne^2 / \varepsilon_0 m_0$, and get the quantum efficiency of exciton is about 1. So far, the results look reasonable. However, when we use these models to predict the reflectivity change at 800 nm, we get disagreement with the experimental data.
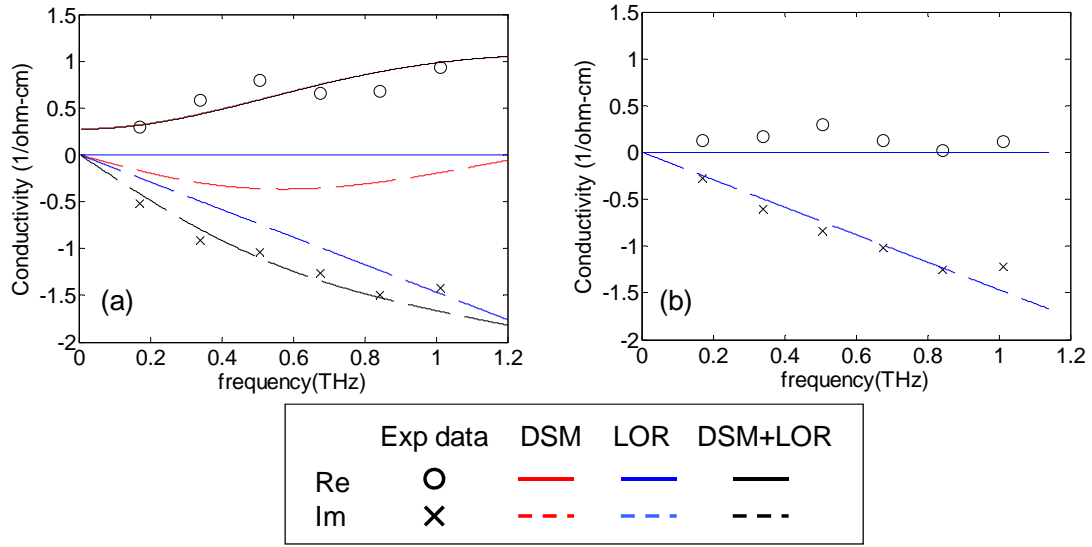
Figure 5-15 (a) Conductivity at 1 ps after photoexcitation. The data are fit with the Drude-Smith model plus Lorentzian model. (b) Conductivity at 5 ps after photoexcitation. The data are fit with the Lorentzian model. The resonant frequency of the Lorentz oscillator is 50 THz.

Using equation (5. 18) , we can estimate the reflectivity change at 800 nm, $\Delta R/R = -3.8 \times 10^{-2}$. The number is 2 orders higher than -4×10^{-4} obtained from the optical pump-probe experiment. This result suggests that the exciton density should be at least 2 orders lower, and that implies that the quantum efficiency of excitons is equal to or less than 0.01. The imaginary conductivity at THz frequencies from the excitons will be much lower than we previously throught, and there should be additional Lorentz oscillator(s) to describe the imaginary conductivity measured in the THz region. In order to fit all the experiment data, we change the resonant frequency from 50 THz to 5 THz, and the oscillator strength becomes G=2.6×10^{27} . These bound carriers have very low energy (0.02 eV) and probably are photo-induced phonons (Infrared active vibrational modes [87][88]).
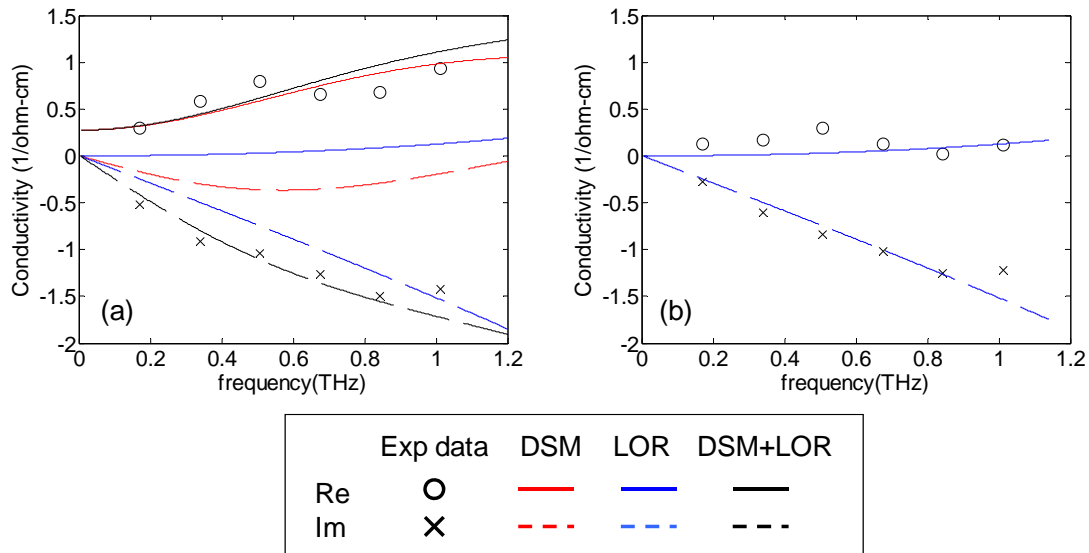
Figure 5-16 Conductivity at 1 ps after photoexcitation. The data are fit with Drude-Smith model plus Lorentzian model. (b) Conductivity at 5 ps after photoexcitation. The data are fit with Lorentzian model. The resonant frequency of the Lorentz oscillator is 5 THz.

In the time-resolved reflectivity change measurement, we observed s very fast rise and decay in the first picosecond after photoexcitation. Although we have similar dynamics measured in transient THz photo-conductivity OPTP-TDS experiment, they may not measure the same phenomenon due to the difference in probing frequency. The reflectivity change contributed by the free carriers in the optical region is negligible compared to the contribution by the bound carriers in this case. The fast rise and decay in the reflectivity change measurement could be due to the dynamics of the exciton density.

5.4.1 Comparison of P3HT and MEH-PPV

We compare the measurement results of MEH-PPV with the previous measurement results of P3HT. The first observation is that P3HT is more resistant than MEH-PPV to photo-oxidation. Figure 5-17 shows the decays of transmitted THz peak amplitude for P3HT and MEH-PPV by pumping continuously with 400-nm pulses. Both materials have similar absorption coefficients at 400-nm, and are pumped with the same fluence. The results show that the decay rate of MEH-PPV is at least three times faster than that of P3HT. The stability of P3HT makes it more suitable for many practical applications.

Photon-to-carrier quantum efficiencies for P3HT and MEH-PPV under the same pumping fluence are 1 % and 0.1%, respectively. When the neat polymers are pumped (time < 1 ps), both exhibit similar real photo-conductivity peaks. However, for the longer times after photoexcitation (e.g., 10 ps), the real conductivity of the MEH-PPV sample decays to almost zero, while the P3HT sample still has considerable real conductivity. It can be explained by the morphology of the films [84]. Regio-regular P3HT has a high degree of intrachain order, and will self-order to form microcrystalline regions of π-stacked lamella with strong interchain interactions [85]. The close proximity of neighboring chains allows the electron and hole charges to escape on separate chains, thus minimizing the subsequent recombination [86]. Because P3HT has greater interchain interaction than MEH-PPV, a longer free carrier lifetime in P3HT is expected.
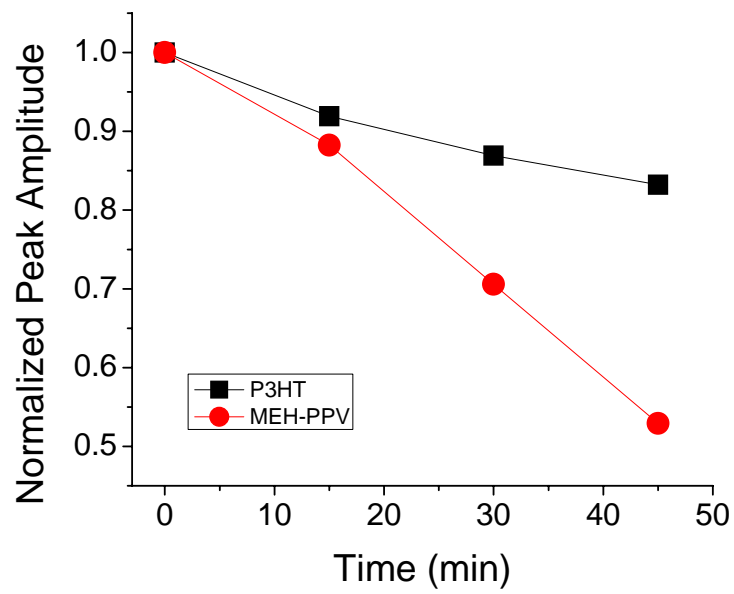
Figure 5-17 Decays of transmitted THz peak amplitude for P3HT and MEH-PPV

5.5 Conclusions

Both conductive and dielectric properties of photo-excited MEH-PPV thin films are reported in this chapter. Photoconductivity dynamics in MEH-PPV was measured under DC bias, and at THz and optical wavelengths with a high time resolution. A free photocarrier quantum efficiency of 10^{-3} was obtained for 400 nm, 110 fs pump laser pulses. A transient photocarrier mobility up to 23 cm^2/Vs was estimated. The quantum efficiency of excitons was estimated to be less than 0.01. Fast response of free carriers was observed in both photoconductivity switch and OPTP-TDS experiments, and fast response of bound carriers was observed in the reflectivity change experiment. All measurements at different wavelengths verified that the fast part of the photocarrier lifetime in MEH-PPV is less than 1ps.

Chapter 6: Conclusion

6.1 Summary

In this thesis, we establish standard experimental and analysis procedures for optical pump- THz probe time domain spectroscopy for investigating the transient events that are faster than the duration of THz probe pulses. The new procedures are made by modifying the conventional analysis method proposed by Kindt and Schmuttenmaer using Nienhuys and Sundstrom's theoretical analysis of OPTP-TDS. We observed artifacts in the conductivity of photoexcited GaAs when we apply the conventional analysis method to the experiment data. The artificial effect can be well described by the Nienhuys and Sundstrom's theoretical analysis. We, for the first time, successfully remove the artifacts and obtain the true transient conductivity of photoexcited GaAs using the correction transformation suggested by Nienhuys and Sundstrom.

P3HT/PCBM blends with P3HT weight fractions of 1, 0.8, 0.5, 0.2, and 0 were investigated using OPTP-TDS. The new analysis process was used to obtain the time resolved frequency dependent complex photoconductivity at subpicosecond resolution. The time resolved conductivity is analyzed by the Drude-Smith model to describe the behavior of localized charge carriers in the polymer. The free charge carrier quantum efficiency is about 1% in P3HT/PCBM blends. The result that the 1:1 blend film shows the highest conductivity among other blends is consistent with independent photovoltaic measurements. The significant drop of real conductivity in the first picosecond after photoexcitation for P3HT/PCBM blends can be attributed to the transient mobility change

due to polaron formation on a sub-picosecond time scale. We also measure the long term (up to 300 ps) conductivity of the polymers and find that the difference of the free carrier life time of neat P3HT, P3HT/PCBM blends, and neat MEH-PPV can be explained by interchain interaction of charge carriers.

The semiconducting polymer MEH-PPV is investigated using OPTP-TDS, a DC-bias transient photoconductivity experiment, and a photo-induced reflectivity change measurement with high time resolution to get the transient conductivities at DC, THz, and optical frequencies. The data are fitted using the Drude-Smith model and the Lorentzian oscillation model. The results show that the free photocarrier quantum efficiency is about 10^{-3} for 400 nm photoexcitation. Transient photocarrier mobility up to 23 cm^2/Vs was estimated. The quantum efficiency of excitons was estimated to be less than 0.01, which is lower than we thought earlier. The imaginary part of the conductivity at THz frequencies is attributed not to excitons but to the bound carriers with one tenth the energy of excitons, which are possibly phonons.

6.2 Future work

In section 4.4.1 we discussed the disagreement of free carrier quantum efficiencies obtained from OPTP-TDS and solar cell measurements. For P3HT/PCBM blends, the efficiencies we observed in OPTP-TDS are about 1~2%, while the efficiencies measured in the polymer solar cells approach 1. The possible reason for the disagreement is the built-in potential. The electrodes in the polymer solar cells provide the built-in electric field due to the difference of the work functions of the electrodes. This field can be 2 orders of magnitude higher than the electric field of the THz probe in OPTP-TDS. Based on this point of view, it would be interesting to perform the OPTP-TDS measurement on a high voltage biased semiconducting polymer sample. It would be similar to photoconductive switch experiment, but we would measure the transmitted THz field instead of the photoinduced current. The sample can be prepared by drop casting a semiconducting polymer solution on a quartz plate that has coplanar electrodes patterned on it. The photoconductivities of the polymer in the biased state and in the unbiased state could be measured easily in an OPTP-TDS experiment. This experiment could give us an idea on how the electric field affects the free carrier generation.

Bibliography

[1] A. Rice, Y. Jin, X. F. Ma, X. –C. Zhang, D. Bliss, J. Larkin, M. Alexander, "Terahertz optical rectification from <110> zinc-blende crystals", Appl. Phys. Lett. Vol 64, p1324, 1994

[2] Ch. Fattinger and D. Grischkowsky, "Terahertz beams", Appl. Phys. Lett., Vol 54, p490, 1989

[3] Kodo Kawase, Jun-ichi Shikata and Hiromasa Ito, " Terahertz wave paramertric source", J. Phys. D: Appl. Phys., Vol 35, R1, 2002

[4] X. –C. Zhang and D. H. Auston, "optoelectronic measurement of semiconductor surface and interfaces with femtoseconds optics", J. Appl. Phys., Vol 71, p326, 1996

[5] Q. Wu and X.-C. Zhang, "Free-space electro-optic sampling of terahertz beams", Appl. Phys. Lett., Vol 67, p3523, 1995

[6] E. L. Dereniak and G. D. Boreman, "*Infrared detectors and systems*", John Wiley & Sons, New York, 1996

[7] Ajay Nahata, Aniruddha S. Weling, and Tony F. Heinz, "A wideband coherent terahertz spectroscopy system using optical rectification and electro-optic sampling", Appl. Phys. Lett., Vol 69, p2321, 1996

[8] J. B. Gunn, "Microwave oscillations of current in III-V semiconductors", Solid State Commun., Vol 1, No 4, p88, 1963

[9] C. Walther, G. Scalari, J. Faist, H. Beere, and D. Ritchie, "Low frequency terahertz quantum cascade laser operating from 1.6 to 1.8 THz", Appl. Phys. Lett. Vol 89, No 23, p231121, 2006

146

[10] K. A. Mclntosh, E. R. Brown, K. B. Nichols, O. B. McMahon, W. F. DiNatale, and T. M. Lyszczarz, "Terahertz photomixing with diode lasers in low-temperature-grown GaAs", Appl. Phys. Lett., Vol 67, p3844, 1995

[11] G. Winnewisser, "Spectroscopy in the terahertz region", Vibrational Spectroscopy, Vol 8, p241, 1995

[12] G. L. Carr, Michael C. Martin, Wayne R. McKinney, K. Jordan, George R. Neil, and G. P. Williams, "High-power terahertz radiation from relativistic electrons", Nature, Vol 420, p153, 2002

[13] T. Yasui, A. Nishimura, T. Suzuki, K. Nakayama, S. Okajima, "Detection system operating at up to 7 THz using quasioptics and Schottky barrier diodes", Review of Scientific Instrumnets, Vol 77, p066102, 2006

[14] W. Knap, Y. Deng, S. Rumyantsev, and M. S. Shur, "Resonant detection of subterahertz and terahertz radiation by plasma waves in submicron field-effect transistors", Appl. Phys. Lett., Vol 81, p4637, 2002

[15] Nadya Anscombe, "No place to hide", IEE Rev., p26, 2005

[16] Kodo Kawase, "Terahertz imaging for drug detection & large-scale integrated circuit inspection", Optics & Photonics news, p34, October 2004

[17] Vincent P. Wallace, "Terahertz methods show promise for breast cancer", Laser Focus World, p83, June 2006

[18] David Zimdars, J. A Valdmanis, Jeffery S. White, G. Stuk, S. Williamson, William P. Winfree, and Eric I. Madaras, "Technology and applications of terahertz imaging non-destructive examination: inspection of space shuttle sprayed on foam insulation", Rev. of Quantitative Nondestructive Evaluation, Vol 24, p570, 2005

[19] N. Karpowicz, Hua Zhong, Cunlin Zhang, Kuang-I Lin, Jenn-Shyong Hwang, Jingzhou Xu, X. –C. Zhang, "Compact continuous-wave subterahertz system for inspection application", Appl. Phys. Lett., Vol 86, no 5, p54105, 2005

[20] B. B. Hu and M. C. Nuss, "Imaging with terahertz waves", Optics Let., Vol 20, no 16, p1716, 1995

[21] J. H. Burroughes, D. D. C. Bradley, A. R. Brown, R. N. Marks, K. Mackay, R. H. Friend, P. L. Burns, and A. B. Holmes, "Light-emitting diodes based on conjugated polymers", Nature, Vol 347, p539, 1990

[22] Christoph J. Brabec, N. Serdar Sariciftci, and Jan C. Hummelen, "Plastic solar cells", Adv. Func. Mater., Vol 11, p15, 2001

[23] M. Granstrom, K. Petritsch, A. C. Arias, A. Lux, M. R. Andersson, R. H. Friend, "Laminated fabrication of polymeric photovoltaic diodes", Nature, Vol 295, p257, 1998

[24] G. Horowitz, "Organic field-effect transistors", Adv. Mater., Vol 10, p365, 1998

[25] Francis Garnier, Ryad Hajlaoui, Adberrahim Yassar, Pratima Srivastava, "All-polymer field-effect transistor realized by printing techniques", Science, Vol 265, p1684, 1994

[26] Fumitomo Hide, Maria A. Diaz-Garcia, Benjamin J. Schwartz, Mats R. Andersson, Qibin Pei, Alan J. Heeger, "Semiconducting polymers: a new class of solid-state laser materials", Science, Vol 273, p1833, 1996

[27] Marisol Reyes-Reyes, Kyungkon Kim, David L. Carroll, "High-efficiency photovoltaic devices based on annealed poly(3-hexylthiophene) and 1-(3-

methoxycarbonyl)-propyl-1- phenyl-(6,6)C61 blends", Appl. Phys. Lett., Vol 87, p083506, 2005

[28] Jin Young Kim, Kwanghee Lee, Nelson E. Coates, Daniel Moses, Thuc-Quyen Nguyen, Mark Dante, Alan J. Heeger, "Efficient tandem polymer solar cells fabricated by all-solution processing", Science, Vol 317, p222, 2007

[29] H. –K. Nienhuys and V. Sundstrom, "Intrinsic complications in the analysis of optical-pump, terahertz probe experiments", Phys. Rev. B, Vol 71, p235110, 2005

[30] M. V. Exter and D. Grischkowsky, "Optical and electronic properties of doped silicon from 0.1 to 2 THz", Appl. Phys. Lett. 56(17), p1694, 1990

[31] M. Bass, P. A. Franken, J. F. Ward, and G. Weinriech, "Optical rectification", Phys. Rev. Lett., Vol 9, No 11, p446, 1962

[32] Robert W. Boyd, *Nonlinear Optics*, 2nd Edition, Academic Press, 2003

[33] A. Yariv, Quantum Electronics, 3rd Edition, Wiley, 1988

[34] P. C. M. Planken, H.-K. Nienhuys, H. J. Bakker, and T. Wenckebach, "Measurement and calculation of the orientation dependence of terahertz pulse detection in ZnTe", J. Opt. Soc. Am. B, Vol. 18, No. 3, p313, 2001

[35] G. Zhao, R. N. Schouten, N. van der Valk, W. T. Wenckebach, and P. C. M. Planken, "Design and performance of a THz emission and detection setup based on a semi-insulating GaAs emitter", Rev. of Sci. Inst., Vol. 73, No. 4, p1715, 2002

[36] H. J. Bakker, G. C. Cho, H. Kurz, Q. Wu, and X. –C. Zhang, "Distortion of terahertz pulses in electro-optic sampling", J. Opt. Soc. Am. B, Vol. 15, No. 6, p1795, 1998

[37] G. Gallot, and D. Grischkowsky, "Electro-optic detection of terahertz radiation", J. Opt. Soc. Am. B, Vol. 16, No. 8, p1204, 1999

[38] G Gallot, J. Zhang, R. W. McGowan, T. Jeon, and D. Grischkowsky, "Measurement of the THz absorption and dispersion of ZnTe and their relevance to the electro-optic detection of THz radiation", Appl. Phy. Lett., Vol. 74, No. 23, p3450, 1999

[39] M. van Exter, "Terahertz time-domain spectroscopy of water vapor", Optics Lett., Vol. 14, No.20, 1989

[40] M. Born and E. Wolf, *Principles of Optics*, Macmillan, 1964

[41] M. C. Beard, G. M. Turner, and C. A. Schmuttenmaer, "Transient photoconductivity in GaAs as measured by time-resolved terahertz spectroscopy", Phys. Rev. B, Vol 62, No 23, p15764, 2000

[42] G. L. Dakovski, B. Kubera, S. Lan, and J. Shan, "Finite pump-beam-size effects in optical pump-terahertz probe spectroscopy", J. Opt. Soc. Am. B, Vol 23, No 1, p139, 2006

[43] E. Hecht, *Optics*, Addison Wesley, 1998

[44] S. S. Prabhu, S. E. Ralph, M. R. Melloch, and E. S. Harmon, "Carrier dynamics of low-temperature-grown GaAs observed via THz spectroscopy", Appl. Phys. Lett., Vol 70, No 18, p2419, 1997

[45] P. U. Jepsen, W. Schairer, I. H. Libon, U. Lemmer, N. E. Hecker, M. Birkholz, K. Lips, and M. Schall, "Ultrafast carrier trapping in microcrystalline silicon observed in optical pump-terahertz probe measurements", Appl. Phys. Lett., Vol 79, No 9, p1291, 2001

[46] J. T. Kindt and C. A. Schmuttenmaer, "Theory for determination of the low-frequency time-dependent response function in liquids using time-resolved terahertz pulse spectroscopy", J. Chem. Phys., Vol 110, No 17, p8589, 1999

[47] M. C. Beard, G. M. Turner, and C. A. Schmuttenmaer, "Terahertz Spectroscopy", J. Phys. Chem., Vol 106, p7146, 2002

[48] E. Hendry, J. M. Schins, L. P. Candeias, L. D. A. Siebbeles, and M. Bonn, "Efficiency of exciton and charge carrier photogeneration in a semiconducting polymer", Phys. Rev. Lett., Vol 92, No 19, p196601, 2004

[49] X. Ai, M. C. Beard, K. P. Knustsen, S. E. Shaheen, G.Rumbles, and R. J. Ellingson, "Photoinduced charge carrier generation in a poly(3-hexylthiophene) and methanofullerene bulk heterojunction investigated by time-resolved terahertz spectroscopy", J. Phys. Chem. B, Vol 110, No 50, p25462, 2006

[50] P. D. Cunningham and L. M. Hayden, "Carrier dynamics resulting from above and below gap excitation of P3HT and P3HT/PCBM investigated by optical-pump terahertz-probe spectroscopy", J. Phys. Chem. C, Vol 112, No 21, p7928, 2008

[51] S.O. Kasap, "*Principles of Electronic Materials and Devices*", Second Edition, McGrraw-Hill, 2002

[52] M. D. Sturge, "Optical absorption of Gallium Arsenide between 0.6 and 2.75 eV", Phys. Rev., Vol 127, No 3, p768, 1962

[53] A. Yariv and P. Yeh, "*Optical waves in Crystals: Propagation and Control of Laser Radiation*", Wiley, New York, 1984

[54] J. I. Pankove, "*Optical Processes in Semiconductors*", Prentice-Hall, Englewood, NJ, 1971

[55] D. Grischkowsky, S. Keidingm N, M. Exter, and C. Fattinger, "Far-infrared time-domain spectroscopy with terahertz beams of dielectrics and semiconductors", J. Opt. Soc. Am. B, Vol 7, No 10, p2006, 1990

[56] C.K. Chiang, C.R. Fincher Jr., Y.W. Park, A.J. Heeger, H. Shirakawa,E.J. Louis, S.C. Gau, A.G. MacDiarmid, "Electrical conductivity in doped polyacetylene", Phys. Rev. Lett., Vol 39, p1098, 1977

[57] C.W. Tang, S.A. VanSlyke, C.H. Chen, "Electroluminescence of doped organic thin films", J. Appl. Phys., Vol 65, p3610, 1989

[58] R.H. Friend, R.W. Gymer, A.B. Holmes, J.H. Burroughes, R.N. Marks, C. Taliani, D.D.C. Bradley, D.A. Dos Santos, J.L. Bredas, M. Lo¨gdlund, W.R. Salaneck, "Electroluminescence in conjugated polymers", Nature, Vol 397, p121, 1999

[59] G. Yu, J. Gao, J.C. Hummelen, F. Wudl, A.J. Heeger, Science, "Polymer photovoltaic cells: enhanced efficiencies via a network of internal donor-acceptor heterojunctions", Science, Vol 270, p1789, 1995

[60] H. Sirringhaus, N. Tessler, R.H. Friend, "Integrated optoelectronic devices based on conjugated polymers", Science, Vol 280, p1741, 1998

[61] N. Tessler, G.J. Denton, R.H. Friend, "Lasing from conjugated-polymer microcavities", Nature, Vol 382, p695, 1996

[62] F. Hide, B.J. Schwartz, M.A. DiazGarcia, A.J. Heeger, "Laser emission from solution and films containing semiconducting polymer and titanium dioxide nanocrystals", Chem. Phys. Lett., Vol 256, p424, 1996

[63] M. Berggren, A. Dodabalapur, R.E. Slusher, Z. Bao, "Light amplification in organic thin films using cascade energy transfer", Nature, Vol 389, p466, 1997

[64] D. Moses, H. Okumoto, C.H. Lee, A.J. Heeger, "Mechanism of carrier generation in poly(phenylene vinylene): transient photoconductivity and photoluminescence at high electric fields", Phys. Rev. B, Vol 54 p4748, 1996

[65] D.M. Basco, E.M. Conwell, "Hot exciton dissociation in conjugated polymers", Phys. Rev. B, Vol 66, p155210, 2002

[66] C.H. Lee, G. Yu, A.J. Heeger, "Persistent photoconductivity in poly(p-phenylenevinylene): spectral response and slow relaxation", Phys. Rev. B, Vol 47, p15543, 1993

[67] E. Hendry, M. Koeberg, J.M. Schins, L.D.A. Siebbeles, M. Bonn, "Ultrafast charge generation in a semiconducting polymer studied with THz emission spectroscopy", Phys. Rev. B, Vol 70, p033202, 2004

[68] H.Y. Liang, W. L. Cao, M. Du, Y. Kim, W. N. Herman and C. H. Lee, "Ultrafast photo-conductivity in BAMH-PPV polymer thin-films", Chem. Phys. Lett., Vol 419, p292-296, 2006

[69] Daniel Moses, Arthur Dogariu, and Alan J. Heeger, "Ultrafast detection of charged photocarriers in conjugated polymers", Phys. Rev. B, Vol 61, p9373, 2000

[70] H. Scher and S. Rackovsky, "Theory of geminate recombination on a lattice", J. Chem. Phys., Vol 81, p1994, 1984

[71] Chi H. Lee," *Picosecond Optoelectronic Devices*", Academic Press, INC., 1984

[72] F.J. Leonberger, Chi H. Lee, F. Capasso, H. Morkoc, "*Picosecond Electronics and Optoelectronics II*", Springer-Verlag, 1987

[73] Anthony Mark Fox, Mark Fox, *Optical Properties of Solids*, Oxford University Press, 2001

153

[74] Jean-Luc Bredas, Jerome Cornil, and Alan J. Heeger, "The exciton binding energy in luminescent conjugated polymers", Adv. Mater. Vol 8, No. 5, p447, 1996

[75] N. V. Smith, "Classical generalization of the Drude formula for the optical conductivity", Phys. Rev. B, Vol 64, p155106, 2001

[76] J. W. v. d. Horst, P. A. Bobbert, P. H. L. d. Jong, M. A. J. Michels, L. D. A. Siebbeles, J. M. Warman, G. H. Gelinck, G. Brocks, "Predicting polarizabilities and lifetimes of excitons on conjugated polymer chains", Chem. Phys. Lett., Vol 334, p303, 2001

[77] Jean-Luc Bredas, David Beljonne, Veaceslav Coropceanu, and Jerome Cornil, "Charge-transfer and energy-transfer processes in pi-conjugated oligomers and polymers: a molecular picture", Chem. Rev., Vol 104, p4971, 2004

[78] E. Hendry, M. Kowberg, J. M. Schins, L. D. A. Siebbeles, M. Bonn, "Free carrier photogeneration in polythiophene versus poly(phenylene vinylene) studied with THz spectroscopy", Chem. Phys. Lett., Vol 432, p441, 2006

[79] K.Lee, R. Menon, C. O. Yoon, and A. J. Heeger,"Reflectance of conducting polypyrrole: observation of the metal-insulator transition driven be disorder", Phys. Rev. B, Vol 52, p4779, 1995

[80] Maher Al-Ibrahim, H.-Klaus Roth, Uladzimir Zhokhavets, Gerhard Gobsch, Steffi Sensfuss, "Flexible large are polymer solar cells based on poly(3-hexylthiophene)/fullerene", Solar Energy Materials & Solar Cells, Vol 85, p13-20, 2005

[81] D. Chirvase, J. Parisi, J. C. Hummelen, and V. Dyakonov, "Influence of nanomorphology on the photovoltaic action of polymer-fullerene composites", Nano-technology, Vol 15, p1317, 2004

[82] G. Dicker, M. P. D. Haas, J. M. Warman, D. M. D. Leeuw, L. D. A. Siebbeles, "The disperse charge-carrier kinetics in regioregular poly(3-hexylthiophene)", J. Phys. Chem. B, Vol 108, p17818, 2004

[83] P. Prins, F. C. Grozema, L. D. A. Siebbeles, "Efficient charge transport along phenylene-vinylene molecular wires", J. Phys. Chem. B, Vol 110, p14659, 2006

[84] Benjamin J. Schwartz, "Conjugated polymers as molecular materials: how chain conformation and film morphology influence energy transfer and interchain interactions", Annu. Rev. Phys. Chem., Vol 54, p141, 2003

[85] Peter J. Brown, Henning Sirringhaus, Mark Harrison, Maxim Shkunov, and Richard H. Friend, "Optical spectroscopy of field-induced charge in self-organized high mobility poly(3-hexylthiophene)", Phys. Rev. B, Vol 63, p125204, 2001

[86] E. Hendry, M. Koeberg, J. M. Schins, H. K. Nienhuys, V. Sundstrom, L. D. A. Siebbeles, and M. Bonn, "Interchain effects in the ultrafast photophysics of a semiconducting polymer: THz time-domain spectroscopy of thin films and isolated chains in solution", Phys. Rev. B, Vol 71, p125201, 2005

[87] K. F. Voss, C. M. Foster, L. Smilowitz, D. Mihailovic, S. Askari, G. Srdanov, Z. Ni, S. Shi, A. J. Heeger, and F. Wudl, "Substitution effects on bipolarons in alkoxy derivatives of poly(1,4-phenylene-vinylene)", Phys. Rev. B, Vol 43, No 6, p5109, 1991

[88] E. Kirk Miller, Kwanghee Lee, Kobi Hasharoni, J. C. Hummelen, Fred Wudl, Alan J. Heeger, "Photo-induced changes in the comples index of refraction in conjugated polymer/fullerene blends", J. Chem. Phys., Vol 108, No 4, p1390, 1998